

## **INFORMATION TO USERS**

The negative microfilm copy of this dissertation was prepared and inspected by the school granting the degree. We are using this film without further inspection or change. If there are any questions about the content, please write directly to the school. The quality of this reproduction is heavily dependent upon the quality of the original material.

The following explanation of techniques is provided to help clarify notations which may appear on this reproduction.

1. Manuscripts may not always be complete. When it is not possible to obtain missing pages, a note appears to indicate this.
2. When copyrighted materials are removed from the manuscript, a note appears to indicate this.
3. Oversize materials (maps, drawings, and charts) are photographed by sectioning the original, beginning at the upper left hand corner and continuing from left to right in equal sections with small overlaps.
4. Most photographs reproduce acceptably on positive microfilm or microfiche but lack clarity on xerographic copies made from the microfilm. For any illustrations that cannot be reproduced satisfactorily by xerography, photographic prints can be purchased at additional cost and tipped into your xerographic copy. Requests can be made to the Dissertations Customer Services Department.



University Microfilms International  
A Bell & Howell Information Company  
300 N. Zeeb Road, Ann Arbor, Michigan 48106



**Order Number 9111378**

**Spatial heterodyne spectroscopy: Interferometric performance at  
any wavelength without scanning**

**Harlander, John Mark, Ph.D.**

**The University of Wisconsin - Madison, 1991**

**U·M·I**  
300 N. Zeeb Rd.  
Ann Arbor, MI 48106



# A dissertation entitled

SPATIAL HETERODYNE SPECTROSCOPY: INTERFEROMETRIC  
PERFORMANCE AT ANY WAVELENGTH WITHOUT SCANNING

submitted to the Graduate School of the  
University of Wisconsin-Madison  
in partial fulfillment of the requirements for the  
degree of Doctor of Philosophy

by

John M. Harlander

Degree to be awarded: December 19\_\_\_\_ May 1991 August 19\_\_\_\_

Approved by Dissertation Readers:

John M. Harlander

Major Professor

Jan 14, 1991

Date of Examination

James E. Lawler

Raymond J. Funk

John D. Wiley

Dean, Graduate School



**SPATIAL HETERODYNE SPECTROSCOPY: INTERFEROMETRIC  
PERFORMANCE AT ANY WAVELENGTH WITHOUT SCANNING**

**by**

**John M. Harlander**

**A thesis submitted in partial fulfillment of the  
requirements for the degree of**

**Doctor of Philosophy**

**(Physics)**

**at the**

**UNIVERSITY OF WISCONSIN-MADISON**

**1991**

**Abstract****SPATIAL HETERODYNE SPECTROSCOPY: INTERFEROMETRIC  
PERFORMANCE AT ANY WAVELENGTH WITHOUT SCANNING**

John M. Harlander

Under the supervision of Professor Fred L. Roesler

at the University of Wisconsin-Madison

In Spatial Heterodyne Spectroscopy (SHS), the wavenumber dependent Fizeau fringe pattern produced by a dispersive two-beam interferometer provides the Fourier transform of a selected spectral interval centered on the wavenumber for which the exiting wavefronts are perpendicular to the optical axis. This displacement of the zero spatial frequency to correspond to a favorable optical wavelength is analogous to the familiar time or frequency heterodyne technique. When the Fizeau fringe pattern is recorded on a position sensitive detector of suitable sensitivity, the spectrum may be recovered from a spatial Fourier transform of the recorded image. A

conventional Michelson Interferometer with its return mirrors replaced with diffraction gratings is an example of a two-beam dispersive interferometer. Since a diffraction grating may be used as a beam splitter, the concept is not restricted to spectral regions where suitable transmitting materials are available.

In a series of experimental and analytical studies, it has been shown that spectrometers operating on the SHS principal achieve the theoretical resolution limit of the gratings without scanning, but retain the large angular input tolerance of conventional scanning Fourier transform spectrometers. Field widening without moving elements can be achieved for transmitting and all-reflecting SHS configurations. The expected performance of specific SHS systems has been compared with conventional techniques for measurements of geocoronal Balmer-alpha radiation from the ground and far-ultraviolet emission lines in the interstellar medium from space.

Approved \_\_\_\_\_

Date \_\_\_\_\_

### Acknowledgements

There are many people who contributed to the work presented in this dissertation. First, I would like to thank Fred Roesler under whose patient guidance this work was done. Most of the concepts crucial to the development of SHS were Fred's or grew out of discussions with him. His knowledge of spectroscopy, combined with his intuition, insight , and open-minded approach were essential to fostering an environment where new ideas could develop.

I would like to thank Ron Reynolds who, along with Wilt Sanders and Blair Savage, were essential in securing funding so the development of SHS can continue. Ron also took over many of the administrative responsibilities of the group in Fred's absence.

The enthusiastic encouragement from Supriya Chakrabarti of UC-Berkeley Space Science Laboratory is greatly appreciated. Sup also loaned us some of the optical components and positioners used in the tests of the all-reflection configuration.

Dan McCammon's interest, comments and equipment loans were greatly appreciated. Discussions with Frank Scherb were also valued. Carey Woodward bailed me out of more computer problems than I care to

remember. Susan Nossal, Monica Coakley, and Dan Schultz absorbed some of my responsibilities while I was "distracted" with this work.

Outside of the research environment, I would like to thank my parents, family, and friends for their support and encouragement. Finally, I would like to thank my wife, Heidi, whose unconditional love, support, and help have made this all possible. It is to her that I dedicate this work.

## TABLE OF CONTENTS

|   |           |
|---|-----------|
| <b>Abstract</b>                           | <b>ii</b> |
| <b>Acknowledgements</b>                   | <b>iv</b> |
| <b>List of Tables</b>                     | <b>x</b>  |
| <b>List of Figures</b>                    | <b>xi</b> |
| <br>                                      |           |
| <b>Chapter 1: Overview</b>                |           |
| 1.1    Introduction                       | 1         |
| 1.2    The SHS Concept                    | 2         |
| 1.3    All-reflection SHS Interferometry  | 8         |
| 1.4    System Tests                       | 11        |
| 1.5    Discussion                         | 22        |
| 1.6    Summary                            | 27        |
| <br>                                      |           |
| <b>Chapter 2: Basic SHS Configuration</b> |           |
| 2.1    Introduction                       | 29        |
| 2.2    General Framework                  | 29        |
| 2.3    First Order Axial Analysis         | 33        |
| 2.4    Resolving Power                    | 36        |
| 2.5    Fringe Localization                | 38        |
| 2.6    Off-axis Analysis                  | 40        |

|  |   |    |
|--|---|----|
| 2.7  | Higher Order Frequency Shifts                           | 43 |
| 2.8  | Effect of Finite Aperture on the<br>Instrument Function | 44 |
| 2.9  | Spectral Range/Sampling                                 | 44 |
| <b>Chapter 3: SHS Systems with Two-Dimensional Detectors</b> |   |    |
| 3.1  | Introduction  | 49 |
| 3.2  | The Two-dimensional Technique                           | 49 |
| 3.3  | First Order Two-dimensional Tests                       | 53 |
| 3.4  | Echelle SHS Configuration                               | 56 |
| 3.5  | Spectral Range/Sampling                                 | 60 |
| 3.6  | SHS Echelle Simulations                                 | 64 |
| 3.7  | Fringe Localization                                     | 73 |
| 3.8  | Etendue Considerations                                  | 73 |
| <b>Chapter 4: All-Reflection Configurations</b>              |   |    |
| 4.1  | Introduction  | 76 |
| 4.2  | The Simple All-Reflection System                        | 77 |
| 4.3  | Phase Discontinuity Upon Diffraction                    | 77 |
| 4.4  | Ray Tracing Analysis                                    | 83 |
| 4.5  | First Order Axial Analysis                              | 90 |
| 4.6  | Fringe Localization Plane                               | 91 |

|   |                                       |     |
|---|---------------------------------------|-----|
| 4.7                                     | Off Axis Analysis                     | 92  |
| 4.8                                     | Reduced Resolving Power Configuration | 94  |
| 4.9                                     | Common Path Configurations            | 97  |
| 4.10                                    | Zero Order Reflections                | 100 |
| <b>Chapter 5: Field Widened Systems</b> |                                       |     |
| 5.1                                     | Introduction                          | 108 |
| 5.2                                     | Field Widened FTS Systems             | 109 |
| 5.3                                     | Field Widened SHS Systems             | 112 |
| 5.4                                     | Analysis                              | 112 |
| 5.5                                     | Fringe Frequency                      | 116 |
| 5.6                                     | Field of View Limits                  | 121 |
| 5.7                                     | Achromatic Field Widening             | 128 |
| 5.8                                     | All-Reflection Field Widening         | 133 |
| <b>Chapter 6: Noise Propagation</b>     |                                       |     |
| 6.1                                     | Introduction                          | 140 |
| 6.2                                     | General Treatment                     | 141 |
| 6.3                                     | Photon Limited Detection              | 142 |
| 6.4                                     | Multiplex Advantage                   | 146 |
| 6.5                                     | Scintillation Noise                   | 147 |
| 6.6                                     | Digitizing Noise                      | 148 |

|   |     |
|---|-----|
| 6.7 Distortions in Intensity                            | 148 |
| <b>Chapter 7: Performance Prediction and Comparison</b> |     |
| 7.1 Introduction  | 155 |
| 7.2 Geocoronal Balmer- $\alpha$ Instrumentation         | 155 |
| 7.3 FUV Interstellar Medium System                      | 166 |
| <b>Chapter 8: Summary and Suggestions for</b>           |     |
| <b>Future Research</b>                                  | 172 |
| <b>References</b>                                       | 175 |

**List of Tables**

|  |     |
|--|-----|
| Table 3.1    Spectral Range for Grating Orders<br>in the SHS Echelle Tests | 65  |
| Table 7.1    Comparison of Geocoronal Balmer-<br>alpha Systems             | 159 |
| Table 7.2 Comparison of Interstellar Medium<br>Systems                     | 171 |

**List of Figures**

|                   |   |           |
|-------------------|---|-----------|
| <b>Figure 1.1</b> | <b>Basic SHS Configuration</b>                                    | <b>4</b>  |
| <b>Figure 1.2</b> | <b>All-Reflection SHS Configuration</b>                           | <b>10</b> |
| <b>Figure 1.3</b> | <b>Common Path All-Reflection Configuration</b>                   | <b>13</b> |
| <b>Figure 1.4</b> | <b>Sodium Interferogram</b>                                       | <b>16</b> |
| <b>Figure 1.5</b> | <b>Sodium Spectrum</b>  | <b>18</b> |
| <b>Figure 1.6</b> | <b>All-Reflection System Test Results</b>                         | <b>21</b> |
| <b>Figure 1.7</b> | <b>Field Widened SHS Configuration</b>                            | <b>25</b> |
| <b>Figure 2.1</b> | <b>Coordinate Definition for Basic SHS System: First Grating</b>  | <b>32</b> |
| <b>Figure 2.2</b> | <b>Coordinate Definition for Basic SHS System: Second Grating</b> | <b>32</b> |
| <b>Figure 2.3</b> | <b>Instrumental Profile</b>                                       | <b>47</b> |
| <b>Figure 3.1</b> | <b>Grating Adjustment for Two-Dimensional Format</b>              | <b>51</b> |
| <b>Figure 3.2</b> | <b>Two-Dimensional System: Sodium Fringes</b>                     | <b>55</b> |
| <b>Figure 3.3</b> | <b>Fourier Transform of Figure 3.2</b>                            | <b>58</b> |
| <b>Figure 3.4</b> | <b>Grating Blaze Efficiency</b>                                   | <b>62</b> |

|            |  |     |
|------------|--|-----|
| Figure 3.5 | Echelle Test: Interferogram                                      | 67  |
| Figure 3.6 | Fourier Transform of Figure 3.5                                  | 69  |
| Figure 3.7 | Perspective Plot of Figure 3.6                                   | 72  |
| Figure 4.1 | All-Reflection SHS Configuration                                 | 79  |
| Figure 4.2 | Phase Relationship Between Incident<br>and Diffracted Wavefronts | 82  |
| Figure 4.3 | Phase Discontinuity of Diffracted<br>Ray                         | 82  |
| Figure 4.4 | Optical Equivalent of the All-<br>Reflection System: On Axis     | 85  |
| Figure 4.5 | Optical Equivalent of the All-<br>Reflection System: Off Axis    | 88  |
| Figure 4.6 | Reduced Resolving Power All-<br>Reflection Configuration         | 96  |
| Figure 4.7 | Common Path All-Reflection<br>Configuration                      | 99  |
| Figure 4.8 | Common Path Separated Input/<br>Output Configuration             | 102 |
| Figure 4.9 | Alternate Arrangement of All-<br>Reflection System               | 105 |

|             |   |     |
|-------------|---|-----|
| Figure 4.10 | Alternate Arrangement of Common Path System         | 107 |
| Figure 5.1  | Off-axis Properties of the Michelson Interferometer | 111 |
| Figure 5.2  | Field Widened Michelson Interferometer              | 111 |
| Figure 5.3  | Field Widened SHS System                            | 114 |
| Figure 5.4  | Angle Definition for Ray Tracing                    | 118 |
| Figure 5.5  | Maximum Field of View: $\phi$                       | 123 |
| Figure 5.6  | Maximum Field of View: $\beta$                      | 125 |
| Figure 5.7  | Maximum Field of View: $\Omega$                     | 127 |
| Figure 5.8  | One Arm of Achromatic Field Widened System          | 131 |
| Figure 5.9  | All-Reflection Field Widened System                 | 135 |
| Figure 5.10 | Alternate All-Reflection Field Widened System       | 139 |
| Figure 6.1  | Efficiency of Single Output System                  | 152 |

**Figure 7.1      Performance of Balmer-alpha**

**Instruments**

**165**

## 1. Overview

**1.1 Introduction:** It is well known that interference spectrometers offer significant advantages over conventional grating spectrometers in the study of faint, extended sources (Roesler, 1974). The primary advantages are 1) an etendue (throughput) typically 200 times larger than grating spectrometers operating at similar resolution, 2) compact size, especially at high resolution, and 3) relative ease of obtaining high spectral resolution. In combination these advantages offer scientific programs important economies in observing time, cost, weight, and volume.

At the University of Wisconsin-Madison an interferometric spectroscopic technique called Spatial Heterodyne Spectroscopy (SHS) is being developed (Harlander & Roesler, 1990; Roesler & Harlander, in press; Harlander et al., in press). The SHS technique utilizes a two-beam dispersive interferometer to produce a Fizeau fringe pattern having wavenumber-dependent spatial frequencies. This pattern is recorded on an imaging detector and Fourier transformed to recover the input spectrum. Zero spatial frequency can be set at a selected wavenumber and thus, the system is analogous to temporal frequency heterodyne techniques. In addition to the advantages of conventional interferometric spectroscopic systems, SHS

instruments are self-scanned (no moving parts), can be field widened, and built in an all-reflection configuration for UV applications.

SHS is a close relative of conventional Fourier Transform Spectroscopy (FTS), however, most of the complex problems of scan and control associated with FTS are avoided. In operation, SHS requires stability but neither critical alignment nor scanning. It has some limitations compared to its more complex relatives, but with suitable design and experimental technique these limitations may be avoided for certain problems.

The first chapter of this dissertation is a stand-alone introduction to the technique. The salient features of the instrument are described, in many cases at a descriptive level, to convey a perspective on the discussion in subsequent chapters. The first chapter also describes system tests that have been performed which illustrate the first-order properties of the device. The following chapters will reintroduce the SHS concept and examine pertinent aspects of the system in greater depth.

**1.2 The SHS Concept:** The basic SHS concept is most easily understood by considering the transmitting beamsplitter arrangement illustrated in Figure 1.1, where a conventional Michelson interferometer is shown with the return mirrors replaced by diffraction gratings  $G_1$  and  $G_2$ . Light enters through aperture  $A_1$  and is collimated by lens  $L_1$ . At the exit,

---

**Figure 1.1:** Schematic diagram of the basic SHS configuration:  
Wavelength dependent Fizeau fringes produced by diffraction gratings  $G_1$  and  
 $G_2$  are recorded by a position sensitive detector I. The Fourier transform of  
the fringe pattern recovers the spectrum.

---

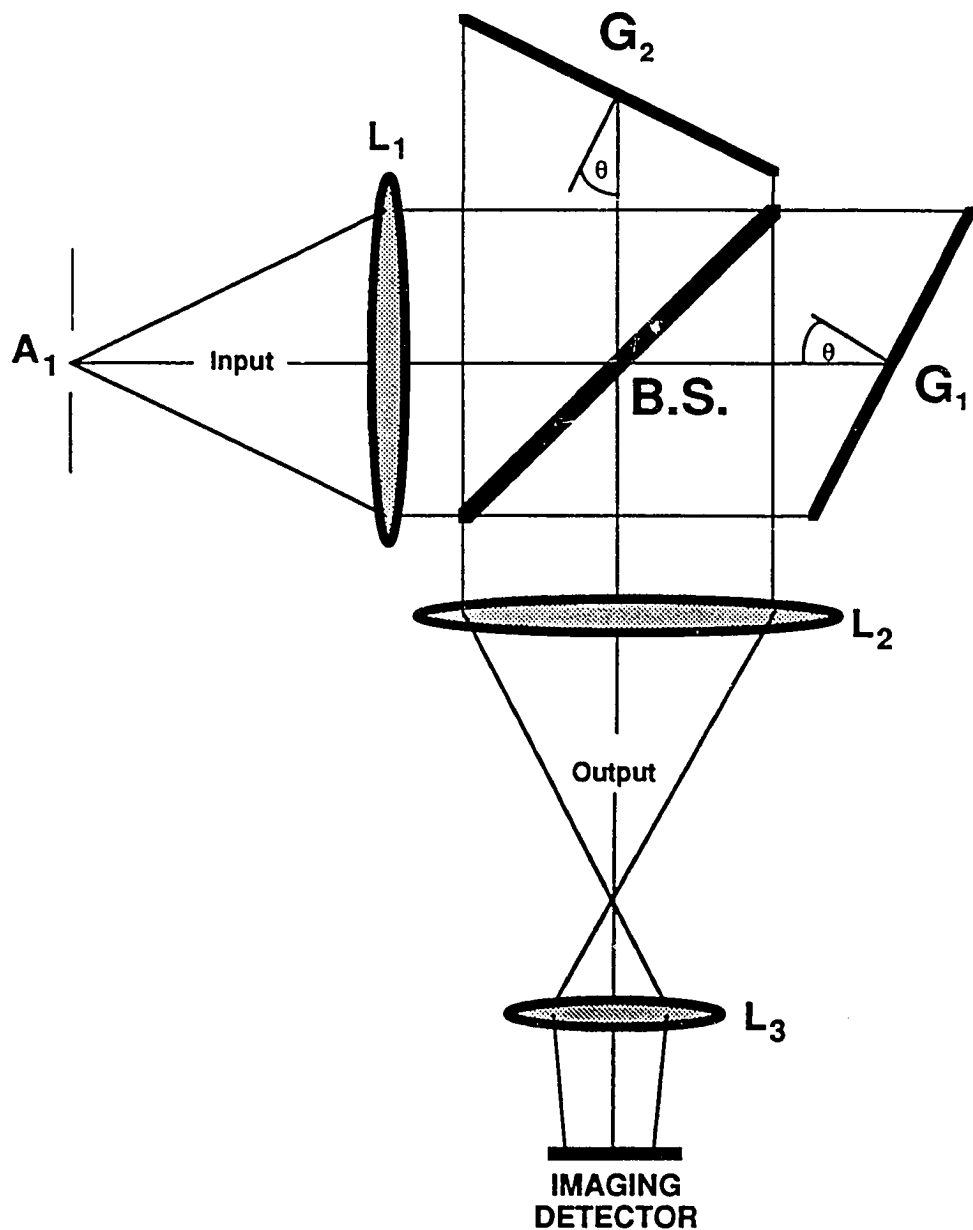


**Figure 1.1**

lenses  $L_2$  and  $L_3$  relay the superposed coherent images of gratings  $G_1$  and  $G_2$  onto the image plane  $I$  where a position sensitive detector records the Fizeau fringe pattern produced by the interferometer. The generation of Fizeau fringes of wavenumber-dependent spatial frequency follows from the grating equation

$$\sigma[\sin\theta + \sin(\theta - \gamma)] = \frac{m}{d} \quad (1.1)$$

where  $\sigma$  is the wavenumber of light,  $m$  is the order of diffraction,  $\theta$  is the Littrow angle and  $1/d$  is the grating groove density. For a point source of wavenumber  $\sigma$  in the input aperture on axis, two coherent plane wavefronts are produced at the output (one from each arm) whose wave vectors are inclined to the optical axis by angles  $\gamma$  and  $-\gamma$  respectively. Ignoring magnification by  $L_2$  and  $L_3$ , these crossed wavefronts produce Fizeau fringes of spatial frequency

$$f_x = 2\sigma \sin\gamma \approx 4(\sigma - \sigma_0) \tan\theta \quad (1.2)$$

where the right hand side is derived from an expansion of equation 1.1 for small  $\gamma$ , and  $\sigma_0$  is the Littrow ( $\gamma=0$ ) wavenumber. For input spectral density  $B(\sigma)$ , the intensity recorded as a function of position  $x$  is given by

$$I(x) = \int_0^{\infty} B(\sigma) (1 + \cos[2\pi(4(\sigma - \sigma_0)x \tan\theta)]) d\sigma \quad (1.3)$$

where  $x$  is measured on the detector in the dispersion plane of the gratings. The Fourier transform of  $I(x)$  recovers the input spectrum. In this process, no element is mechanically scanned and zero spatial frequency corresponds to  $\sigma - \sigma_0$ . Effectively, SHS instruments record the entire path difference scanned by FTS on a position sensitive detector without scanning, and heterodyne the interferogram with a frequency corresponding to the Littrow wavenumber of the gratings.

The limiting resolving power ( $\sigma/\delta\sigma$ ) can be shown to be equal to the theoretical resolving power of the dispersive system. For the geometry in Figure 1.1 the result is

$$R_0 = 4W\sigma \sin\theta \quad (1.4)$$

where  $W$  is the width of the gratings and  $\theta$  is the Littrow angle. As in FTS, the resolving power is simply twice the maximum path difference in the system divided by the wavelength.

The spectral range of SHS systems is limited by the highest spatial frequency that can be recorded on the imaging detector without aliasing. For  $N$  detector elements in one dimension,  $N/2$  spectral elements may be

recovered. This is in marked contrast to the FTS technique where the number of samples required is typically equal to twice the resolving power of the system. In high resolution FTS, the number of samples can become quite large. The reduction in the number of samples required by SHS instruments is a direct result of the heterodyned nature of the interferogram recorded and enables SHS systems to attain high resolution with relatively few samples.

By including off-axis input angles in the grating equation (eq. 1.1), the solid angle field-of-view  $\Omega$  of SHS instruments can be shown to be  $\Omega = 2\pi/R$  where  $R$  is the resolving power of the system. This is the same value achieved by conventional FTS or Fabry-Perot interferometers.

Specialists in interference spectroscopy might recognize the optical configuration of the basic SHS system as similar to the SISAM interferometer (Connes, 1958). SHS differs from the SISAM in that it uses an imaging detector to record all spectral elements simultaneously as opposed to the single channel scanned detection of the SISAM. The first description of a true SHS system was given by Dohi and Susuki (1971) who employed photographic film as the imaging detector. Advances in imaging detectors in the last decade have led to a rediscovery of the SHS concept both at the University of Wisconsin and in the Netherlands (Butcher et al., 1989). The thrust of the European effort has been to develop SHS for use with the next

generation of large aperture ( $D > 8$  meters) telescopes (Douglas et al., 1990).

At the University of Wisconsin, the thrust is the application of the technique for studies of diffuse emission lines originating in the interstellar medium and airglow.

**1.3 All-Reflection SHS Interferometry:** In addition to the basic SHS configuration described above, a number of all-reflection SHS configurations have been conceived which bring the gains of interference spectroscopy to spectral regions where transmitting optical materials are not available. These systems do not require the complex scan and control mechanisms of earlier all-reflection FTS instruments (Kruger et al., 1972).

Figure 1.2 shows a simple all-reflection SHS configuration. Light enters the lower portion of the elliptical aperture  $S$ , is collimated by  $M_3$ , and divided by beam-splitting grating  $G_0$ , which may be holographically produced to provide symmetric splitting. Mirrors  $M_1$  and  $M_2$  return the diffracted light to the grating which recombines the beams and sends the light through the exit portion of the aperture and onto the imaging detector. The diffraction grating acts as both the beam-splitter and the dispersive element in the system. Zero spatial frequency corresponds to the wavenumber of light ( $\sigma_0$ ) whose rays are normal to mirrors  $M_1$  and  $M_2$ . The theoretical resolution of the dispersive system determines the resolving power of the interferometer,

---

**Figure 1.2:** Schematic diagram of the all-reflection SHS configuration.

Light enters the system through the lower half of split aperture S and exits through the upper half. The diffraction grating acts as both the beam splitter and dispersive element in the system.

---

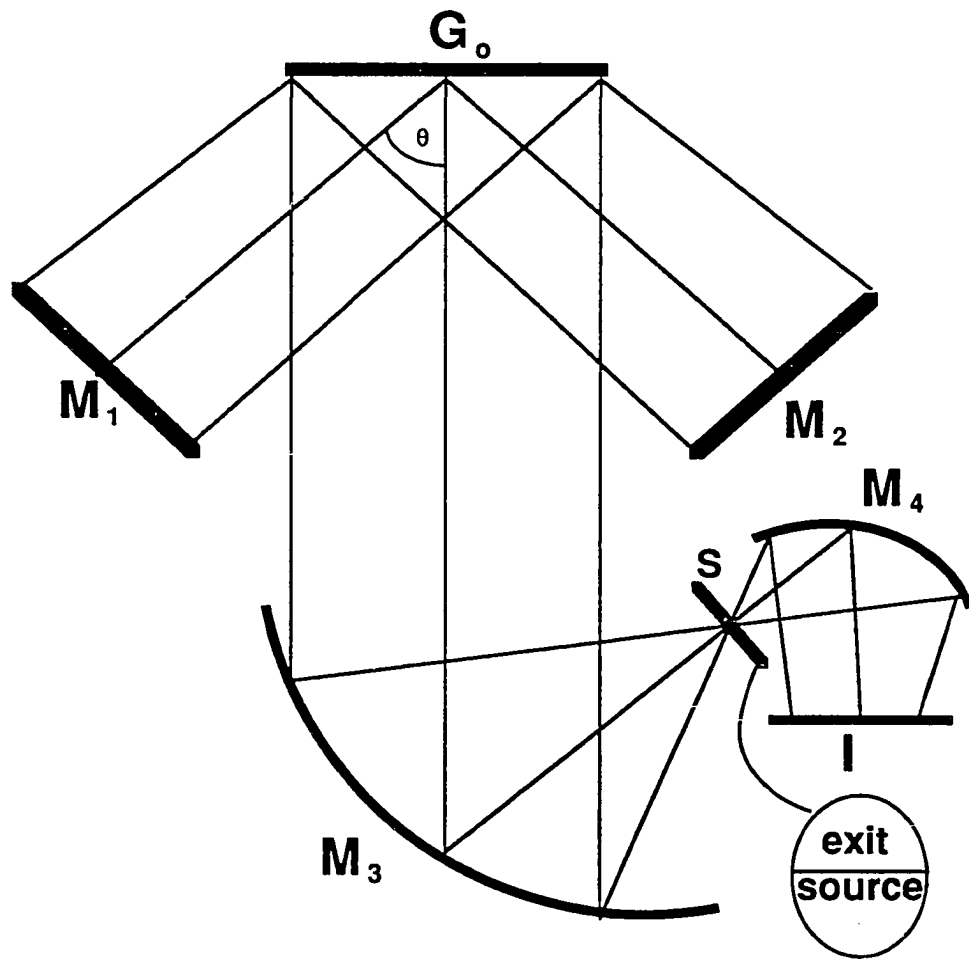


**Figure 1.2**

which is given by equation 1.4 above. The etendue of the all-reflection system is reduced by a factor of  $\cos\theta$  from the etendue in the basic SHS configuration due to the magnification introduced by the non-Littrow diffraction at the grating.

Figure 1.3 shows a common path all-reflection SHS system. Light enters the instrument through mechanical collimator C and is split into two beams by the bottom half of diffraction grating G. The beams travel through the interferometer in opposite directions, indicated by dashed and solid lines in the figure, are recombined by the top half of the grating and focused onto the detector by mirror  $M_3$ . Since a translation of any one of the optical elements in the interferometric portion of the instrument effects both beams in the same manner, the system is very stable. Note that this interferometer records only one side of the symmetric interferogram. To obtain a two-sided interferogram, either mirror  $M_1$  or  $M_2$  may be replaced by a roof mirror oriented so the beams are combined directly below (into the plane of the figure) the point where the beams are split.

**1.4 System Tests:** The optical performance of both conventional and all-reflection SHS instruments has been verified in the visible and near-UV portions of the spectrum, respectively. For these tests a Photometrics camera system employing a PM512 CCD chip coated with Metachrome II for UV

**Figure 1.3:** Common path configuration of an all-reflection SHS interferometer. Light enters the system through mechanical collimator C and is split into two beams by the lower half of diffraction grating G. The two beams travel through the interferometer in opposite directions, shown by the dashed and solid line, are recombined on the upper half of the grating, and are focused onto the imaging detector by mirror M<sub>3</sub>.

---

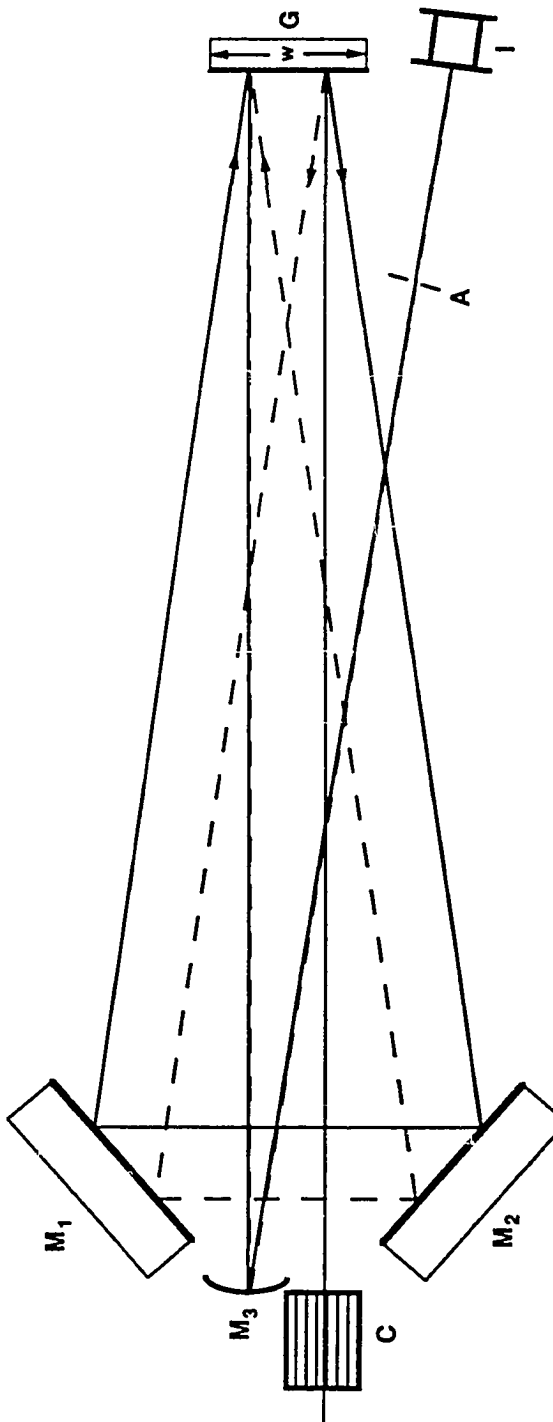


Figure 1.3

sensitivity was used. Both instruments performed as expected in all respects.

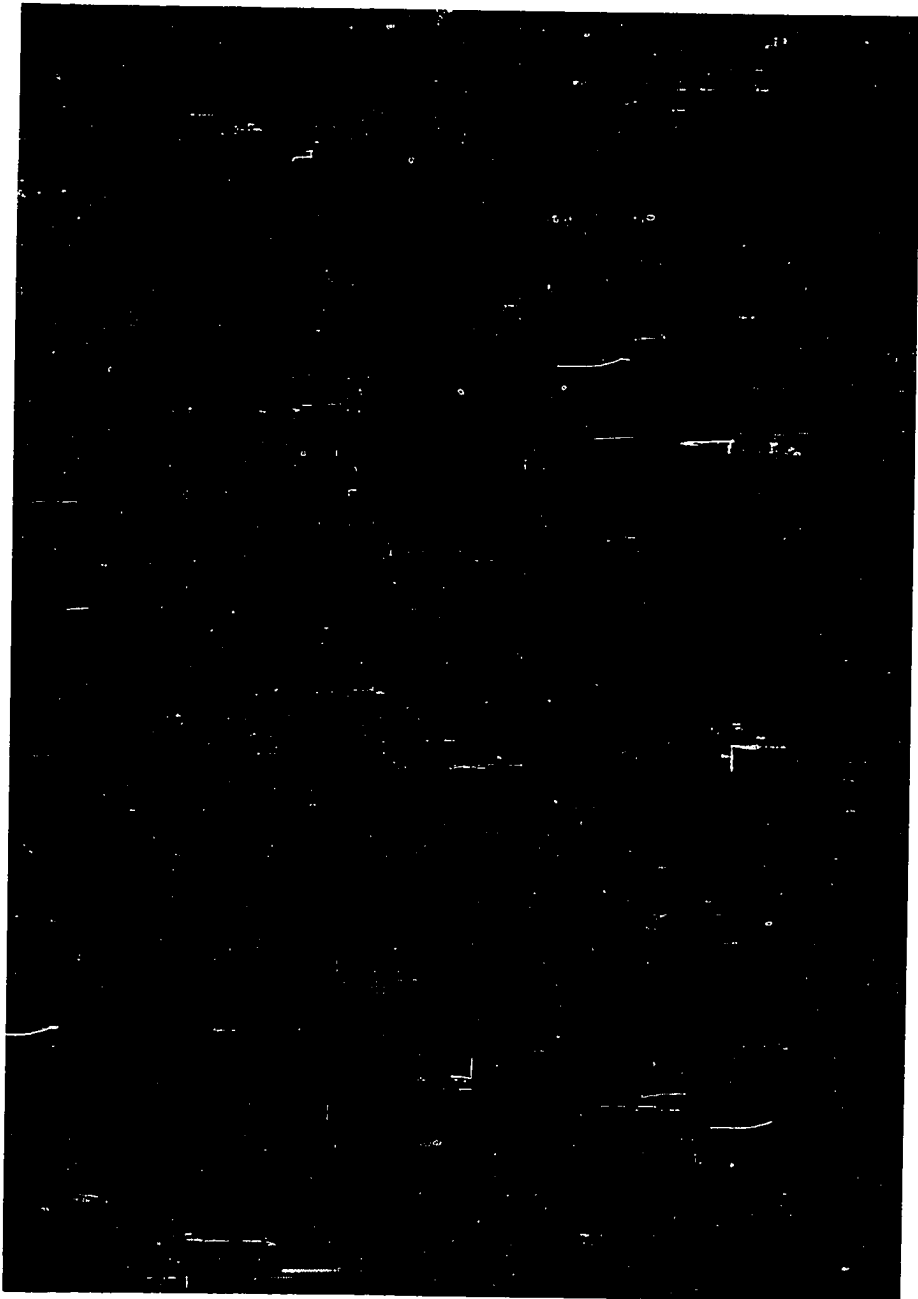
Tests of the visible system (Figure 1.1) were performed using the sodium doublet ( $5889.95\text{\AA}$  and  $5895.92\text{\AA}$ ). The diffraction gratings were conventionally blazed with diffraction angle  $\theta$  of  $20.7^\circ$  at  $5890\text{\AA}$  (first order Littrow with a groove density of 1200 g/mm). The width of the diffraction gratings imaged onto the detector was approximately 17.5 mm therefore, the resolving power predicted for this system by equation 1.4 is  $\sim 42,000$ . The aperture which limited the field-of-view for the system was chosen to achieve a throughput characteristic of interference spectrometers of the same size and resolving power. Figure 1.4 shows the intensity pattern recorded on the CCD detector for this system. The background in the figure is a grayscale image of the intensity pattern showing two distinct spatial frequencies. Overlaying this is a line plot which represents the intensity versus pixel number for a vertical slice through the image. A flat field was obtained by summing images taken with the alternate arms of the interferometer blocked. The wavelength corresponding to zero frequency ( $\lambda_0 - 1/\sigma_0$ ) was set at approximately  $5896.6\text{\AA}$ . Therefore, the low frequency modulation is attributed to the  $5895.9\text{\AA}$  line and the high frequency modulation is attributed to the line at  $5889.9\text{\AA}$ .

Figure 1.5 shows the amplitude of the Fourier transform of the line

---

**Figure 1.4:** Photograph of the fringe pattern formed by the Na doublet at  $5890\text{\AA}$  and  $5896\text{\AA}$  using the configuration shown in Figure 1.1, and a superimposed graph of intensity averaged over 20 columns. The low frequency modulation is from the line at  $5890\text{\AA}$  and the high frequency modulation is from  $5896\text{\AA}$  radiation.

---

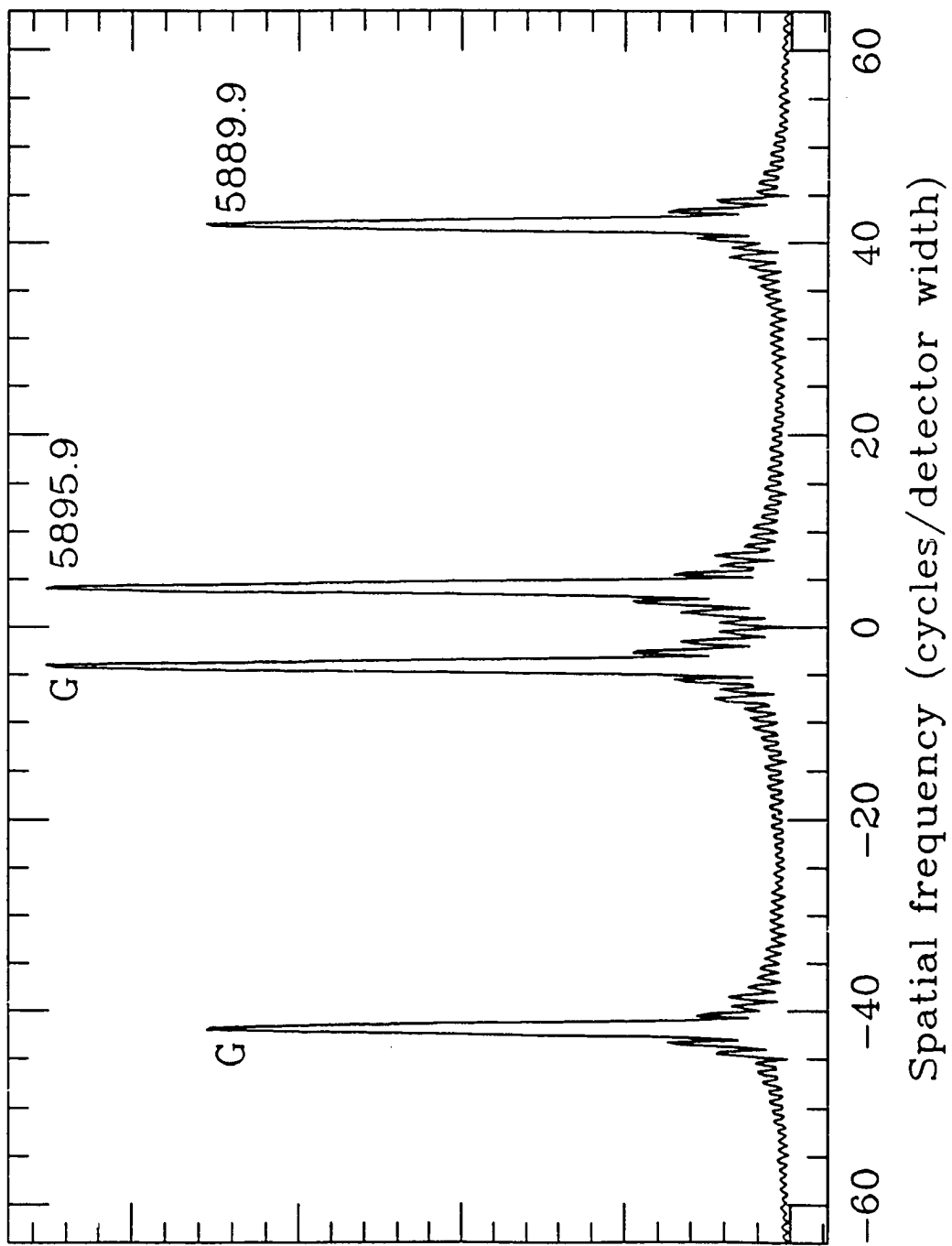


**Figure 1.4**

**Figure 1.5:** One-dimensional amplitude Fourier transform of the fringe pattern shown in Figure 1.4: The lines labeled G are transform ghosts which result from the symmetry of the cosine interferogram produced by the instrument.

---

Figure 1.5: Sodium spectrum  $R=40,000$



plot in Figure 1.4. The ringing spectra indicate that neither line is resolved in this system. The achieved resolving power can be determined by measuring the width of the emission peaks in Figure 1.5. Using the 5.97Å separation of the two emission lines to calibrate the wavenumber scale, the achieved resolving power is ~ 39,000.

The symmetric transform in Figure 1.5 shows "true" and "ghost" spectra because the instrument produces identical output for input wavenumbers  $\sigma_0 + \Delta\sigma$  and  $\sigma_0 - \Delta\sigma$  (cf. equation 1.3). The resulting ambiguity can be avoided by prefiltering or by employing a two-dimensional format in which the Fizeau fringes exhibit a wavenumber-dependent rotation. The two-dimensional format is described in Chapter 3.

Tests of the all-reflection system were performed using the Hg resonance line at 2537Å on the common path configuration shown in Figure 1.3. Three different Hg sources were measured: an Hg-198 source, a natural Hg source, and a natural Hg source coupled to an absorption cell. Since approximately 15 mm of a holographically ruled diffraction grating of groove density 600 g/mm used in first order was imaged on the detector, a resolving power of 70,000 was expected.

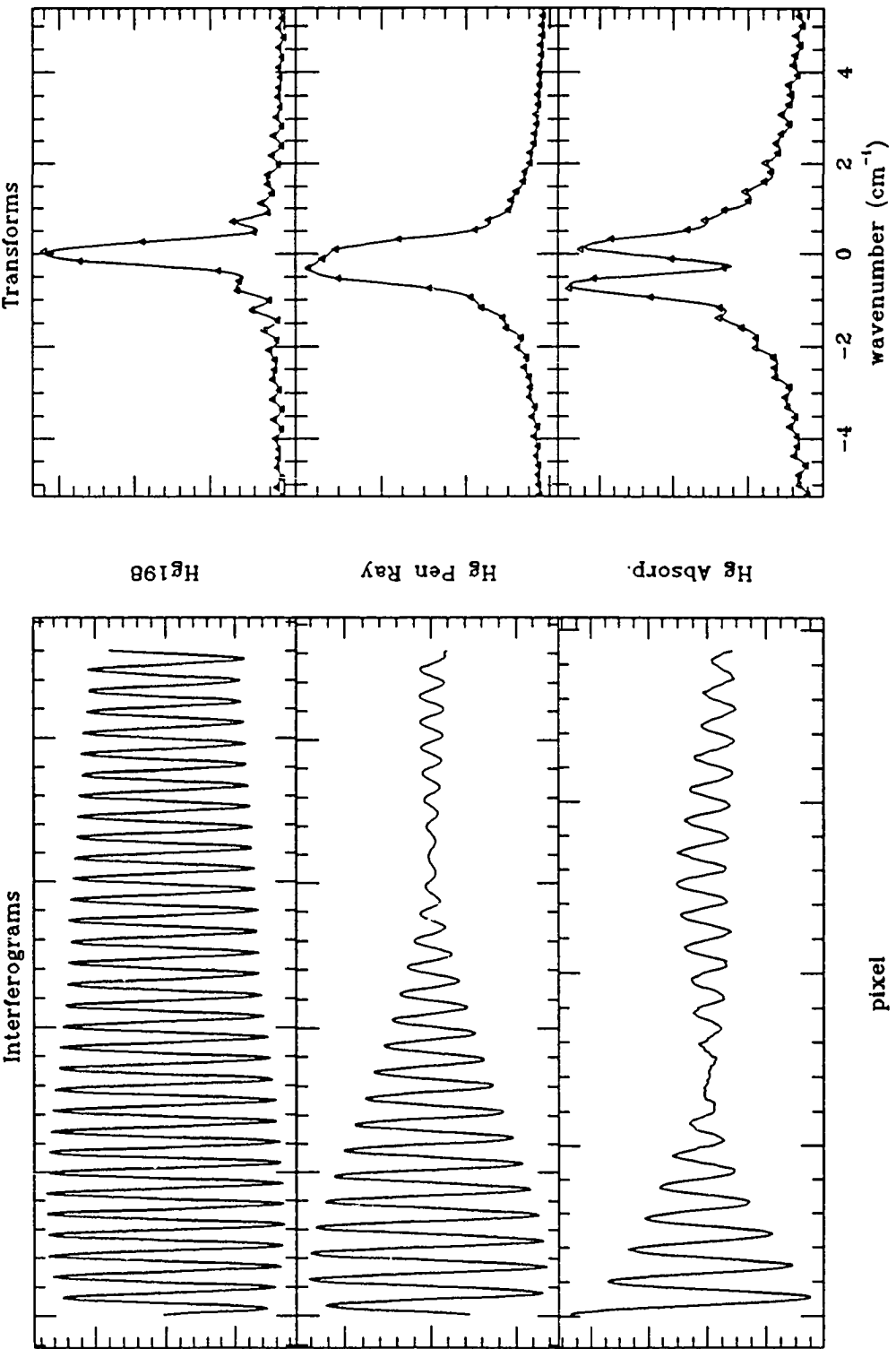
Test results of the all-reflection system are shown in figure 1.6. The upper left-hand panel shows the interferogram recorded using the Hg-198

---

**Figure 1.6:** Interferograms and spectra from tests of the all-reflection-common path interferometer in Figure 1.3: Zero on the wavenumber scale corresponds to the peak of the Hg-198 line. See text for more details.

---

Figure 1.6: Hg  $\lambda 2537$  Tests  $R=70,000$



source. The upper right-hand plot shows the spectrum of the source obtained from the amplitude Fourier transform of the interferogram. Only the portion of the transform near the 2537Å line is shown. The near-constant amplitude modulation of the interferogram and ringing spectrum indicate that the narrow line produced by the single isotope in the Hg-198 source is unresolved by the system. The spectrum closely resembles a  $|\text{sinc}|$  function which, in the case of an amplitude transform, is the instrumental profile of this system. The center of Figure 1.6 shows a similar sequence of plots for the natural Hg source. Since natural Hg contains a number of isotopes, the line is broader than the previous case and is clearly resolved. The lower panels of Figure 1.6 were obtained by passing the light from the natural Hg source through an unlit Hg germicidal lamp which acted as an absorption cell. Since a detailed wavenumber calibration was not performed during tests of this system, the wavenumber scale in Figure 1.6 was obtained by considering the theoretical resolution of the system and the expected width of the natural Hg source.

**1.5 Discussion:** Since SHS records spectral information in the Fourier domain, many of the advantages and disadvantages of conventional Fourier Transform Spectroscopy apply to SHS. In other respects SHS differs from FTS.

*Immunity to Artifacts Due to Source Variations:* SHS systems detect the

entire interferogram simultaneously therefore, variations in source intensity (so-called scintillation noise) do not distort the spectra as is the case with FTS. However, SHS systems distribute the interferogram over a number of detector channels which can lead to an analogous distortion if the detectors are not carefully cross-calibrated.

*Loss of Absolute Wavelength Standard:* As is the case with other dispersive systems, SHS does not achieve the high wavelength accuracy of FTS. In many situations, however, this limitation will not significantly compromise the quality of the data obtained.

*Field Widening:* Field widening is a technique developed for FTS whereby the field of view, and therefore the etendue, of the instrument may be increased greatly over that achieved by conventional interferometric instruments. The gains achieved with this technique depend on the resolving power and the method used to achieve field widening, but gains in light gathering power of two orders of magnitude are not uncommon (Baker, 1977). The principle difference between field widening an FTS instrument and an SHS instrument is field widening can be achieved in SHS systems with no moving parts. The simplest field widened SHS system is obtained by placing appropriate prisms into the arms of the instrument as shown in Figure 1.7. The prism angle is chosen so the refractive material in the prism

---

**Figure 1.7:** Field widened SHS configuration: The geometric properties of prisms  $P_1$  and  $P_2$  increase the field of view of the system. The input and output optics are shown in Figure 1.1.

---

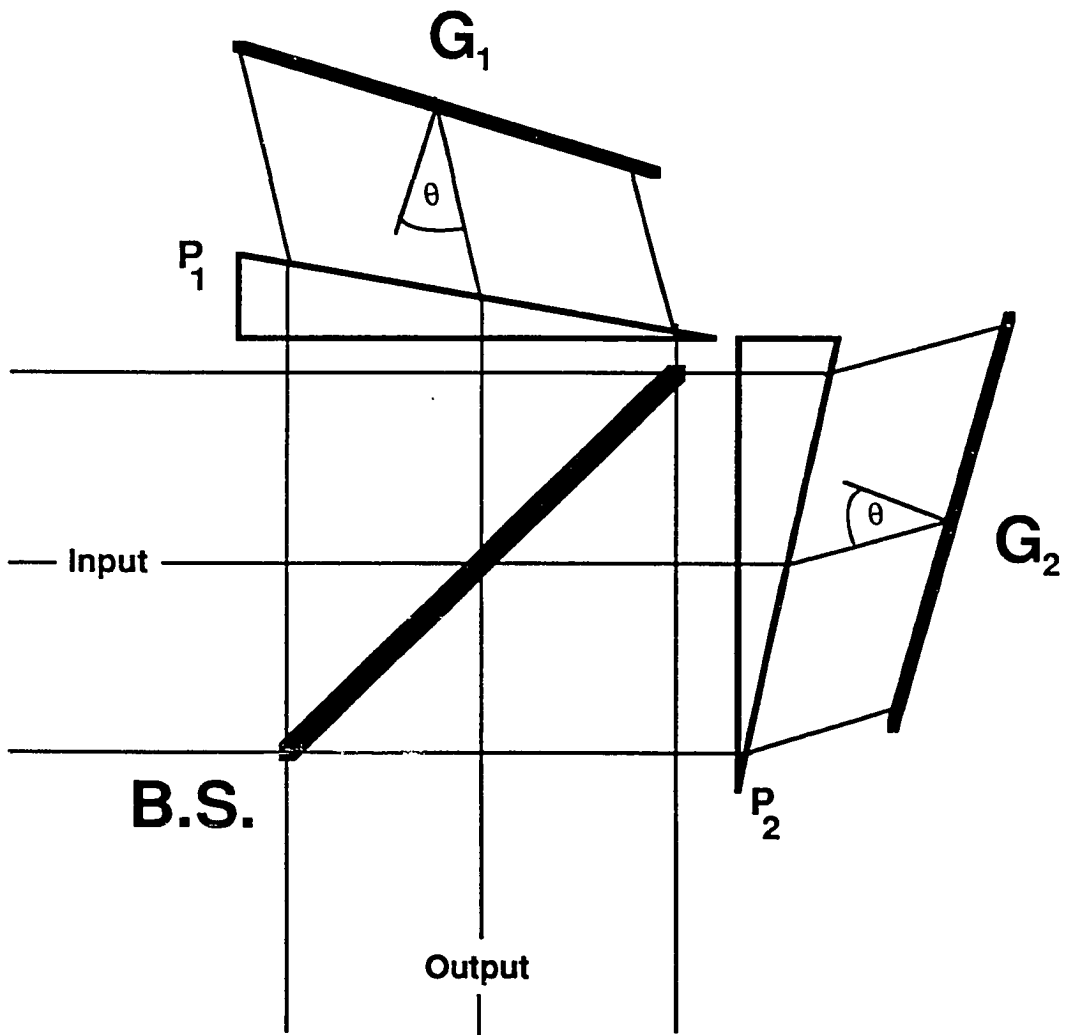


**Figure 1.7**

geometrically rotates the image of the gratings so they appear normal to the optical axis. Ultimately, asymmetries introduced by the prisms limit the field of view, but not before significant gains can be achieved for many problems.

*Echelle Mode:* In order to achieve the broad spectral range many situations require, the narrow bandwidth restrictions imposed by the finite number of pixels in one dimension of available imaging detectors may be overcome by utilizing pixels in both dimensions on a two-dimensional detector to record spectral information. The details of this technique are described in Chapter 3.

*Multiplex Advantage:* A multiplex advantage is attained by FTS systems in spectral regions where the dominant noise in the system is generated by the detector. All photons passed by the system are detected by a single detector; hence the photon flux on the detector is increased by a large factor over a comparable non-multiplex system. As a result, the signal-to-noise ratio of spectra obtained with multiplex systems is higher than achieved by non-multiplex systems (Sakai, 1977). Since SHS systems distribute the interferogram over a number of detector elements, the classical multiplex advantage does not apply. However, a partial multiplex gain may be realized since the photon flux on a particular detector element may be greater in SHS than the flux detected by a competing technique. In situations where the

detection is dominated by photon noise, the SHS system performs comparably to FTS instruments from a signal-to-noise ratio point of view.

*Self-Measurement of Critical Alignment State:* A very important practical aspect of SHS systems is they appear to be exceptionally forgiving of errors. The fringe patterns recorded for a monochromatic input by SHS instruments are measurements of wavefront errors and the exact state of alignment. At the time an observation is made, the measured fringe pattern of a calibration lamp may be used to correct in software for the adjustment state of the instrument and figure errors of the optical surfaces. Stability within approximately  $\lambda/10$  would be required during an exposure, but long term drifts or the effects of impacts within achievable mechanical stability requirements may be corrected.

**1.6 Summary:** SHS is likely to have important applications, particularly in the study of faint, diffuse light sources. Important properties of this instrument are:

- the resolving power achieved is the diffraction limit of the dispersive system in the configuration being considered
- the etendue (area  $\times$  solid angle) is characteristic of interference spectrometers at the achieved resolving power
- scanned elements are not required

- spectral coverage is achieved instantaneously
- field-widening can be achieved without moving parts
- the concept can be implemented at any wavelength
- high resolution is attainable in a compact package.

## 2. Basic SHS Configuration

**2.1 Introduction:** With the overview of SHS instruments provided in Chapter 1, attention may now turn to an in-depth analysis of the basic SHS system shown in Figure 1.1. Important properties of this device will be derived from first principles with an emphasis on aspects common to all SHS systems. To calculate these properties in detail, a general framework for precisely predicting the Fizeau fringe pattern produced by the interferometer will be introduced. This framework will be helpful in deriving the maximum field-of-view, the fringe localization plane, and the instrumental profile of the basic SHS system. It will also be utilized in subsequent chapters as an aid in developing the properties of other SHS systems.

**2.2 General Framework:** The intensity distribution produced by the interference of two coherent plane wavefronts characterized by wavevectors  $\vec{k}_1$  and  $\vec{k}_2$  (ignoring polarization) is

$$I = I_1 + I_2 + 2\sqrt{I_1 I_2} \cos((\vec{k}_1 - \vec{k}_2) \cdot \vec{r} + \varepsilon_1 - \varepsilon_2) \quad (2.1)$$

where  $I_1$  and  $I_2$  are the intensities of the individual waves and  $\varepsilon_1$  and  $\varepsilon_2$  are their phases at the origin of  $\vec{r}$ . If  $I_1 = I_2 = I_0/2$  and  $\varepsilon_1 - \varepsilon_2 = 0$ , then equation 2.1 reduces to

$$I = I_0(1 + \cos((\vec{k}_1 - \vec{k}_2) \cdot \vec{r})). \quad (2.2)$$

Figures 2.1 and 2.2 illustrate the diffraction gratings  $G_1$  and  $G_2$  from Figure 1.1 as they appear to an incoming wavevector. Also shown in these figures is a coordinate system whose origin coincides with the point where the images of the two gratings cross as viewed looking back into the instrument. The y axis is along the grooves of the gratings and the z axis is along the optical axis of the interferometer. The gratings are positioned so the z axis intersects them at the center of a groove facet. This insures that phase shifts introduced upon diffraction at the gratings are the same for both arms of the interferometer and can be ignored (see section 4.3 for a more detailed discussion). A general wavevector,  $\vec{k}_i$ , can be expressed in the coordinates defined in Figures 2.1 and 2.2 as

$$\begin{aligned} k_x &= 2\pi\sigma \cos\phi_i \sin\beta_i \\ k_y &= 2\pi\sigma \sin\phi_i \\ k_z &= 2\pi\sigma \cos\phi_i \cos\beta_i \end{aligned} \quad (2.3)$$

where  $\sigma$  is the wavenumber. The grating equation is given by  $\sigma \cos\phi (\sin\theta_{in} + \sin\theta_{out}) - m/a$  where  $m$  is the order number,  $1/a$  is the groove density,  $\theta_{in}$  and  $\theta_{out}$  denote the direction of the component of the incoming

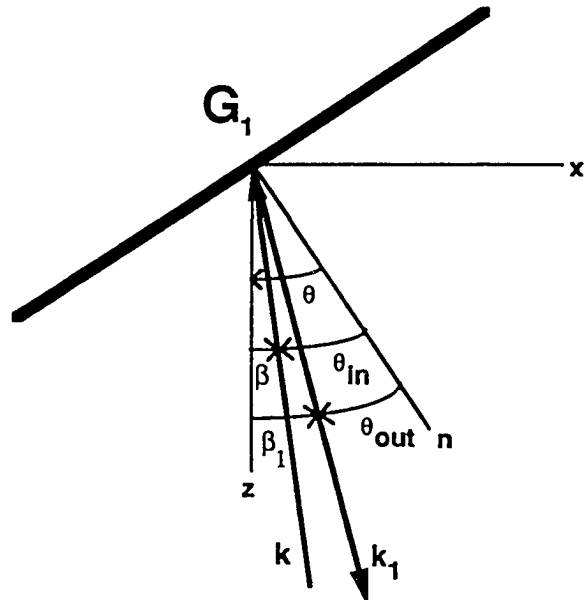
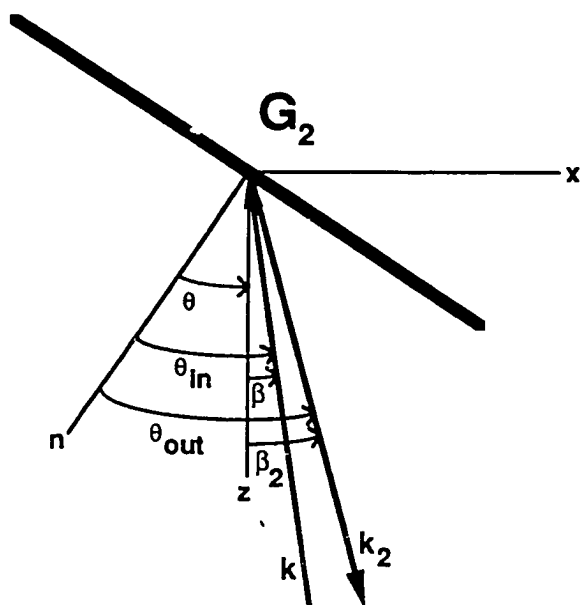
**Figure 2.1** Relationship between the various angles for grating  $G_1$  used in the derivation of equation 2.4: The angle  $\theta$  between the grating normal  $n$  and the  $z$  axis is the Littrow angle for wavenumber  $\sigma_0$ . The angle  $\phi$  between  $\vec{k}$  and the  $x$ - $z$  plane is not shown.

---

---

**Figure 2.2** Same as Figure 2.1 except for grating  $G_2$

---

**Figure 2.1****Figure 2.2**

and outgoing rays in the dispersion plane, and  $\phi$  is the angle between the wavevector and the dispersion plane. The grating equation, expressed in terms of incoming angles  $\beta$  and  $\phi$  and outgoing angles  $\beta_i$  and  $\phi_i$  defined in figures 2.1 and 2.2, is

$$\sin(\theta \mp \beta_{1,2}) - \frac{2\sigma_0 \sin \theta}{\sigma \cos \phi} - \sin(\theta \mp \beta) = 0 \quad (2.4)$$

$$\phi_{1,2} = -\phi.$$

In equation 2.4, subscripts 1 and 2 denote angles associated with the outgoing wavevectors  $\vec{k}_1$  and  $\vec{k}_2$  and  $m/a = 2\sigma_0 \sin \theta$  where  $\sigma_0$  and  $\theta$  are the Littrow wavenumber and angle, respectively. For a plane wave incident at angles  $\beta$  and  $\phi$ , the Fizeau fringe pattern produced by the basic SHS system as a function of  $x$ ,  $y$ , and  $z$  is obtained by substituting the outgoing angles predicted by equation 2.4 into equation 2.3 and then substituting equation 2.3 into equation 2.2. By adding the Fizeau fringe patterns produced by incident wavefronts at all angles and wavenumbers admitted into the system, the complete Fizeau fringe pattern is determined.

**2.3 First Order Axial Analysis:** For a monochromatic point source on

axis at the input aperture,  $\beta = 0$  and  $\phi = 0$ . Substituting this into equation 2.4 and expanding to first order in  $\beta_{1,2}$  gives

$$\beta_{1,2} = \pm 2 \tan \theta \left( \frac{\sigma - \sigma_0}{\sigma} \right). \quad (2.5)$$

Substituting this result into equation 2.2 via equations 2.3 gives

$$I(x) = I_0 (1 + \cos(2\pi(4(\sigma - \sigma_0)x \tan \theta))). \quad (2.6)$$

Equation 2.6 is independent of  $y$  and  $z$  (the fringes are non-localized) since equation 2.3 predicts  $k_{y1} - k_{y2}$  and  $k_{z1} - k_{z2}$  to first order in  $\beta_{1,2}$ . For an on-axis polychromatic source, equation 2.6 can be written

$$I(x) = \int_0^\infty B(\sigma) (1 + \cos(2\pi(4(\sigma - \sigma_0)x \tan \theta))) d\sigma \quad (2.7)$$

where  $B(\sigma)d\sigma$  is the intensity at  $\sigma$ .

It is important to emphasize some aspects of equation 2.7. With the exception of the constant term,  $I(x)$  represents a Fourier transform of the input spectrum. Note that zero frequency corresponds to  $\sigma = \sigma_0$  and no element has been mechanically scanned in this process. Effectively, SHS instruments record the path difference scanned by FTS on a position sensitive

detector without scanning, and heterodyne the interferogram with a frequency corresponding to the Littrow wavenumber of the gratings.

To compare the interferograms produced by SHS and FTS systems, it is convenient to introduce a transformation of variables in equation 2.7. The SHS interferogram can be expressed as a function of the optical path difference recorded by the system at position  $x$  on the diffraction grating by making the substitution

$$u = 4x \tan \theta. \quad (2.8)$$

The input spectra in the SHS system can be symmetrized by defining

$$B_e(\sigma') = \frac{1}{2}(B(\sigma') + B(-\sigma')) \quad (2.9)$$

where  $\sigma' = \sigma - \sigma_0$ . This is a generalization of the relationship  $B_e(\sigma) = (B(\sigma) + B(-\sigma))/2$  often applied in the analysis of FTS systems (Vanasse & Sakai, 1966; Brault, 1985) and accounts for the symmetry in the recovered transform. After making these changes, equation 2.7 can be written

$$I(u) = \int_{-\infty}^{\infty} B_e(\sigma')(1 + \cos(2\pi\sigma'u)) d\sigma' \quad (2.10)$$

where  $I$  is now considered a function of path difference  $u$ . This relation has

the same form as the equation that typically describes the interferogram in conventional FTS. It should be kept in mind, however, that the variable  $\sigma'$  measures the spectrum in terms of *differences* in wavenumber from  $\sigma_0$ .

**2.4 Resolving Power:** In general, the raw output of any spectrometer represents the convolution of the input spectrum with the system's instrumental profile. If the profile of a monochromatic source is measured by an instrument, the raw spectrum represents the instrumental profile which, in turn, determines the resolution limit  $\delta\sigma$  of the instrument. By setting  $B(\sigma') = \delta(\sigma'_1 - \sigma')$  in equation 2.9, the response of the basic SHS systems given by equation 2.10 is

$$I(u) = \cos(2\pi u \sigma'_1) \quad (2.11)$$

where  $\sigma'_1 = \sigma_1 - \sigma_0$  and the constant term has been removed. Since  $I(u)$  is measured only over a finite range of  $u$  ( $-U < u < U = u_{max}$ ), in the simplest case, the transform of equation 2.11 can be written

$$P(\sigma' - \sigma'_1) = \int_{-\infty}^{\infty} \Pi\left(\frac{u}{2U}\right) \cos(2\pi u \sigma'_1) \cos(2\pi u \sigma') du \quad (2.12)$$

where the rectangle function  $\Pi(x) = 1$  for  $-0.5 < x < 0.5$  and zero for  $x < -0.5$

and  $x > 0.5$ . The instrumental profile (convolving function) is then

$$P(\sigma' - \sigma'_1) = 2U \{ \text{sinc}[2U(\sigma' - \sigma'_1)] + \text{sinc}[2U(\sigma' + \sigma'_1)] \} \quad (2.13)$$

where the  $\text{sinc}(x) = \sin(\pi x)/\pi x$ . The width of the sinc functions in equation 2.13 determine the resolution limit of the system. Defining  $\delta x - 1$  as the characteristic width of  $\text{sinc}(x)$  (Vanasse & Sakai, 1966; Brault, 1985), equation 2.13 determines the resolution limit of the system as  $|\sigma' - \sigma'_1| = \delta x - 1/2U$ . An alternate derivation of this resolution limit follows from defining the resolution as the wavenumber interval over which the number of detected fringes changes by one. Adopting either of these definitions for the resolution limit and setting  $U = 4x_{\max} \tan\theta$  where  $x_{\max} = (W \cos\theta)/2$ , the resolving power of the system shown in Figure 1.1 is given by

$$R_0 = 4W\sigma \sin\theta. \quad (2.14)$$

Note that equation 2.14 is equal to the theoretical resolving power of the dispersive elements in the system. In general, SHS instruments achieve a resolving power characteristic of the dispersive elements in the system.

Equation 2.13 predicts two sinc functions for a monochromatic input because the system, as described so far, produces an identical response for wavenumbers  $+\sigma'$  and  $-\sigma'$  as a result of the symmetry of the cosine

interferogram (cf. equation 2.11). In the FTS case, the symmetry of the cosine interferogram produces ghost spectra at negative wavenumbers which are regarded as unphysical. However, in the heterodyned system signal at negative wavenumbers could be real and lead to ambiguous results. By careful experimental design and technique, difficulties associated with this ambiguity can be avoided for many problems. For problems requiring unambiguous recovery, a method utilizing a two-dimensional format to break the symmetry in the cosine interferogram will be described in Chapter 3.

**2.5 Fringe Localization:** As described in section 2.2, the intensity of light seen at a particular point in the interferometer is the superposition of fringe patterns from all wavenumbers and angles. For the case of a monochromatic point source in the input aperture, discussed in section 2.3, a single plane wave is incident on each grating and non-localized fringes are produced in the interferometer. With a finite aperture, plane waves are incident on the gratings at various angles and the sum of the intensities of the overlapping fringe patterns averages to a uniform value at most points in space. The fringes become localized in a particular plane determined by the point where the spatial phase of the fringe patterns coincide. This plane can be determined for the basic SHS system using the framework derived in section 2.2. Using the quantities defined above, the argument of the cosine

function in equation 2.2 can be written as

$$\delta = (k_{x1} - k_{x2})x + (k_{z1} - k_{z2})z. \quad (2.15)$$

The phase does not depend upon  $y$  since the combination of equations 2.3 and 2.4 give  $k_{y1} - k_{y2}$ . If a line  $(x_0, z_0)$  can be found where equation 2.15 satisfies  $\delta = 0$  independent of wavenumber and incident angle, spatial frequencies from the various fringe patterns will all be in phase along the line and the localization plane will be given by  $z - z_0$ . The image of the line  $(x_0, z_0)$  is also the position of zero-path difference in the interferogram since  $\delta = 0$  there and all pairs of exit wavefronts will exhibit constructive interference along the line. For the system under consideration, equation 2.15 gives  $\delta = 0$  at the point  $(x_0, z_0) = (0,0)$  and the fringes are localized in the x-y plane of Figures 2.1 and 2.2. The exit optics should image this plane, nominally the plane of the gratings, on the detector. This simple result stems from the assumption  $\varepsilon_1 - \varepsilon_2 = 0$  in equation 2.1 for this system. The assumption is valid for the case of a symmetric system where the coordinate systems in Figures 2.1 and 2.2 are exactly the same distance from the beam splitter and any phase shifts introduced upon diffraction are the same in the two arms. To maintain the symmetry a compensating plate has been assumed

as part of the beam-splitter in figure 1.1. If the compensating plate is absent, the position of one of the gratings should be adjusted so the optical path in the two arms of the interferometer are the same for a given wavenumber. Dispersion effects introduced by the beam splitter must then be considered in the analysis.

**2.6 Off Axis Analysis:** In addition to localizing the fringe plane, enlarging the input aperture increases the sensitivity of the instrument because more light is admitted into the system. This increase in sensitivity must be weighed against a reduction in fringe contrast resulting from the dependence of fringe frequency on off-axis angle. Similar trade-offs are encountered in the analysis of every spectroscopic system. In order to calculate the limitation on the field of view, an analysis developed for FTS by Brault (1985) will be adapted for the basic SHS system.

The intensity  $dI$  detected by the system when viewing solid angle  $d\Omega$  can be expressed

$$dI(x) = \int_{-\infty}^{\infty} B(\sigma)(1 + \cos((k_{x1} - k_{x2})x)) d\Omega d\sigma \quad (2.16)$$

where equation 2.15 has been used with  $z=0$ . Expanding the grating equation (eq. 2.4) to first order in  $\sigma'/\sigma$  and second order in angles and substituting into

equation 2.3 gives

$$\begin{aligned} k_{x1} &= 2\pi(2\sigma'\tan\theta - \sigma\beta) - 2\sigma\Omega\tan\theta \\ k_{x2} &= 2\pi(-2\sigma'\tan\theta - \sigma\beta) + 2\sigma\Omega\tan\theta \end{aligned} \quad (2.17)$$

where  $\Omega \sim \pi(\beta^2 + \phi^2)$  is the solid angle viewed by the instrument. Substituting equation 2.17 into equation 2.16 and changing variables to  $\sigma'$  and  $u$ , equation 2.16 can be written

$$dI(u) = \int_{-\infty}^{\infty} B_e(\sigma') d\sigma' \left[ 1 + \cos\left(2\pi u(\sigma' - \sigma \frac{\Omega}{2\pi})\right) \right] d\Omega. \quad (2.18)$$

Integrating equation 2.18 over solid angle from 0 to  $\Omega_m$  results in

$$\begin{aligned} I(u) &= \Omega_m \int_{-\infty}^{\infty} B_e(\sigma') d\sigma' [1 + \\ &\quad \text{sinc}\left(\frac{u\sigma\Omega_m}{2\pi}\right) \cos(2\pi u(\sigma'(1 - \frac{\Omega_m}{4\pi}) - \frac{\sigma_0\Omega_m}{4\pi}))]. \end{aligned} \quad (2.19)$$

The leading  $\Omega_m$  represents the increase in fringe amplitude due to a finite field of view while the sinc function reduces the contrast of the fringes at large path differences.

The criterion most commonly adopted to obtain the maximum tolerable field of view is to determine the maximum fringe amplitude at the longest path difference (usually fixed by resolving power considerations) for the highest wavenumber measured (Brault, 1985). The amplitude of the fringes at the longest path difference,  $u_{\max} - U$ , produced by the interferometer is, from equation 2.19,

$$\Omega_m \operatorname{sinc}\left(\frac{U\sigma\Omega_m}{2\pi}\right) - \frac{2}{U\sigma} \sin\left(\frac{U\sigma\Omega_m}{2}\right) \quad (2.20)$$

which has a maximum at  $\Omega_m = \pi/U\sigma$ . Using equations 2.8, 2.14, and  $x_{\max} = W\cos\theta/2$ , the limiting field of view is determined as  $\Omega_m = 2\pi/R$ . This is the field of view typically used for conventional Fabry-Perot and FTS interferometers. The basic SHS system enjoys the same gains in throughput over conventional grating spectroscopy as the conventional systems.

A simple calculation shows the condition  $\Omega_m = 2\pi/R$  is equivalent to increasing the field of view until the total number of fringes produced by the extreme rays in the system differs by one from the number produced by the axial rays. This rule of thumb will be referred to later to derive the field of view for other SHS systems.

The effect of a finite field of view on the fringe frequency is to scale

$\sigma'$  by the quantity  $1 - \Omega_m/4\pi$  and to shift the frequency by  $\sigma_0 \Omega_m/4\pi$  (cf. equation 2.19). In practice, these shifts are taken into account when calibrating the wavenumber scale by measuring two spectral lines of known wavenumber. Strictly speaking, however,  $\sigma'$  should be redefined as

$$\sigma' = (\sigma - \sigma_0) - \frac{\sigma \Omega_m}{4\pi} \quad (2.21)$$

in all of the above equations.

**2.7 Higher Order Frequency Shifts:** The analysis leading to equation 2.19 is valid only to first order in  $\sigma'/\sigma$ . When higher order terms in  $\sigma'/\sigma$  cannot be neglected, the phase of the interferogram is non-linear and SHS systems technically do not produce a true Fourier transform of the spectrum. The magnitude of the shift can be estimated by including second order  $\sigma'/\sigma$  terms in the expansions that led to equation 2.19. The shift, as a result of the addition of the second order term, can be expressed in terms of a change in the total number of fringes detected as

$$\Delta n = -\frac{n_1^2}{R} \tan^2 \theta \quad (2.22)$$

where  $n_1 - 2U\sigma'$  is the number of fringes predicted by the first order analysis.

**2.8 Effect of Finite Aperture on the Instrument Function:** As demonstrated in section 2.7, an effect of a finite aperture is the reduction in the fringe modulation as the path difference increases. The reduction in fringe modulation effects the instrument function because the envelope of the cosine interferogram for light of wavenumber  $\sigma_1$  is given by

$$\Omega_m \text{sinc}\left(\frac{u\sigma_1\Omega_m}{2\pi}\right) \cdot \prod \left(\frac{u}{2U}\right). \quad (2.23)$$

The Fourier transform of this equation is the instrumental profile and is given by

$$P(\sigma') = [\Omega_m \prod \left(\frac{2\pi\sigma'}{\sigma_1\Omega_m}\right)] * [2U \text{sinc}(2U\sigma')] \quad (2.24)$$

where the  $*$  denotes a convolution. In addition to convolving the spectrum with a sinc function as before, the spectrum is also convolved with a rectangle of width  $w = \sigma_1\Omega_m/2\pi$  or, if the maximum aperture is used,  $w = \sigma_1/R$ . In this case, the rectangle is one resolution element wide which increases the width of the instrumental profile slightly. A numerical calculation of this instrumental profile is shown in Figure 2.3.

**2.9 Spectral Range/Sampling:** For conventional FTS, the spectral range is typically determined by the number of samples obtained in the

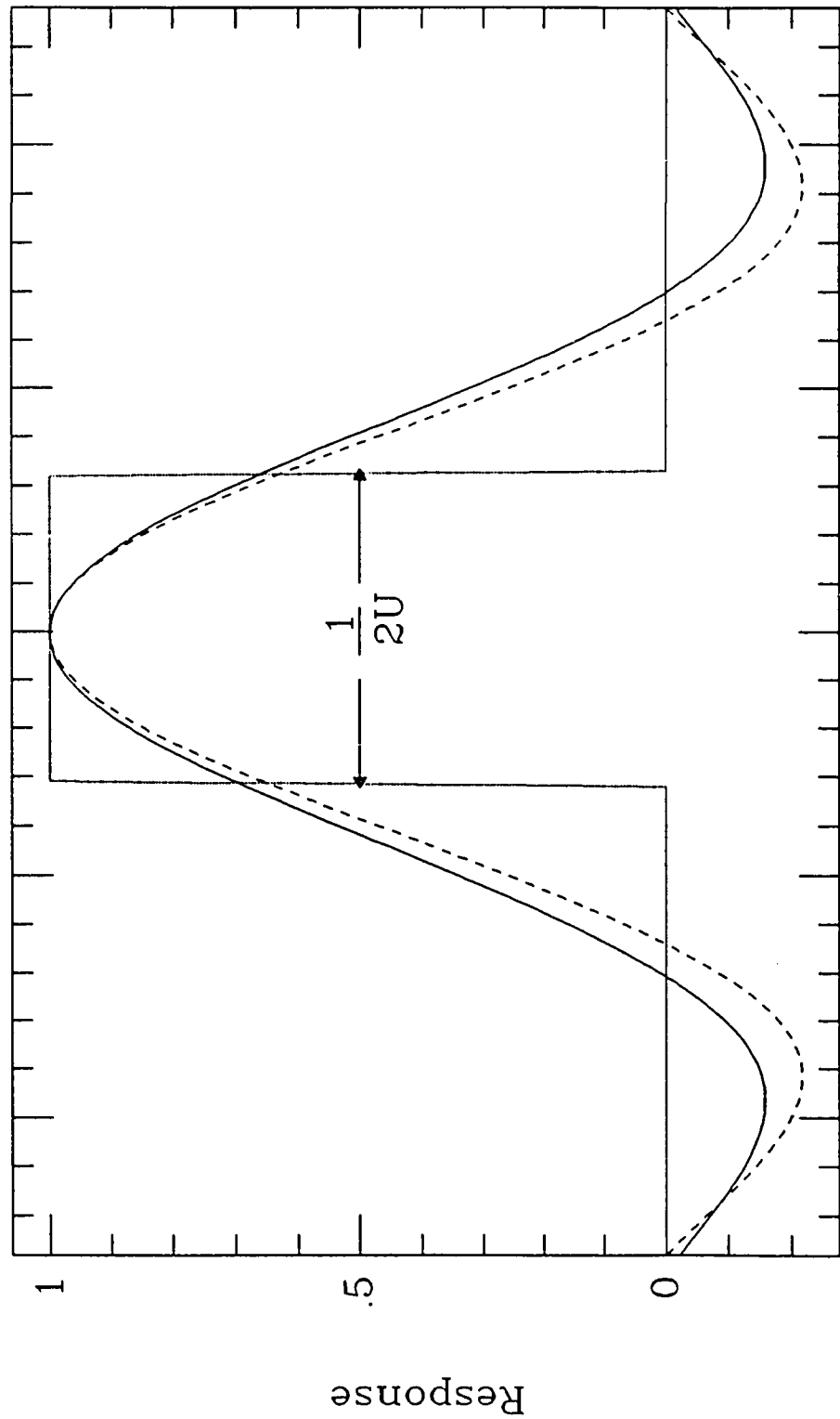
interferogram. In the unaliased case, the highest recoverable wavenumber,  $\sigma_{\max}$ , is related to the sampling interval by the relationship  $\sigma_{\max} \leq 1/2 \delta u$ , where  $\delta u$  is the sampling interval (Bell, 1972; Sakai, 1977; Brault, 1985). This is a statement of Nyquist's theorem from communications theory which states that in order to recover a spectrum unambiguously, the sampling frequency must be at least twice as great as the highest frequency in the spectrum. The spectral range in FTS can also be expressed in terms of the total number of samples obtained in the interferogram as  $N - 2\sigma_{\max}/\delta\sigma$ . In SHS, this relationship is also valid if  $\sigma$  and  $\delta\sigma$  are replaced by  $\sigma'$  and  $\delta\sigma'$ . Nyquist's theorem continues to hold in SHS systems where it is applied to *heterodyned* frequencies; thus, the number of resolution elements obtained is equal to half the number of samples obtained. The non-aliased spectral range is then determined by the number of resolution elements times the resolution limit or  $\sigma'_{\max} = N\delta\sigma'/2$ .

Sampling the interferogram with an array detector of discrete finite width pixels introduces a distortion in the intensity distribution recovered by SHS systems; this distortion is not seen with the comb function sampling typically used in conventional FTS. A discussion of this effect, as well as the effects of sampling on the signal-to-noise ratio obtained in the spectrum, will

**Figure 2.3** Instrumental profile expected for the basic SHS system:  
The expected instrumental profile for the basic SHS system is shown by the  
solid curve which represents the convolution of  $\text{sinc}(2U\sigma')$  (dashed curve)  
with  $\prod(2U\sigma')$  (dotted curve).

---

Figure 2.3: SHS Instrumental Profile



Spatial Frequency (arbitrary units)

be deferred to Chapter 6.

### 3. SHS Systems with Two Dimensional Detectors

**3.1 Introduction:** As demonstrated in previous chapters, the symmetric heterodyned interferogram recorded by SHS systems leads to an ambiguity in the spectra recovered by them. The ambiguity is a result of the systems producing identical output for wavenumbers  $+\sigma'$  and  $-\sigma'$ ; hence, the recovered spectra are effectively folded about the point  $\sigma - \sigma_0$ . Discussed in this chapter are a two-dimensional fringe format which removes this ambiguity and first order tests of an SHS instrument employing the two-dimensional technique. Also discussed is a description of the SHS echelle concept which utilizes the two-dimensional format to increase the number of spectral elements that can be recovered. The implementation of the echelle system is modeled and the results presented. The chapter concludes with a reconsideration of the fringe localization and etendue issues related to the two-dimensional format.

**3.2 The Two-Dimensional Technique:** The ambiguity associated with the "true" and "ghost" spectra, illustrated in Figure 1.5, can be eliminated by utilizing a two-dimensional format in the basic SHS system. The ambiguity is eliminated by rotating one of the gratings in the basic system by a small angle,  $\alpha/2$ , about an axis perpendicular to the optical axis and the grooves of

**Figure 3.1** Adjustment of the basic SHS system to achieve the two-dimensional format: If grating  $G_2$  is rotated by an angle  $\alpha/2$  about the x axis, the symmetry with respect to wavenumber is broken in the cosine interferogram produced by the basic SHS system.

---

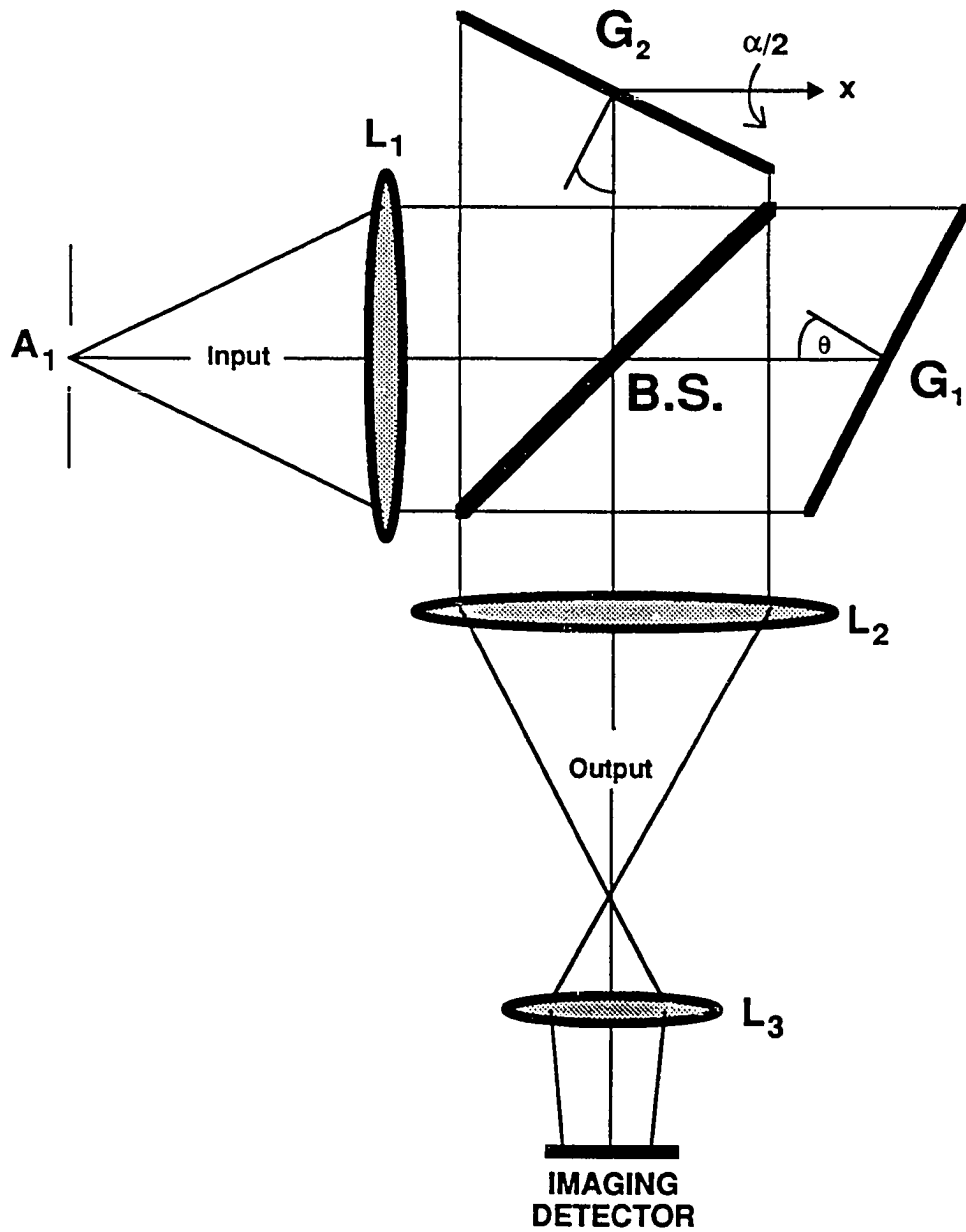


**Figure 3.1**

the grating. This is illustrated in Figure 3.1 where grating  $G_2$  has been slightly rotated about the  $x$  axis. The tilt introduces a spatial modulation perpendicular to the modulation produced by the grating dispersion. The fringes recorded by this system are no longer parallel to the  $y$  axis; rather, they are functions of both  $x$  and  $y$  and exhibit a wavenumber dependent rotation. The dependence is shown by considering the response of the system to a monochromatic point source on the axis of the input aperture. When a tilt of  $\alpha/2$  is introduced, the interferometer produces output wavefronts whose normal vectors are characterized by angles

$$\begin{aligned}\beta_{1,2} &= \pm 2 \tan \theta \left( \frac{\sigma - \sigma_0}{\sigma} \right) \\ \phi_2 &= -\alpha.\end{aligned}\quad (3.1)$$

The interferogram is then recast as

$$I(x,y) = \int_0^\infty B(\sigma) [1 + \cos(2\pi(4(\sigma - \sigma_0)x \tan \theta + \sigma y \alpha))] d\sigma \quad (3.2)$$

(cf. equation 2.7). For  $\sigma = \sigma_0$ , Fizeau fringes parallel to the  $x$  axis with spatial frequency  $f_y - \sigma\alpha$  are recorded. The fringes recorded for arbitrary wavenumber are rotated with respect to the  $x$  axis by an angle  $\eta$  where  $\tan \eta = -f_x/f_y$  ( $f_x = 4(\sigma - \sigma_0)\tan \theta$ ). If  $\sigma > \sigma_0$ , then  $f_x < 0$  and  $\eta < 0$ , and if  $\sigma < \sigma_0$ ,

then  $f_x > 0$  and  $\eta > 0$ . Recording this pattern on a two-dimensional detector and performing a two-dimensional Fourier transform completely separates the spectra that are superimposed in the one-dimensional case.

For monochromatic input, the two-dimensional transform of the fringe pattern predicted by equation 3.2 will consist of sinc functions (each two-dimensional) at the points  $(+4\sigma'\tan\theta, +(\sigma_0 + \sigma')\alpha)$  and  $(-4\sigma'\tan\theta, -(\sigma_0 + \sigma')\alpha)$  in the  $(f_x, f_y)$  plane. The addition of the cross tilt separates the ambiguous spectra from the one-dimensional case by using the positive  $f_y$  half-plane to record one of the overlapping spectra and the negative half-plane to record the other. Except for the sign of the quantity  $\delta\sigma/\delta f_x$ , the spectral content of these half-planes is identical. The recovered transform is symmetric about the point  $(f_x, f_y) = (0,0)$ .

**3.3 First Order Two dimensional Tests:** Tests of the two-dimensional concept were performed on the system shown in Figure 3.1 using the sodium source employed in the system tests in Chapter 1. Figure 3.2 shows the fringe pattern recorded on the CCD system when one of the gratings in the basic system was tilted. The adjustment was selected approximately half-way between the two lines to produce roughly equal and opposite fringe rotations.

---

**Figure 3.2** Photograph of the fringe pattern formed by the Na doublet when gratings are adjusted for the two-dimensional format: The adjustment was selected approximately half-way between the two lines to produce roughly equal and opposite fringe rotations.

---

Figure 3.2

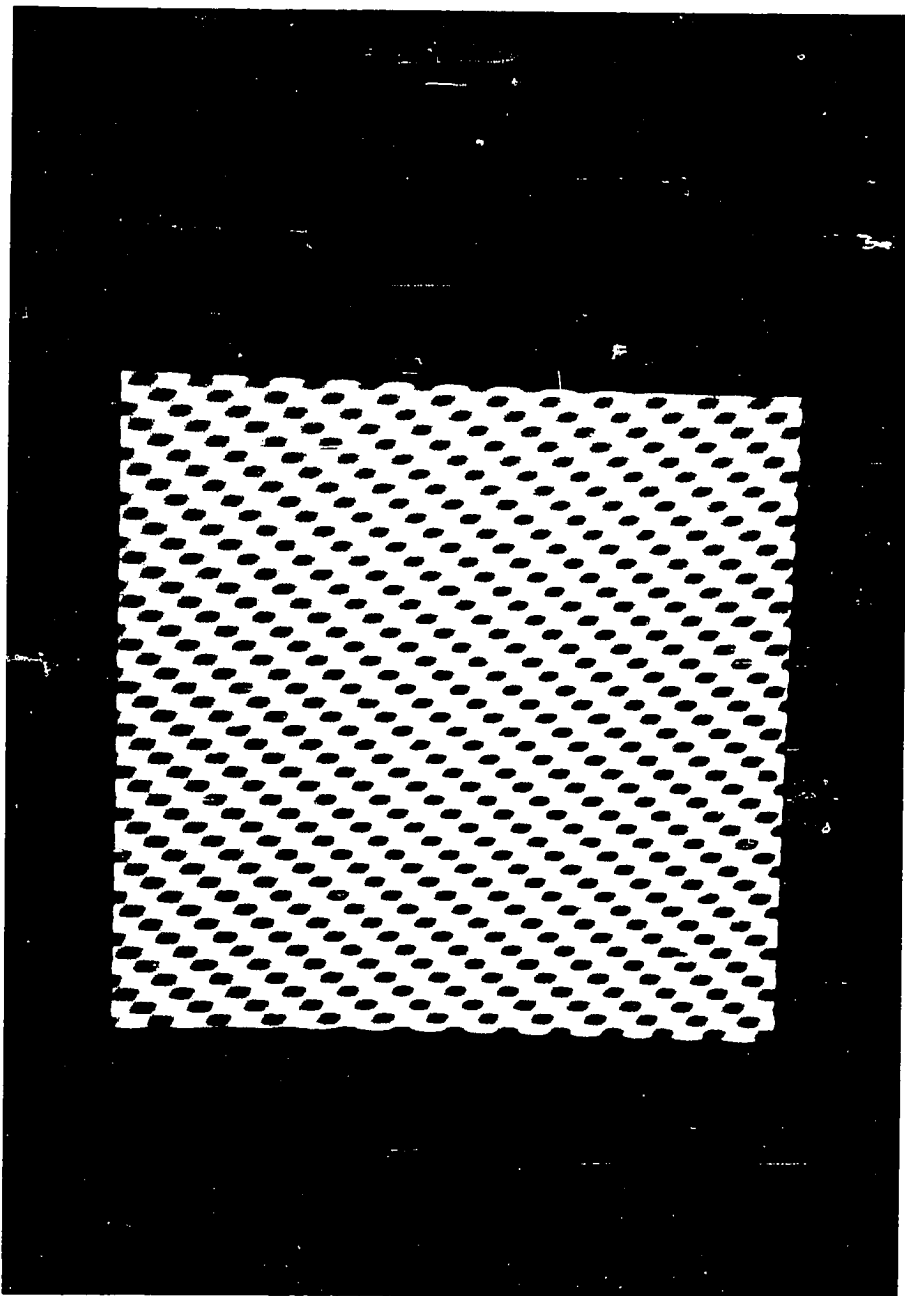


Figure 3.3 shows the two-dimensional amplitude Fourier transform of this pattern. Spectral information is recorded along the spatial frequency axis and "true" and "ghost" spectra are clearly separated along the order axis.

**3.4 Echelle SHS Configuration:** Substituting the variables  $\sigma'$  and  $u$ , discussed in Chapter 2, and defining the optical path difference along the  $y$  direction as  $v = \alpha y$ , equation 3.2 can be written

$$I(u, v) = \int_0^{\infty} B(\sigma) d\sigma (1 + \cos(2\pi(\sigma' u + \sigma v))). \quad (3.3)$$

Inspection of equation 3.3 reveals that the interferogram records a heterodyned Fourier transform of the spectrum as a function of  $u$ , but a non-heterodyned transform is recorded as a function of  $v$ .

This form, with high resolution in one dimension and low resolution in the other, is analogous to an echelle spectrograph where a grating with relatively coarse groove density is used in multiple orders. The multiple orders are then sorted by a low resolution cross dispersing grating, typically used in first order. The spectrum is detected by imaging the entrance slit onto a two-dimensional detector where bands of light are recorded separated in the cross dimension by the cross disperser. Echelle spectrographs typically achieve high spectral resolving power and a wide bandwidth with the

---

**Figure 3.3** Two-dimensional amplitude Fourier transform of the fringe pattern shown in Figure 3.2: Spectral information is displayed along the frequency axis and "true" and "ghost" spectra are separated along the order axis. Note the symmetry in the transform about the 0,0 point.

---

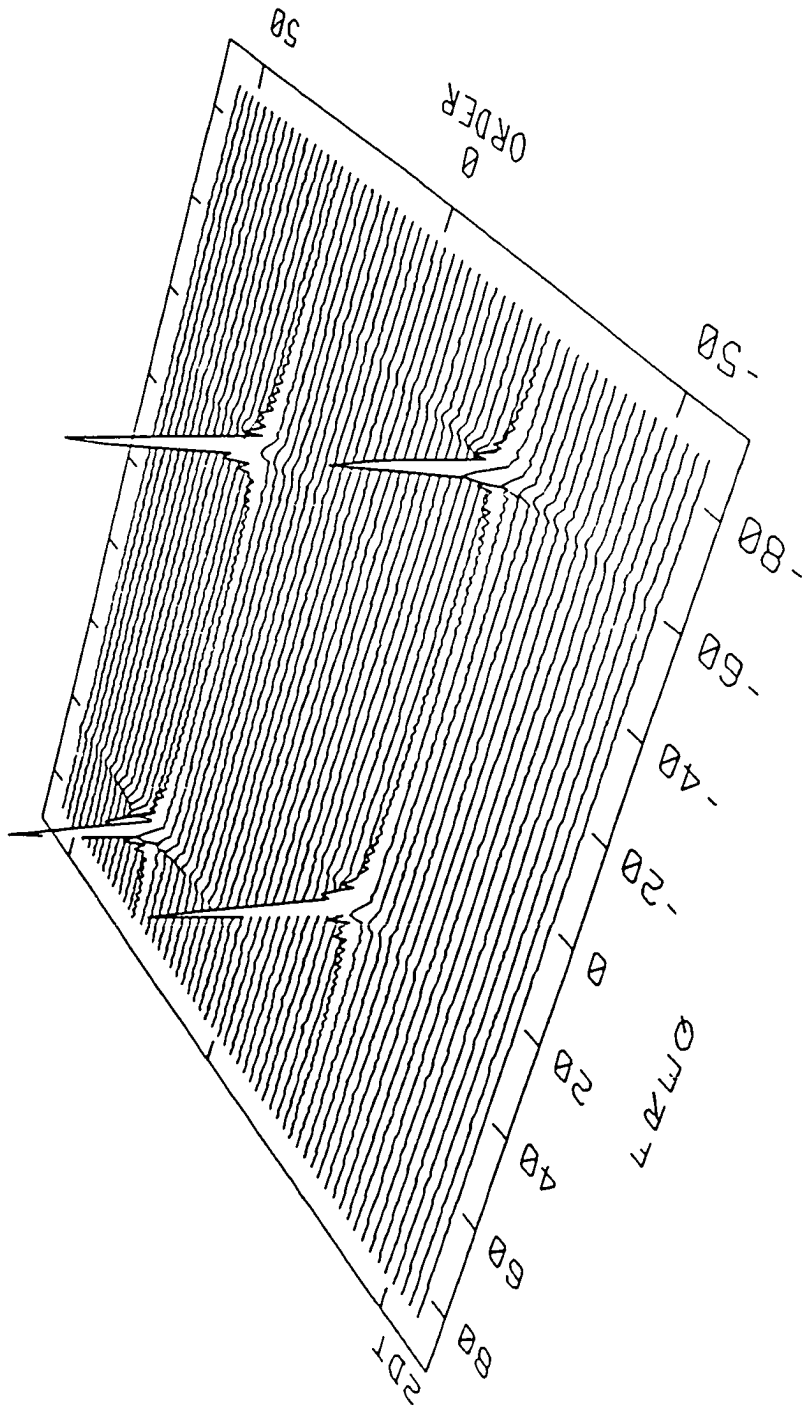


**Figure 3.3**

convenience of two-dimensional array detectors.

When the gratings in Figure 3.1 are used in multiple order, the system has a number of  $\sigma_0$ 's (one from each order). The low resolution transform provided by the cross tilt in the v dimension can separate these orders. The tilt  $\alpha/2$  must be large enough so the series of Littrow wavenumbers differ by at least one fringe in the v dimension and the spectral range in a given order must be small enough (as determined by the properties of the grating) so light at the ends of the order do not produce aliased signals at the detector. A two-dimensional Fourier transform of the Fizeau fringes produced by this device will recover the echelle spectrograph format with high dispersion along u and low dispersion along v.

When the gratings in the basic SHS system are used in multiple orders, and the two-dimensional format is employed, the intensity distribution recorded on the imaging detector is given by

$$I(u,v) = \sum_m \int_0^{\infty} B(\sigma) d\sigma F_m(\sigma) (1 + \cos(2\pi(\sigma'_m u + \sigma v))) \quad (3.4)$$

where m denotes the order number,  $F_m(\sigma)$  gives the blaze efficiency for order m, and  $\sigma'_m = \sigma - \sigma_{0m}$ . The blaze efficiency  $F_m(\sigma)$ , in the simplest analysis, is

determined by the single slit diffraction from a single groove facet on the grating (Miller & Roesler, in press).  $F_m(\sigma)$  can be expressed as

$$F_m(\sigma) = \text{sinc}^2\left(\frac{\sigma - \sigma_{0m}}{\sigma_{01}}\right). \quad (3.5)$$

In equation 3.5,  $\sigma_{0m}$  denotes the Littrow wavenumber for order  $m$  which is given by

$$\sigma_{0m} = \frac{m}{2a \sin \theta} \quad (3.6)$$

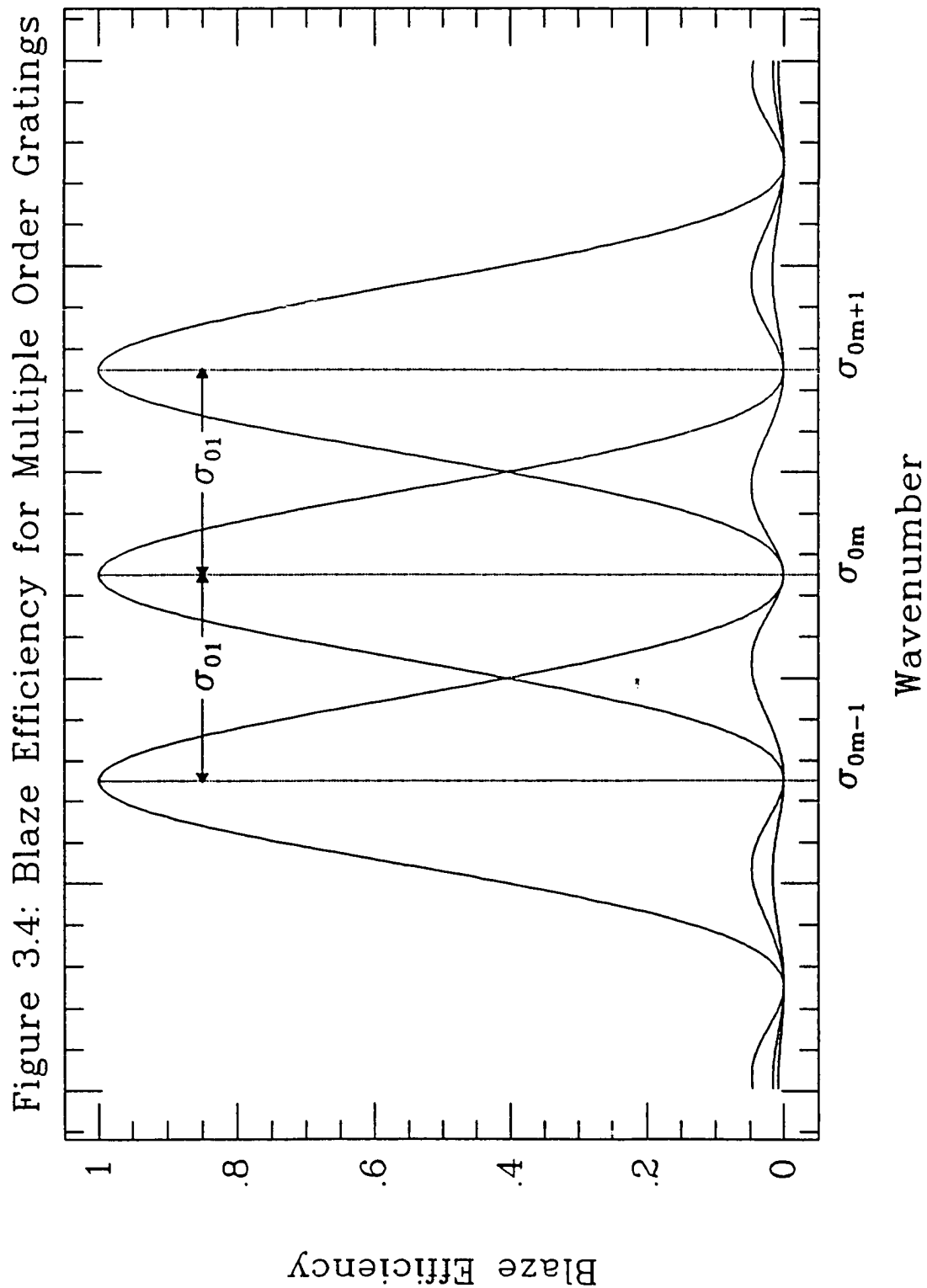
where  $1/a$  is the groove density and  $\theta$  is the grating angle. A plot of the blaze efficiency predicted by equation 3.5 for orders  $m-1$ ,  $m$ , and  $m+1$  is shown in Figure 3.4. Each order has an effective spectral range of  $\sigma_{0m} \pm \sigma_{01}$  while adjacent orders are separated in wavenumber by  $\sigma_{01} - 1/2a \sin \theta$ .

**3.5 Spectral Range/Sampling:** In the echelle SHS configuration, the spectral range for a particular order of the gratings must be less than the limiting spectral range determined by sampling considerations. If  $N_u$  samples are obtained along  $u$ , then the maximum measurable spectral range in this dimension is given by  $N_u \delta \sigma$ . Comparing this to the spectral range of one

---

**Figure 3.4** Blaze efficiency for multiple order gratings: The efficiency of diffraction for three orders of a diffraction grating as a function of wavenumber. Adjacent orders are separated in wavenumber by  $\sigma_{01} - 1/2a\sin\theta$  and each order has an effective spectral range equal to  $2\sigma_{01}$ .

---



order of the gratings,  $2\sigma_{01}$ , an upper limit for the number of samples required along u is

$$N_u \geq \frac{2\sigma_{01}}{\delta\sigma}. \quad (3.7)$$

The number of samples required in the high resolution dimension is twice the first order resolving power of the grating combination. Since SHS systems achieve the theoretical resolution of the dispersive elements in the system, equation 3.7 may be interpreted as requiring the number of samples in the u dimension to be at least twice the total number of grooves on the diffraction gratings.

In the cross dispersion dimension, the resolution of the transform in v must be high enough to distinguish adjacent orders from one another by a differential of at least one fringe. If the orders are to be completely resolved (the intensity going to zero between each), there must be a differential of two fringes between adjacent orders. It can be shown that this requirement is met if  $n_v - 2m$  where  $n_v$  is the number of fringes in the v dimension and m is the order number of the gratings. The number of samples along v must be at least twice this number or

$$N_v \geq 4m_{\max} \quad (3.8)$$

where  $m_{\max}$  is the highest order of the gratings. This analysis also leads to a relationship for the magnitude of the angular tilt  $\alpha$  required to separate the grating orders. If the orders are to be separated by at least two fringes, then

$$\alpha \geq \frac{2}{W_v \sigma_{01}} \quad (3.9)$$

where  $W_v$  is the width of the grating in the v dimension.

**3.6 SHS Echelle Simulation:** To verify the above concepts, a computer simulation of the SHS echelle configuration was performed. A relatively small detector format of 64 x 64 was chosen so results of the simulation could be easily displayed. This small detector format leads to diffraction gratings with unusually low groove densities when a practical aperture is used. The large groove size does not pose a problem for a computer simulation, but for a practical system, a larger detector format is probably desirable.

The sampling requirements derived in section 3.4 place limits on the maximum order number and resolution of the system. With a 64 x 64 element detector array, equation 3.8 requires  $m_{\max} \leq 16$  while equation 3.7 requires  $R_1 = \sigma_{01}/\delta\alpha - 32$ . Arbitrarily choosing to work in grating orders 6 through 10 and restricting the bandpass of the instrument to the visible spectral region

( $\sigma \leq 25,000 \text{ cm}^{-1}$ ), the resolution limit  $\delta\sigma$  of the system is determined by the relationships  $25,000 \text{ cm}^{-1} = \sigma_{01} m_{\max}$  and  $\sigma_{01} = 32\delta\sigma$ . Combining these two relationships results in  $\delta\sigma = 80 \text{ cm}^{-1}$  and  $\sigma_{01} = 2560 \text{ cm}^{-1}$ . The gratings required to achieve these specifications have groove facets of width  $a = 2W/R_1$ . If a 25 mm grating aperture is assumed,  $a = 1.56 \text{ mm}$ . The grating angle is given by  $\sin\theta = 1/2a\sigma_{01}$  or, if the above parameters are used,  $\theta = 0.072^\circ$ . The spectral range encompassed by each order is tabulated in table 3.1. The magnitude of the cross tilt  $\alpha$  was chosen by equation 3.9 with  $W_v = 25 \text{ mm}$ .

**Table 3.1**

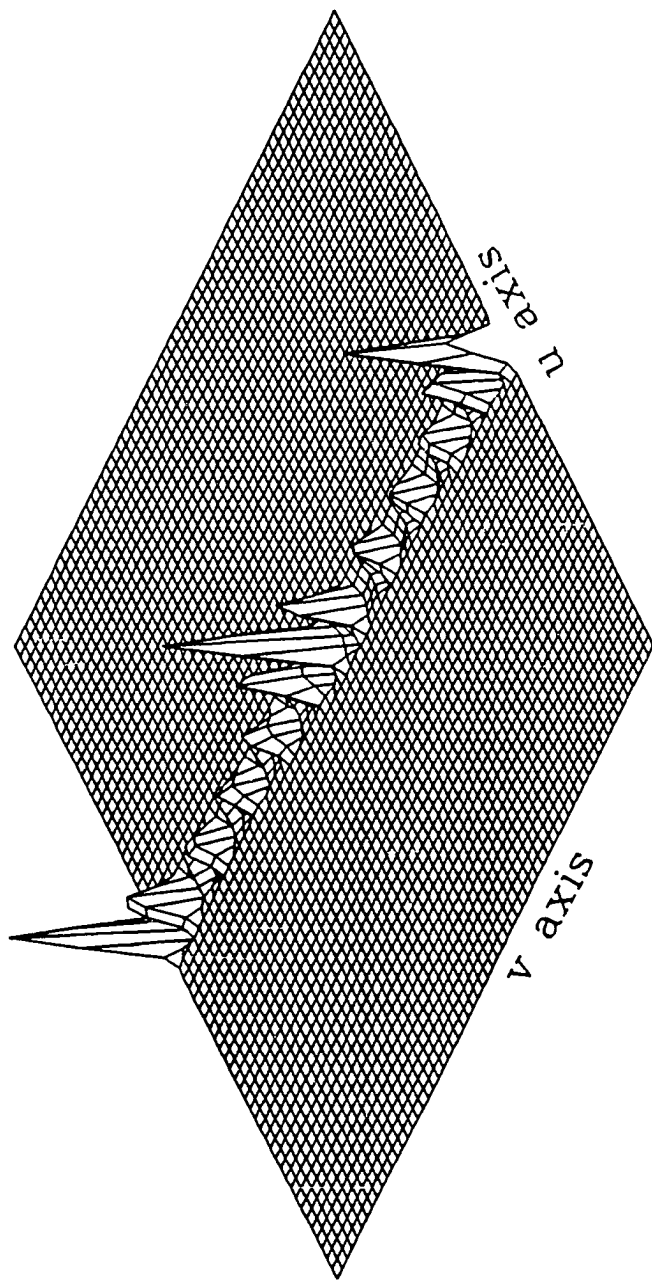
| Order number | Spectral Range $\text{cm}^{-1}$ |
|--------------|---------------------------------|
| 6            | 12800-17920                     |
| 7            | 15360-20480                     |
| 8            | 17920-23040                     |
| 9            | 20480-25600                     |
| 10           | 23480-28160                     |

---

**Figure 3.5** Modeled intensity distribution for the SHS echelle simulation: Intensity distribution predicted by equation 3.4 for the SHS echelle system simulation (described in the text).

---

Figure 3.5: SHS Echelle Modeled Intensity Distribution



---

**Figure 3.6** Two-dimensional Fourier transform of the pattern shown in Figure 3.5: See text for details.

---

Figure 3.6: SHS Echelle Simulation

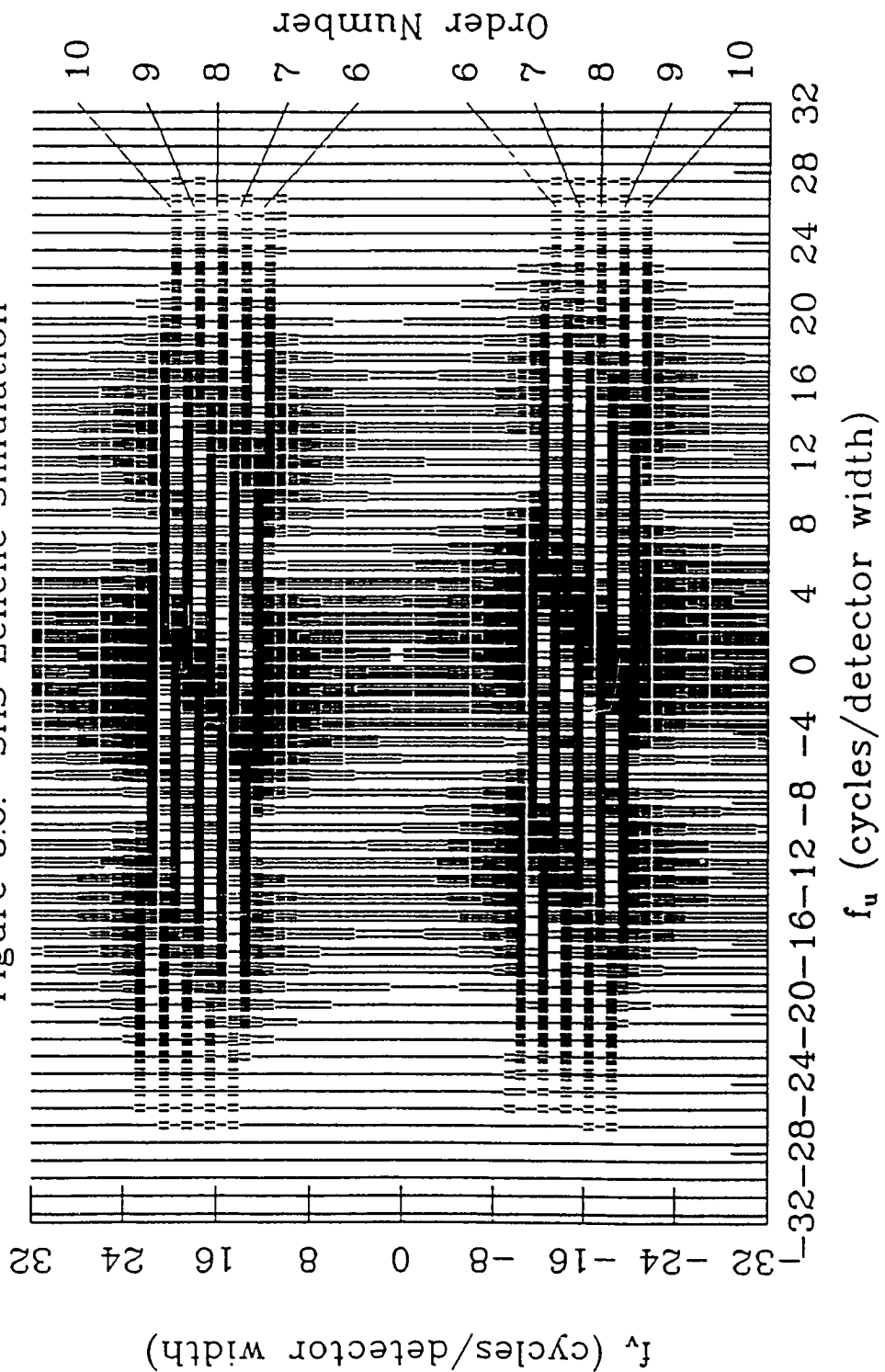


Figure 3.5 shows the modeled intensity distribution recorded on the detector assuming a source uniform in wavenumber between  $12,800 \text{ cm}^{-1}$  and  $28,000 \text{ cm}^{-1}$ . Figure 3.6 shows a halftone representation of the two-dimensional Fourier transform of the pattern in Figure 3.5. As indicated by the labels on the right-hand side of the figure, ten distinct bands (two from each order of the gratings) are recovered in the transform. These bands are rotated with respect to the  $f_u$  axis. As a result of the grating blaze efficiency shown in Figure 3.4, the ends of a particular order must have the same  $f_v$  position as the center of an adjacent order. If adjacent orders are to be separated by two fringes in the  $v$  dimension, then each order must have a differential of two fringes from the center of the order to its ends. Note the symmetry in Figure 3.6 about the point  $(f_u, f_v) = (0,0)$ .

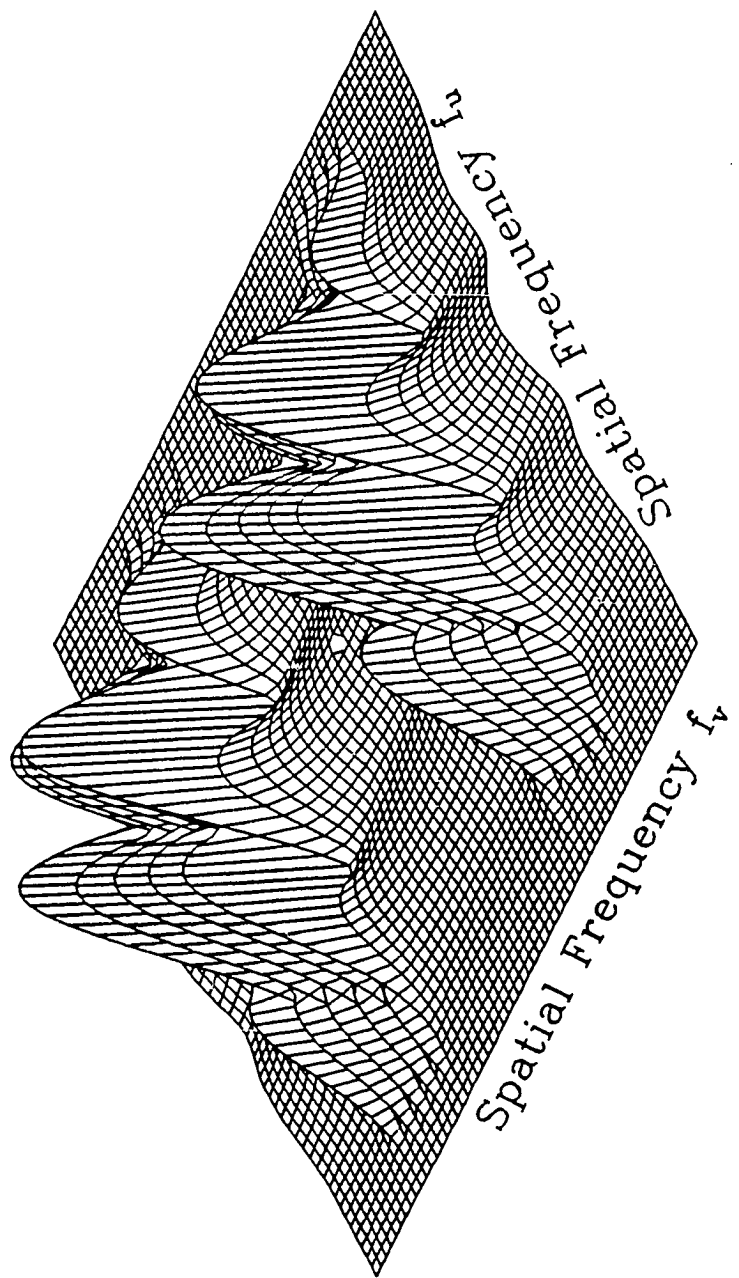
Figure 3.7 shows a perspective representation of Figure 3.6. The intensity recovered along a particular order seems to fluctuate in Figure 3.7 more than expected from the blaze efficiency considerations. The fluctuation is a result of  $f_v$  changing along an order. When  $f_v$  is not an integer, the recovered intensity is shared between pixels in the  $f_v$  dimension; this sharing of intensity is the cause of the extra minima in Figure 3.7.

---

**Figure 3.7** Perspective plot of Figure 3.6: The valleys along a recovered order occur at non-integer values of  $f_v$ , where the intensity is shared between pixels.

---

Figure 3.7: SHS Echelle Simulation



**3.7 Fringe Localization:** With the introduction of the cross-tilt, the Fizeau fringe pattern for a monochromatic point source is a function of  $x$ ,  $y$ , and  $z$ . Following the analysis in section 2.5, the phase of the modulation term in the interferogram can be written as

$$\delta = (k_{x1} - k_{x2})x + (k_{y1} - k_{y2})y + (k_{z1} - k_{z2})z. \quad (3.10)$$

The localization plane can be determined by finding a point  $(x_0, y_0, z_0)$  where  $\delta = 0$  independent of wavenumber and off axis angle. The result is trivial;  $\delta = 0$  at the point  $(x_0, y_0, z_0) = (0, 0, 0)$ . The fringes are localized in the plane  $z = 0$  which coincides with the image of the crossing point of the gratings.

**3.8 Etendue Considerations:** The introduction of a cross-tilt into the system modifies the analysis for the response of the system to off-axis input angles. In principle, the cross-tilt will have an effect on the maximum allowable input aperture for a particular resolving power and on the instrumental profile of the system.

The response of the echelle configuration to off-axis wavenumbers can be derived quantitatively by modifying the analysis in Chapter 2 to include the tilt  $\alpha/2$ . When the effect of the cross-tilt is included in the angular expansions, the exiting wavefronts are characterized by wavevectors with components

$$\begin{aligned}
 k_{x1} &= 2\pi(2\sigma'\tan\theta - \sigma\beta - \sigma(\phi^2 + \beta^2)\tan\theta) \\
 k_{x2} &= 2\pi(-2\sigma'\tan\theta - \sigma\beta + \sigma((\phi + \alpha/2)^2 + \beta^2)\tan\theta) \\
 k_{y1} &= -2\pi\sigma\phi \\
 k_{y2} &= -2\pi\sigma(\phi + \alpha).
 \end{aligned} \tag{3.11}$$

As before, the expansion is valid to second order in angles and first order in  $\sigma'/\sigma$  (cf. equation 2.17). The modulation term in the interferogram can then be written

$$\cos\left(2\pi\left[u\left(\sigma' - \sigma\frac{\Omega'}{2\pi}\right) + v\sigma\right]\right) \tag{3.12}$$

where  $\Omega' = \pi(\phi^2 + (\phi + \alpha/2)^2 + 2\beta^2)/2$  (cf. equation 2.18). As long as  $\Omega' \leq \Omega_m$  where  $\Omega_m = 2\pi/R$  is the solid angle field of view, determined by the analysis in Chapter 2, the spatial frequency shifts due to off axis-angles in the echelle system will be tolerable and the instrumental profile in the presence of the cross-tilt will differ only slightly from the profile in the absence of the tilt.

The maximum field of view for most practical SHS echelle systems differs only slightly from the field of view for a basic SHS system operating at the same resolution. This is because the angle  $\alpha/2$  is typically much

smaller than the maximum  $\phi$  achieved by the basic system ( $\phi_m - \sqrt{2/R}$  derived in section 2.6). For example, if an SHS echelle system is to be designed with the maximum order number of  $m_{max} = 50$ , a resolving power of 20,000 at  $\sigma = 20,000 \text{ cm}^{-1}$ , and a grating of 5 cm aperture, then  $\alpha/2 \approx 0.05\phi_m$ . In this case,  $\Omega'$  differs very slightly from  $\Omega$  ( $\Omega = \pi(\beta^2 + \phi^2)$ ) and therefore,  $\Omega'_m \approx \Omega_m$ .

#### 4. All-Reflection Configurations

**4.1 Introduction:** Interference spectrometers are typically limited to spectral regions where transmitting optical elements are available. In the extreme ultraviolet (EUV) and x-ray spectral regions ( $\lambda < 1100\text{\AA}$ ), transmitting optical materials are not available or of sufficient quality for interferometry. In an effort to bring the gains of interference spectroscopy to the EUV and x-ray regions, all-reflection FTS systems have been designed and tested (Kruger et al., 1972; Fonck et al., 1978); however, the scan and control mechanisms required by these devices tend to be complex and costly.

The SHS systems discussed thus far all require at least one transmitting optical element. All-reflection SHS configurations not requiring transmitting elements that also retain the simplicity and robust qualities of other SHS systems will be discussed in this chapter. The all-reflection configurations use a symmetrically ruled diffraction grating as the beam splitter/combiner and as a dispersive element in the system. The discussion is limited to the one dimensional format of Chapter 2. However, except where indicated, the two dimensional techniques addressed in chapter 3 are applicable to the all-reflection systems. Properties of the simplest design will be derived, particularly when they differ from the properties derived for the basic SHS

configuration. Other designs will then be introduced.

**4.2 The Simple All-Reflection System:** The simplest all-reflection configuration is shown schematically in figure 4.1. Light enters the lower portion of the elliptical aperture  $S$ , is collimated by mirror  $M_3$ , and divided by beam-splitting grating  $G_0$  which may be holographically produced to provide symmetric splitting. Mirrors  $M_1$  and  $M_2$ , located symmetrically on either side of the grating, return the diffracted light to the grating where the beams are recombined. The exiting beam is focused by mirror  $M_3$  through the exit portion of the aperture and onto the imaging detector. The diffraction grating acts both as the beam splitter and the dispersive element in the system. In order to derive the complete Fizeau fringe pattern and the interferogram produced by this device, the phase of the wavefronts diffracted from the grating must be examined.

**4.3 Phase Discontinuity Upon Diffraction:** In the development of the properties of the basic SHS configuration, the phase of a wavevector upon diffraction was considered to be a continuation of the incident phase. This was possible because the wavevectors characterizing the wavefronts under consideration intersected the origin shown in figures 2.1 and 2.2, which was positioned at the point where the gratings cross at the center of a groove facet. Phase shifts introduced upon diffraction are the same for both beams

**Figure 4.1** Schematic diagram of the all-reflection SHS configuration:  
Light enters the system through the lower half of split aperture S and exits  
through the upper half. The diffraction grating acts as both the beam splitter  
and dispersive element in the system.

---

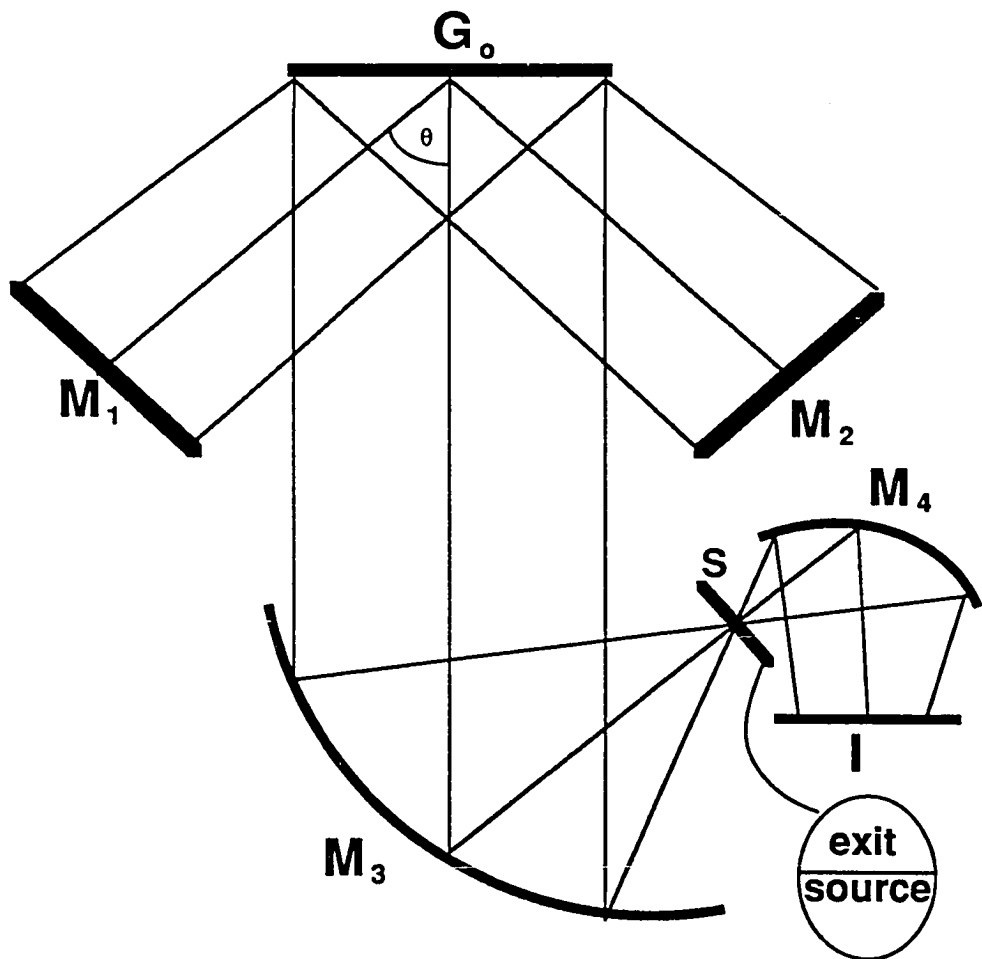


**Figure 4.1**

and do not effect the phase of the Fizeau fringes. In this analysis, the phase can be considered to be continuous only through one point on the grating. For rays incident on other points on the grating, the phase suffers a discontinuity. The discontinuity is illustrated in figure 4.2 where a plane wavefront of wavenumber  $\sigma$  is incident on a transmission grating of groove density  $1/a$  at angle  $\theta_1$  and diffracted to order  $m$  at an angle  $\theta_2$  given by the grating equation  $\sigma(\sin\theta_1 + \sin\theta_2) = m/a$ . The phase of the ray passing through point P on the figure is assumed continuous. Figure 4.3 illustrates a ray passing through point P' where the phase undergoes a discontinuity. The path difference associated with the discontinuity is found by determining the equivalent path through point P shown by the dark line in Figure 4.3. The path is given by  $l_g - x(\sin\theta_1 + \sin\theta_2)$  which, with the help of the grating equation, can be written as

$$l_g - \frac{x}{\sigma} \frac{m}{a}. \quad (4.1)$$

The sign of  $x$  is determined as follows:  $x$  is positive (negative) if the exiting ray at P is diffracted toward (away from) P' with reference to the zero order ray. This general result holds where the incident and exiting rays have non-zero components out of the dispersion plane of the grating ( $\phi \neq 0$ ). In this

**Figure 4.2** Illustration of the phase relationship between incident and diffracted wavefronts: The phase is continuous through point P on the diffraction grating.

---

---

**Figure 4.3** Geometry for determining the phase discontinuity upon diffraction: If the phase of the ray through point P is assumed continuous, the discontinuity in phase which occurs at point P' is given by the equivalent path through point P. The equivalent path is illustrated as the dark line and is given by  $l_g - x(\sin\theta_1 + \sin\theta_2)$ .

---

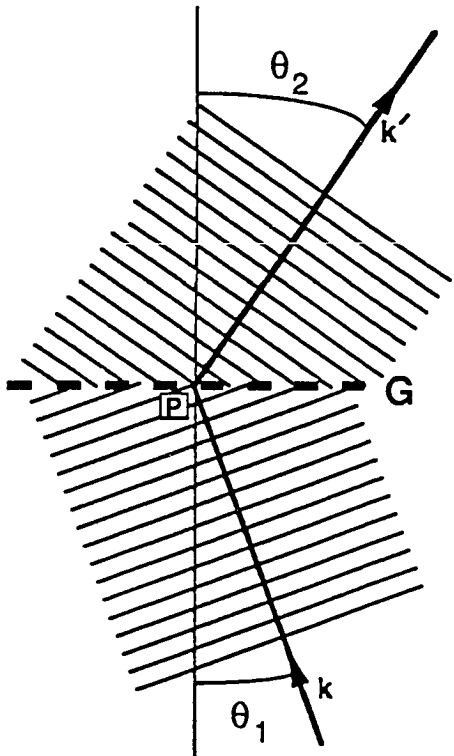
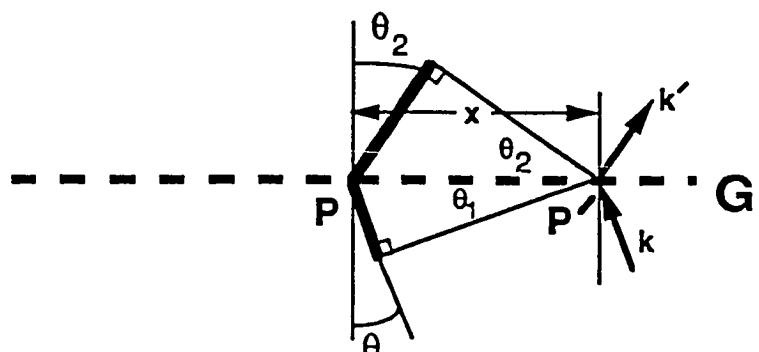


**Figure 4.2**



$$l_g = x (\sin \theta_1 + \sin \theta_2)$$

**Figure 4.3**

case,  $x$  is the distance between points  $P$  and  $P'$  projected onto the dispersion plane.

**4.4 Ray Tracing Analysis:** To derive the properties of the Fizeau fringe pattern produced by the all-reflection interferometer it was necessary to extend the general framework developed in section 2.2 to include the phase shifts introduced by the grating beam splitter. Similar to the earlier analysis, wavefronts were characterized by their wavevectors. The phase of the waves at the exit of the interferometer was obtained by tracing the rays associated with the wavevectors, starting from the beamsplit, through both arms of the interferometer, and then back to the diffraction grating where discontinuities in path upon diffraction were included.

Figure 4.4 shows an optical equivalent of the interferometer portion of figure 4.1. The images of the grating in the two side mirrors are shown as gratings  $G_1$  and  $G_2$ . In addition, the two images of the grating and the grating itself are shown as transmission gratings for clarity. Gratings  $G_1$  and  $G_2$  represent the grating at the beam split and  $G$  represents the grating when the beams are recombined. Distance  $d$  designates the on-axis separation between the gratings in each arm. Also shown in the figure are the central rays associated with wavefronts which produce zero spatial frequency at the output. The wavenumber of these rays is  $\sigma_0$  (by definition) and for the

**Figure 4.4** Optical equivalent of the simple all-reflection SHS system shown in Figure 4.1: The interferometric portion of the system is unfolded for clarity. A ray of wavenumber  $\sigma_0$  and incident angles  $\beta = 0$  and  $\phi = 0$  defines the optical axis of the system.

---

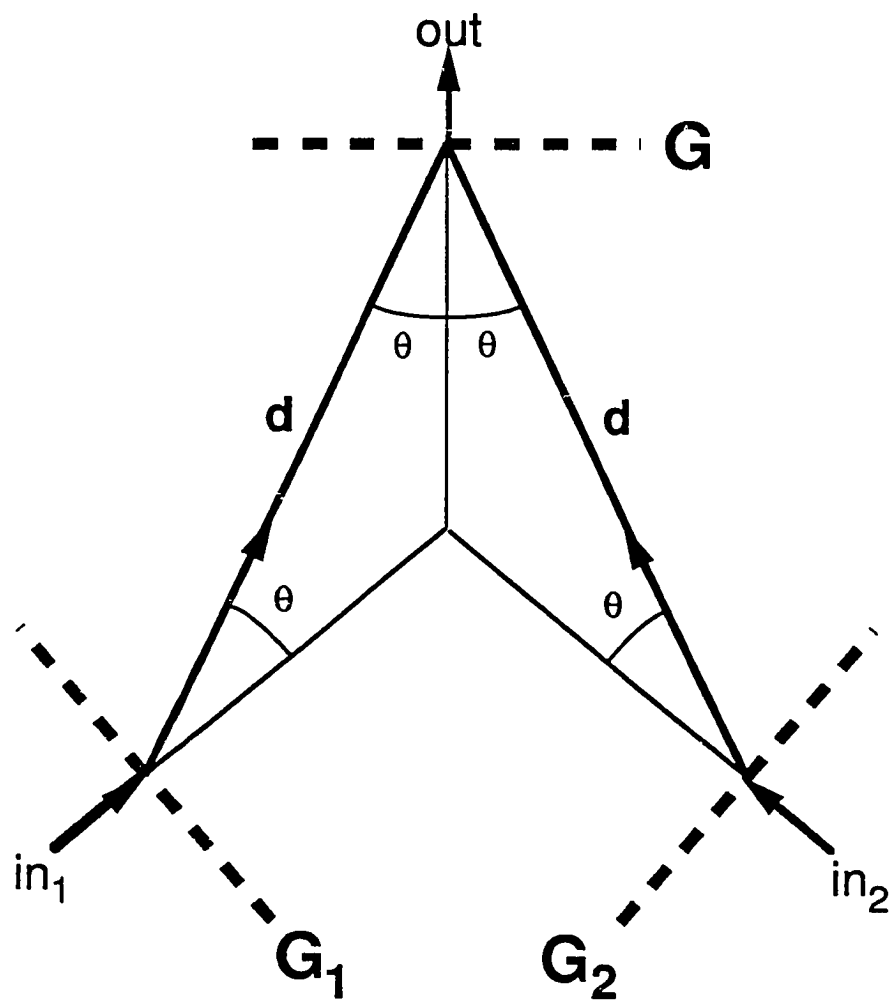


**Figure 4.4**

particular rays shown in the figure,  $\beta=0$  and  $\phi=0$ . Coordinates for describing off-axis wavevectors of arbitrary wavenumber and input angle are illustrated in figure 4.5. Keeping in mind that points  $O$ ,  $O_1$ , and  $O_2$  in the figure all represent the same physical point on the diffraction grating, a wavevector incident on points  $O_{1,2}$  at angles  $\beta$  and  $\phi$  is diffracted to two wavevectors at angles  $\theta + \beta'_{1,2}$  and  $\phi$ . These rays travel a distance  $l_{1,2}$  to points  $P_{1,2}$  which are a distance  $\vec{r}_{1,2}$  away from  $O$ . The rays suffer a discontinuity in path of  $l_{g1,g2}$  at points  $P_{1,2}$  and are diffracted again into angles  $\beta_{1,2}$  and  $\phi$ . The interference of the two exit wave fronts can be written as

$$\begin{aligned} I = & I_0(1 + \cos(\delta)) \\ \delta = & \vec{k}_1 \cdot (\vec{r} - \vec{r}_1) + k(l_1 + l_{g1}) - \\ & (\vec{k}_2 \cdot (\vec{r} - \vec{r}_2) + k(l_2 + l_{g2})) \end{aligned} \quad (4.2)$$

where  $\vec{k}_i$  is defined in equation 2.3,  $k=2\pi/\sigma$ , and  $\vec{r}=ix+jy+kz$  is a vector between  $O$  and the observation point. The output angles in figure 4.5 are determined by two applications of the grating equation as

---

**Figure 4.5** Illustration showing the central rays for off-axis wavefronts of arbitrary wavenumber: The wavevectors  $\mathbf{in}_1$  and  $\mathbf{in}_2$  represent the same ray incident on the beam splitter.

---

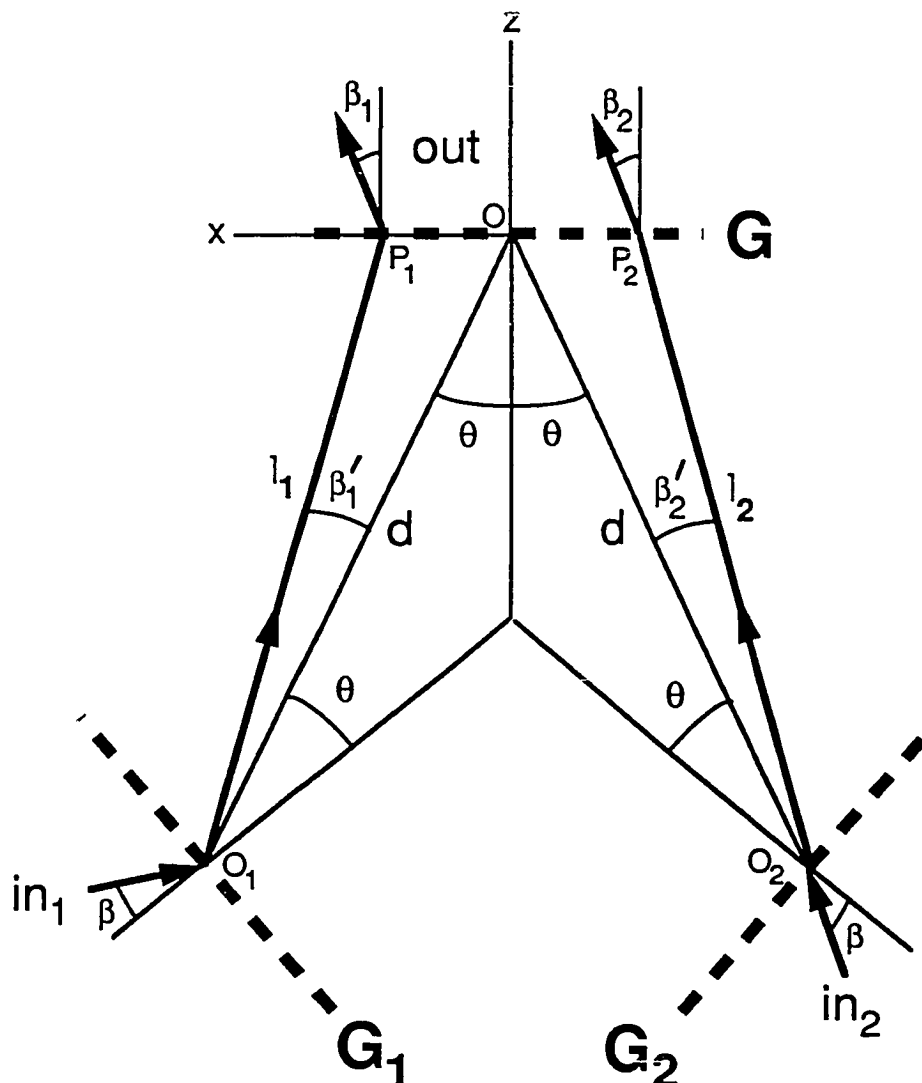


**Figure 4.5**

$$\begin{aligned}
 \sin(\theta + \beta'_{1,2}) &= \frac{\sigma_0 \sin \theta}{\sigma \cos \phi} \mp \sin \beta \\
 \sin \beta_{1,2} &= \pm \frac{\sigma_0 \sin \theta}{\sigma \cos \phi} \mp \sin(\theta - \beta'_{1,2}) \\
 \phi_{1,2} &= \phi
 \end{aligned} \tag{4.3}$$

where  $\sigma_0 \sin \theta = m/a$ . Figure 4.5 and simple geometry give the distances required by equation 4.2:

$$\begin{aligned}
 l_{1,2} &= \frac{d \cos \theta}{\cos \phi \cos(\theta - \beta'_{1,2})} \\
 x_{1,2} &= \pm \frac{d \sin \beta'_{1,2}}{\cos(\theta - \beta'_{1,2})} \\
 y_{1,2} &= \frac{d \cos \theta \tan \phi}{\cos(\theta - \beta'_{1,2})} \\
 z_{1,2} &= 0 \\
 l_{g1,g2} &= \frac{d \sin \beta'_{1,2}}{\cos(\theta - \beta'_{1,2})} \frac{\sigma_0}{\sigma} \sin \theta.
 \end{aligned} \tag{4.4}$$

With the system characterized in this manner, its properties can now be determined.

**4.5 First Order Axial Analysis:** For a monochromatic point source on axis in the input aperture in figure 4.1, the Fizeau fringe pattern produced at the output follows directly from equations 4.2, 4.3, and 4.4. Setting  $\beta = 0$  and  $\phi = 0$  in equation 4.3 and expanding to first order in  $\beta'$  and  $\beta$ , gives

$$\begin{aligned}\beta'_{1,2} &= -\frac{\sigma - \sigma_0}{\sigma} \tan\theta \\ \beta_{1,2} &= \mp 2 \frac{\sigma - \sigma_0}{\sigma} \sin\theta.\end{aligned}\tag{4.5}$$

The intensity recorded on the detector is described by a first order expansion of equation 4.2

$$I(x) = I_0(1 + \cos(2\pi 4(\sigma - \sigma_0)x \sin\theta)).\tag{4.6}$$

Making the substitutions  $\sigma' = \sigma - \sigma_0$  and  $u = 4x \sin\theta$  and generalizing to the polychromatic case, the familiar form

$$I(u) = \int_{-\infty}^{\infty} B_e(\sigma') d\sigma' (1 + \cos(2\pi \sigma' u))\tag{4.7}$$

is recovered. Note that the path difference  $u$  for this system differs from the path difference in the Michelson configuration by a factor of  $1/\cos\theta$ .

The resolution limit for SHS systems was derived in section 2.4 as  $\delta \sigma' = 1/2 u_{\max}$ . Setting  $u_{\max} = 2W\sin\theta$  where  $W$  is the width of the grating in the dispersion plane, the expression for the theoretical resolving power for this system is the same as derived for the basic SHS system in Chapter 2:

$$R_0 = 4W\sigma \sin\theta. \quad (4.8)$$

**4.6 Fringe Localization Plane:** The localization of the Fizeau fringes for the all-reflection interferometer can also be derived using the framework of section 4.4. As described in detail in section 2.5, if a point  $(x_0, y_0, z_0)$  can be found where  $\delta = 0$  independent of incident angle or wavenumber, then the fringes are localized in the plane  $z = z_0$ . Setting  $x_0 = 0$  and  $y_0 = 0$  in equation 4.2, this condition can be expressed as

$$0 = -\vec{k}_1 \cdot \vec{r}_1 + \vec{k}_2 \cdot \vec{r}_2 + k_{z1}z_0 - k_{z2}z_0 + k(l_1 - l_2 + l_{g1} - l_{g2}). \quad (4.9)$$

Using equations 4.3 and 4.4 and much algebra, equation 4.9 can be written

$$0 = k \cos\phi [z_0(\cos\beta_1 - \cos\beta_2) + d(\cos\beta'_1 - \cos\beta'_2)]. \quad (4.10)$$

Expanding equation 4.10 to second order in angles and substituting  $\beta'_i$  and  $\beta_i$  derived from a power expansion of equation 4.3 gives

$$0 - z_0 \left( -\frac{8\sigma'}{\sigma} \beta \sin\theta + O^3 \right) + \\ d \left( -\frac{4\sigma'}{\sigma} \beta \frac{\sin\theta}{\cos^2\theta} + O^3 \right) \quad (4.11)$$

where  $O^3$  indicates terms in the expansion higher than second order in  $\beta$ ,  $\phi$ , and  $\sigma'/\sigma$ . Equation 4.11 is satisfied to second order in  $\sigma'/\sigma$  and off axis angle by the relationship

$$z_0 = -\frac{d}{2\cos^2\theta}. \quad (4.12)$$

The plane  $z - z_0$  is the fringe localization plane. In the following analysis, the coordinate system describing the Fizeau fringes will be translated in the  $z$  direction by an amount  $z_0$  from the position indicated in Figure 4.5 so the origin of the coordinate system coincides with the zero phase point of the Fourier transform and  $\delta \sim (\vec{k}_1 - \vec{k}_2) \cdot \vec{r}$  in equation 4.2.

#### 4.7 Off Axis Analysis:

With the localization plane defined and the

origin of the coordinate system describing the fringes shifted to the localization plane, the response of the all-reflection system to off-axis wavefronts can be determined. The basic procedure, described in section 2.6, requires an expansion of equation 4.3 to second order in  $\beta$  and  $\phi$  and first order in  $\sigma'/\sigma$ , and substitution of the results into equation 4.2. The fringe frequency shift for off-axis wavefronts and the magnitude of this shift ultimately limits the field of view. If the system views a solid angle  $d\Omega$ , then the intensity recorded on the detector is

$$dI(u) = \int_{-\infty}^{\infty} B_e(\sigma') d\sigma' (1 + \cos[2\pi u(\sigma' - \sigma(\phi^2 + \frac{\beta^2}{\cos^2 \theta}))]) d\Omega. \quad (4.13)$$

This relationship differs from equation 2.18 by the factor of  $1/\cos^2 \theta$  in the  $\beta^2$  term. The effect of this term is to reduce the field of view in the dispersion plane relative to the field of view in the basic SHS configuration by a factor of  $\cos \theta$ . Using the criterion of section 2.6 to determine the maximum field of view, the field of view for the all-reflection system is

elliptical with half angles

$$\begin{aligned}\phi_m &= \sqrt{2/R} \\ \beta_m &= \sqrt{2/R} \cos \theta\end{aligned}\quad (4.14)$$

in the y-z and x-z planes, respectively.

**4.8 Reduced Resolving Power System:** For a given wavenumber, the grating angle,  $\theta$  and the width of the grating,  $W$  determine the resolving power of the simple all-reflection system ( $R = 4W\sigma \sin\theta$ ). For a fixed resolving power and maximum throughput (which is proportional to  $W$ )  $\theta$  must be small. A practical limit is reached in the simple all-reflection system when  $\theta$  is decreased because the instrument must be lengthened to provide clearance between the return mirrors for the incident and exiting light. The overall size of the instrument can become large, especially at low resolving power. The size limitation can be overcome by replacing the return mirrors in Figure 4.1 with matched diffraction gratings used in Littrow as shown in Figure 4.6. The beam splitting grating can then be used at a relatively large angle because the path difference introduced by the beam splitting grating is in part canceled by the path difference introduced by the side gratings. If  $\theta'$  is the Littrow angle of the side gratings, the path difference in this

**Figure 4.6** Reduced resolving power all-reflection SHS configuration:  
Littrow gratings  $G_1$  and  $G_2$  cancel some of the path difference introduced by  
grating  $G_0$ . For a fixed resolving power, the angle  $\theta$  is independent of the  
width of the gratings.

---

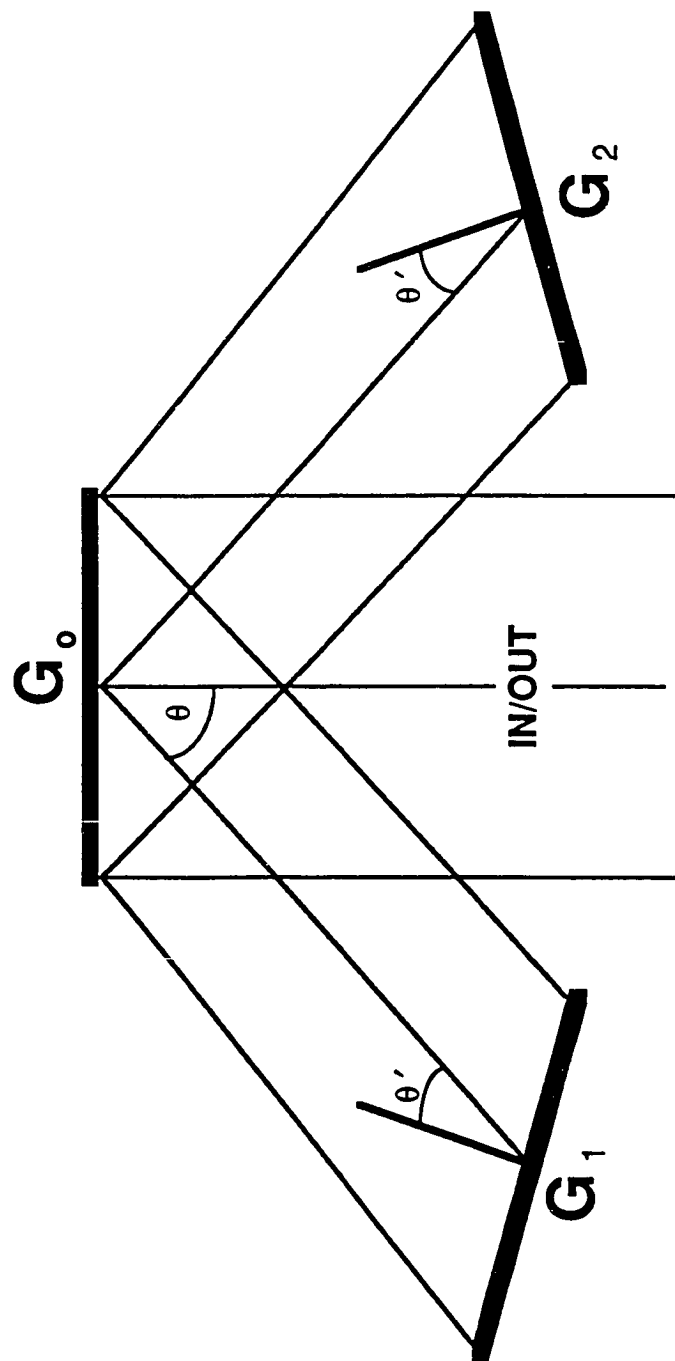


Figure 4.6

configuration is given by

$$u = 4x \sin \theta (1 - \tan \theta' \cot \theta) \quad (4.15)$$

which leads to a resolving power of

$$R_0 = 4W\sigma \sin \theta (1 - \tan \theta' \cot \theta). \quad (4.16)$$

A detailed analysis of this configuration shows the fringe localization plane and the restrictions on the input aperture are the same as those for the simple all-reflection system (eqs. 4.12 and 4.14).

**4.9 Common Path Configurations:** Figure 4.7 shows a common path arrangement of the all-reflection interferometer. The system is identical to the simple all-reflection interferometer shown in Figure 4.1 except the side mirrors are rotated so the two beams circulate in opposite directions through the interferometer. From an optical standpoint this configuration unfolds to the schematic interferometer illustrated in figure 4.5. As a result, the analysis provided for the simple all-reflection interferometer applies directly to this device. An advantage of the common path arrangement is that the spatial frequency of the fringe pattern is insensitive to pure translations of the side mirrors since each beam is incident on every optical element in the system. The result is a system that is much more forgiving with regard to its alignment and stability requirements. Rotations of the side mirrors tune the system in the wavenumber associated with zero spatial frequency  $\sigma_0$ . A disadvantage

---

**Figure 4.7** Common path arrangement of the simple all-reflection interferometer: Mirrors  $M_1$  and  $M_2$  are rotated so the beams of light circulate through the system in opposite directions.

---

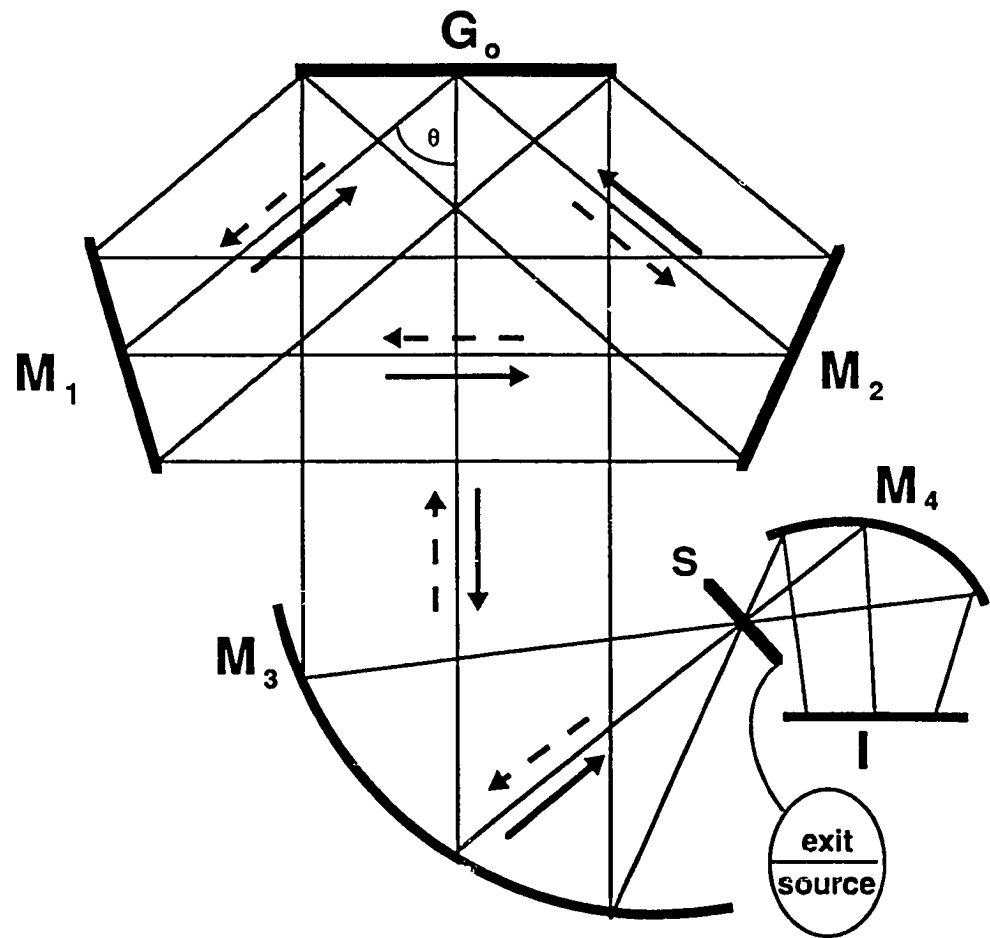


**Figure 4.7**

of the common path configuration is that the two dimensional geometry of Chapter 3 is not possible since a tilt in one of the side mirrors effects both beams in the same sense.

Another feature of the common path interferometer is that an incident ray that is split on the left half of the diffraction grating recombines and exits via the right half of the diffraction grating. This suggests the alternate input and output optical configuration shown in Figure 4.8. Light is collimated by mirror  $M_1$  (which could be a mechanical collimator) and passed to the left half of the diffraction grating. The beams are combined on the left half of the diffraction grating and focused onto the detector by mirror  $M_4$ . Only one side of the symmetric interferogram is recorded and vignetting effects reduce the efficiency near the point  $x=0$ . The advantage of this configuration is the ease and efficiency of the input and output optics, especially when a mechanical collimator is used. The two dimensional format can be utilized since the beams circulate through the system next to one another; one of the side mirrors may be split and tilted slightly to produce fringes in the cross direction.

**4.10 Zero Order Reflections:** A disadvantage of the split input/output aperture in the above all-reflection configurations is scattered and background unmodulated light can find its way to the detector and ultimately add to the

---

**Figure 4.8** Common path all-reflection SHS system with alternative input/output: Half of the grating is used as a beam splitter and the other half as a beam combiner. As a result, the system records only one side of the symmetric interferogram.

---

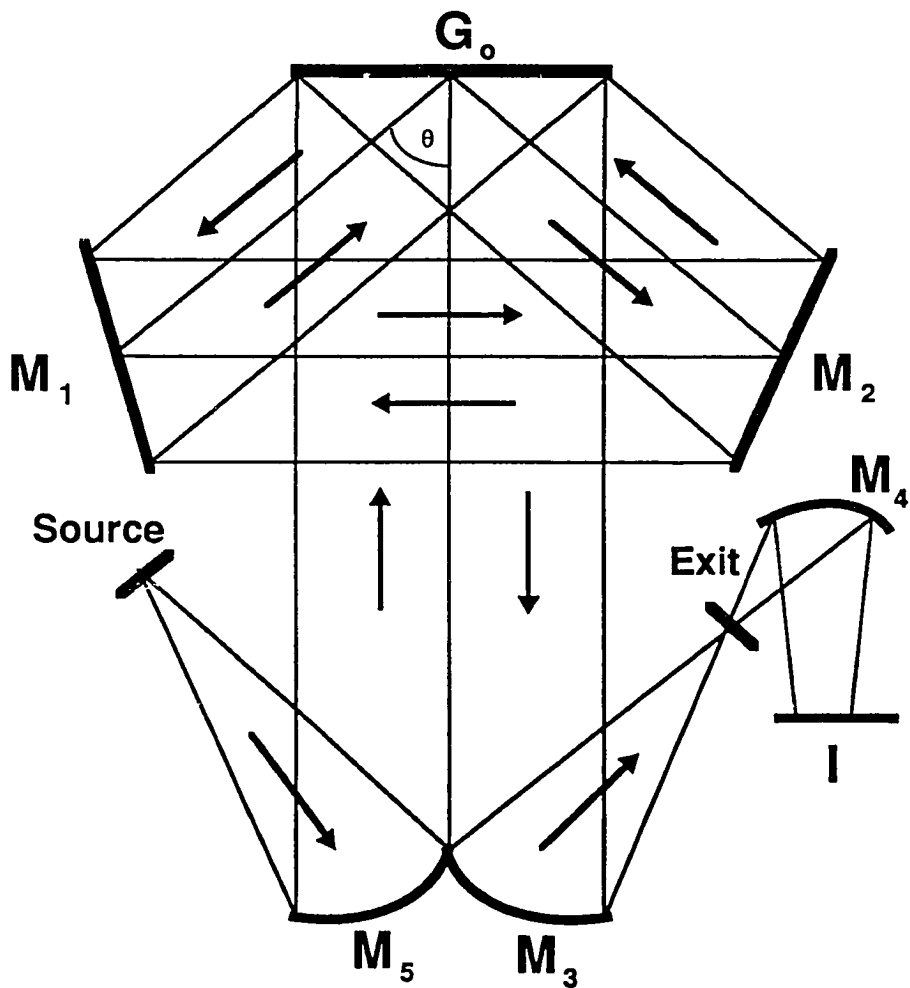


**Figure 4.8**

noise in the recovered spectrum. Most of the problem comes from input light returning directly from the diffraction grating in zero order through the exit portion of the aperture and onto the detector. By tipping the diffraction grating, the zero order light can be separated from the modulated light and blocked before it reaches the detector (Fonck & Roesler, 1980), however, this comes at the cost of reducing the field of view. In the configuration shown in Figure 4.9 the split aperture is eliminated by replacing the side mirrors with roof mirrors to redirect the returning beams underneath the point where the beams are split. Separate collimating and focusing mirrors are used so the exit aperture can be located away from the entrance aperture. The price paid is the addition of one reflection in each of the beams. This concept can also be adapted to the common path interferometer by replacing one of the side mirrors with a roof mirror (Figure 4.10). A two-sided interferogram is recorded in this common path configuration in contrast to the one-sided interferogram obtained with the configuration in Figure 4.8.

---

**Figure 4.9** Alternate arrangement of the simple all-reflection interferometer which eliminates a split aperture: Roof mirrors  $RM_1$  and  $RM_2$  direct the return beams below (into the plane of the figure) the outgoing beams. By using separate collimating and focusing mirrors, the exit aperture may be located away from the entrance aperture.

---

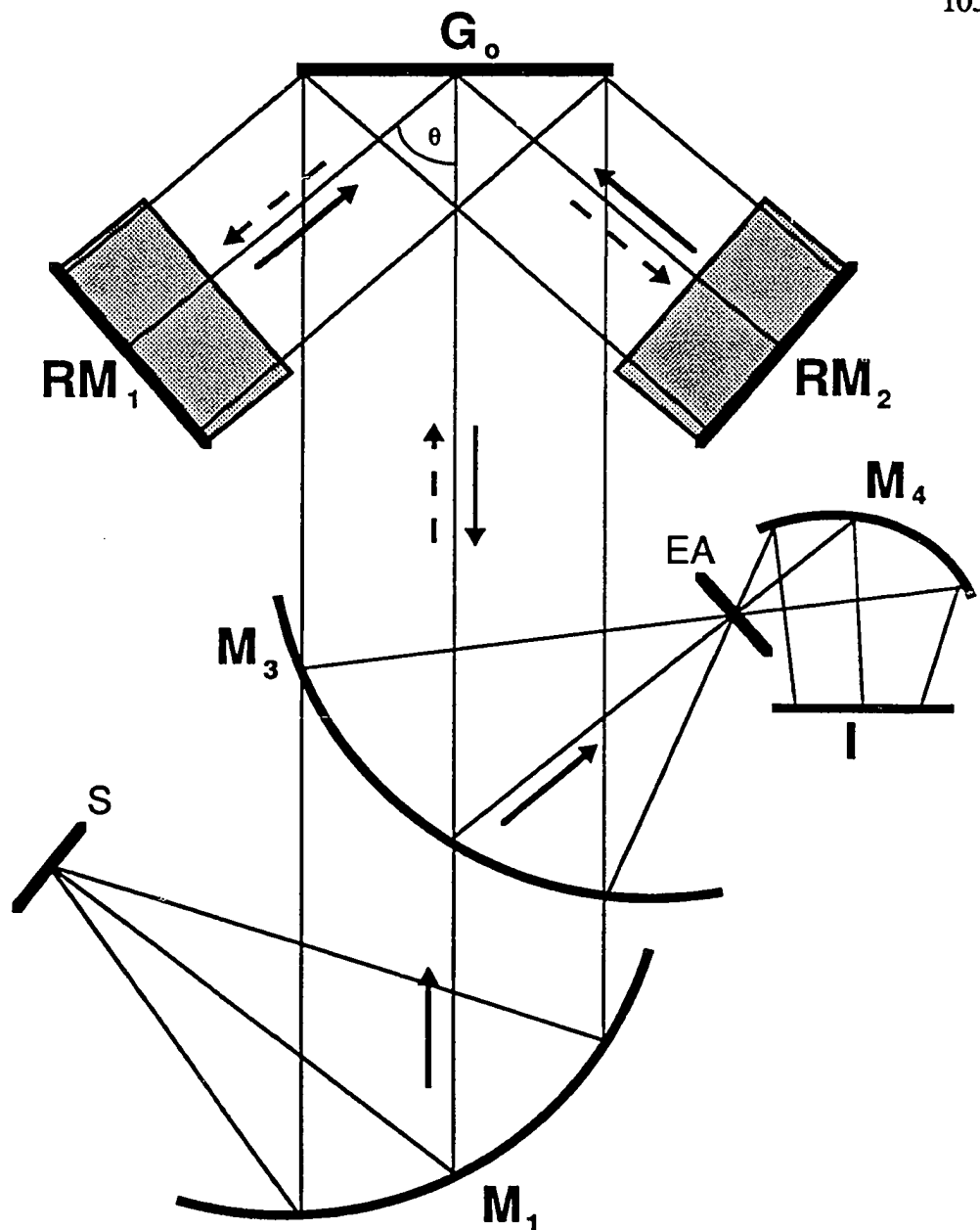


**Figure 4.9**

---

**Figure 4.10** Common path all-reflection interferometer with separated input/output: Adaptation of the concept in Figure 4.9 to the common path system.

---

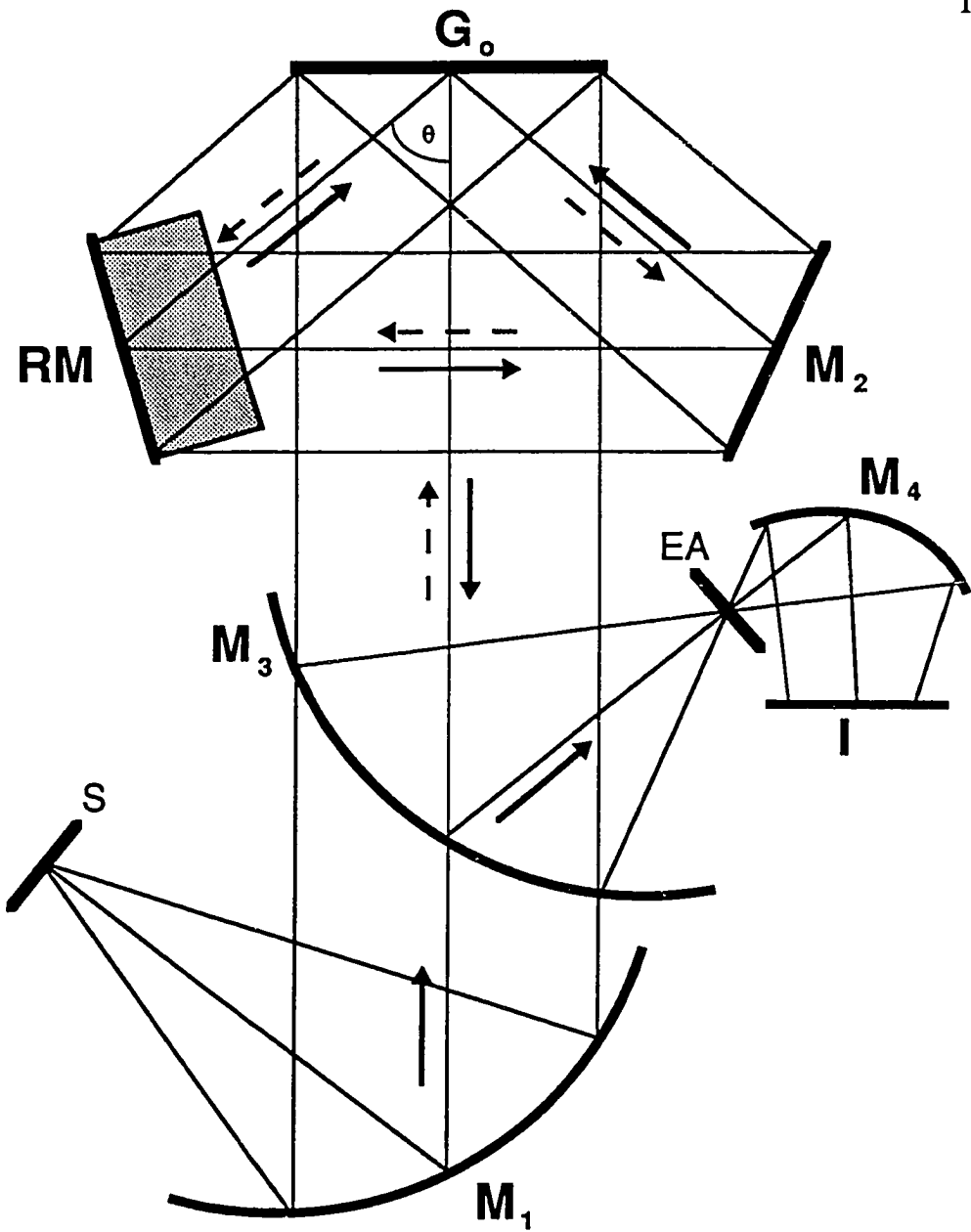


**Figure 4.10**

## 5. Field Widened Systems

**5.1 Introduction:** Chapter 2 demonstrated that the field of view of the basic SHS system is equal to the field of view achieved by Fabry-Perot and conventional FTS interferometers. For spatially extended sources, interferometric spectrometers are much more sensitive than comparable grating spectrometers because they achieve a field of view that is typically two orders of magnitude greater than achieved by grating spectrometers. In an effort to further increase these field of view gains, field widening techniques have been developed for FTS systems (Baker, 1977). Field widened FTS (FW-FTS) systems achieve a field of view  $\Omega_m$  approximately two orders of magnitude greater than that of standard FTS, giving them a gain of four orders of magnitude over diffraction grating systems. The increase in field of view can be used either to increase the sensitivity of the instrument or to decrease its overall size and cost. Field widening techniques can also be applied to SHS systems. The advantage of field widened SHS (FW-SHS) systems over FW-FTS systems is FW-SHS retains most of the characteristics of basic SHS systems (i.e. no moving parts) while achieving a field of view characteristic of FW-FTS systems.

Chapter 5 briefly reviews properties of field widened FTS systems and then introduces field widened SHS systems. The chapter concludes with a discussion of a speculative method for field widening the all-reflection SHS configuration.

**5.2 Field Widened FTS Systems:** The limitation on the field of view in interferometric systems results from the change in path difference with off-axis angle. For Fabry-Perot and conventional FTS interferometers, the leading term in the expansion of path difference with respect to off-axis angle is quadratic, a dependence that arises solely from geometrical considerations.

Figure 5.1 illustrates the situation for the Michelson interferometer. The path difference off-axis is related to the axial path difference by  $l' - l \cos \theta \sim l(1 - \theta^2/2)$  where  $l'$  ( $l$ ) is the off-axis (axial) path difference and  $\theta$  is the off-axis angle. The  $\theta^2$  term in this path difference can be eliminated by placing a material with refractive index  $n$  directly in front of the displaced mirror (Mertz, 1965). A field widened FTS system is illustrated in Figure 5.2. For this field widened configuration the leading angular term in path difference is quartic (Bouchareine & Connes, 1963). The thickness  $t$  of the refractive material is given by  $t = nl/2(n - 1)$ ; the *geometric* position of the mirrors coincide when viewed from the exit aperture while, from a *physical* optics point of view, a path difference is retained.

---

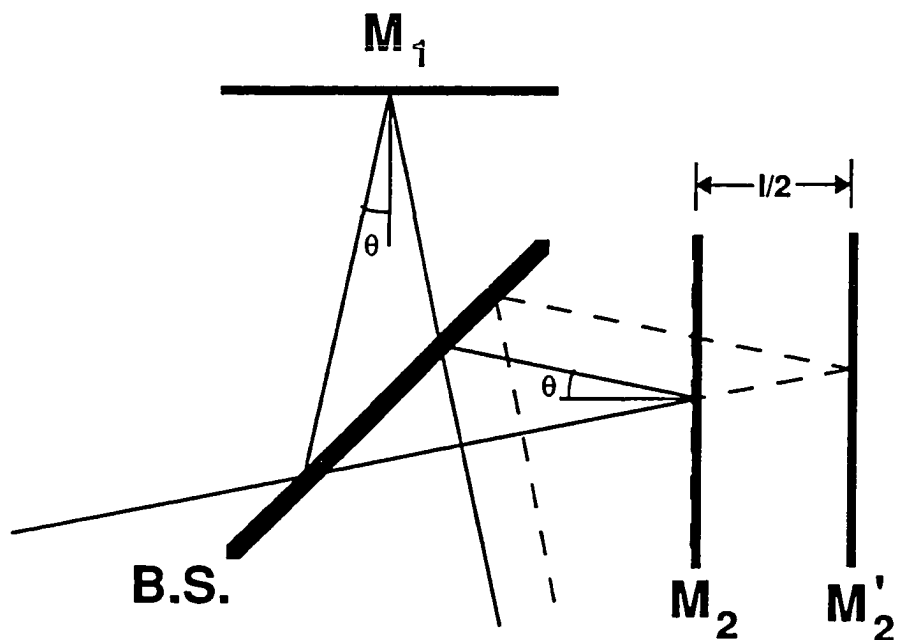
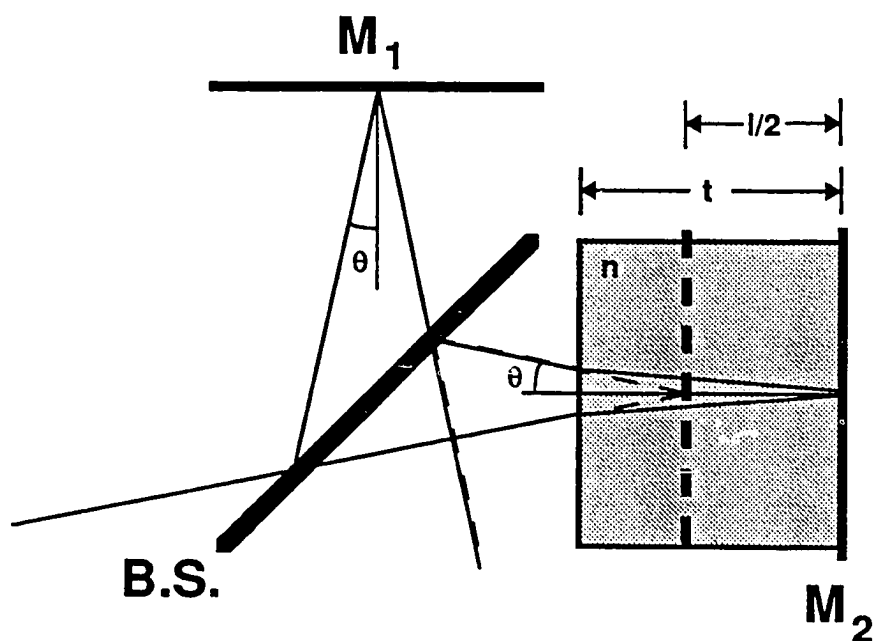
**Figure 5.1** Off-axis properties of a Michelson interferometer: When mirror  $M_2$  is moved to position  $M_2'$ , the path difference in the system becomes a function of off-axis angle  $\theta$ .

---

---

**Figure 5.2** Field widened Michelson interferometer: If a material with refractive index  $n$  and thickness  $t$  is placed in front of the displaced mirror  $M_2'$ , the quadratic dependance on path difference with off-axis angle is eliminated. The thickness of the material is chosen so the geometric images of  $M_1$  and  $M_2$  appear coincident.

---

**Figure 5.1****Figure 5.2**

In order to construct a functioning field widened FTS instrument, the thickness of the refractive material must be varied as the system is scanned, while at the same time achieving interferometric tolerances on the alignment of the scanned elements. Consequently, field widened FTS instruments require complex scan and control mechanisms. Numerous instrumental configurations have been conceived in an effort to minimize the complexity associated with these devices and many field widened FTS interferometers have successfully operated in the field (Baker, 1977).

**5.3 Field Widened SHS Systems:** Field widening techniques can be applied to SHS systems, but in marked contrast to field widened FTS instruments, field widened SHS instruments *have no moving parts*. The simplest field widened SHS system is shown in Figure 5.3 where prisms  $P_1$  and  $P_2$  have been placed in the arms of the basic configuration of the device. The prism angle is selected so the diffraction grating appears to be perpendicular to the optical axis when viewed through the refractive material in the prism. From a geometrical optics standpoint, the diffraction gratings behave as if they were mirrors in a conventional Michelson interferometer at zero path difference. Aberrations introduced by the prisms ultimately limit the field of view, but not before large gains are realized in many situations.

**5.4 Analysis:** Conceptually, the analysis of the field widened SHS

---

**Figure 5.3** Field widened SHS system: Prisms  $P_1$  and  $P_2$  are chosen so the diffraction gratings appear, from a geometrical optics point of view, perpendicular to the optical axis.

---

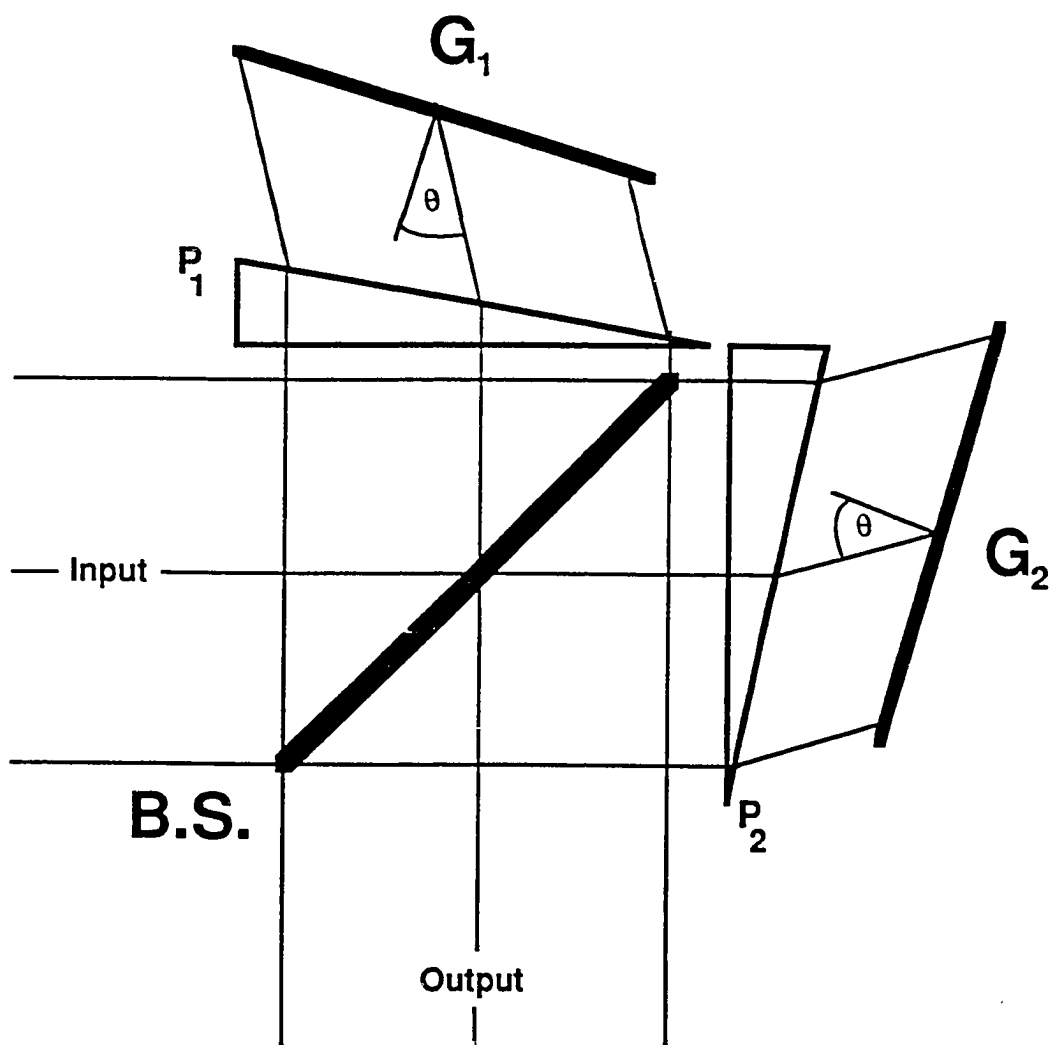


**Figure 5.3**

systems parallels the analysis utilized for the conventional systems. At the input, a wavefront is characterized by a single ray which gives rise to two rays at the output. The wavefronts associated with these coherent output rays interfere to produce Fizeau fringes. The interference pattern is determined by the superposition of Fizeau patterns resulting from all rays admitted into the system. In the general case, ray tracing must be performed on every ray pair to determine the phase of the fringes (cf. Chapter 4). As a practical matter, however, the ray tracing for the system shown in Figure 5.3 is very complex so a simpler procedure was adopted. The spatial frequency of the fringes, the prism angle required to achieve field widened performance, and the maximum field of view for the system are all determined by the direction of the exit vectors  $\vec{k}_1$  and  $\vec{k}_2$ , independent of their phase. The determination of these exit wavevectors is relatively simple and will be performed in Section 5.5.

The calculation of the optical path determines the phase and localization plane of the Fizeau fringe pattern. In general, the calculation is extremely complex and much time (both by hand and using algebraic computer software) has been devoted to perform it, all to no avail. One would expect the fringe localization plane to follow from the analysis in Chapter 2; the fringes are localized at the geometric crossing point of the

gratings (Figures 2.1 and 2.2). This statement has been verified empirically by computer simulation of a number of specific field widened SHS systems. Therefore, in the analysis that follows, the fringe localization plane will be assumed to be at the crossing point of the diffraction gratings and the angles of the exiting wavefronts will be determined independent of their phase.

**5.5 Fringe Frequency:** Figure 5.4 defines the angles that will be used to determine the exit wavefronts. The prisms are assumed to be at minimum deviation and for now, dispersion effects will be ignored since the wavelength range over which the prisms are used is typically small. For a ray incident at angles  $\beta$ , measured in the plane of the figure away from the optical axis, and  $\phi$ , the out-of-plane angle, the angles  $\beta'$  and  $\phi'$  at the output of the prism are given by Snell's law in the form

$$\begin{aligned} \sin\phi_p &= \frac{1}{n}\sin\phi \\ \sin(\alpha/2 + \beta_p) &= \frac{1}{n}\sin(\gamma + \beta)\frac{\cos\phi}{\cos\phi_p} \\ \sin\phi' &= n\sin\phi_p \\ \sin(\gamma + \beta') &= n\sin(\alpha/2 - \beta_p)\frac{\cos\phi_p}{\cos\phi'} \end{aligned} \quad (5.1)$$

**Figure 5.4** Definition of the angles in equation 5.1: Angles with respect to the optical axis  $\beta$ ,  $\beta_p$ , and  $\beta'$  in the dispersion plane of the grating G are shown. The optical axis traverses the prism at minimum deviation. Angle  $\phi$  (not shown) is between the incident ray and the x-z plane.

---

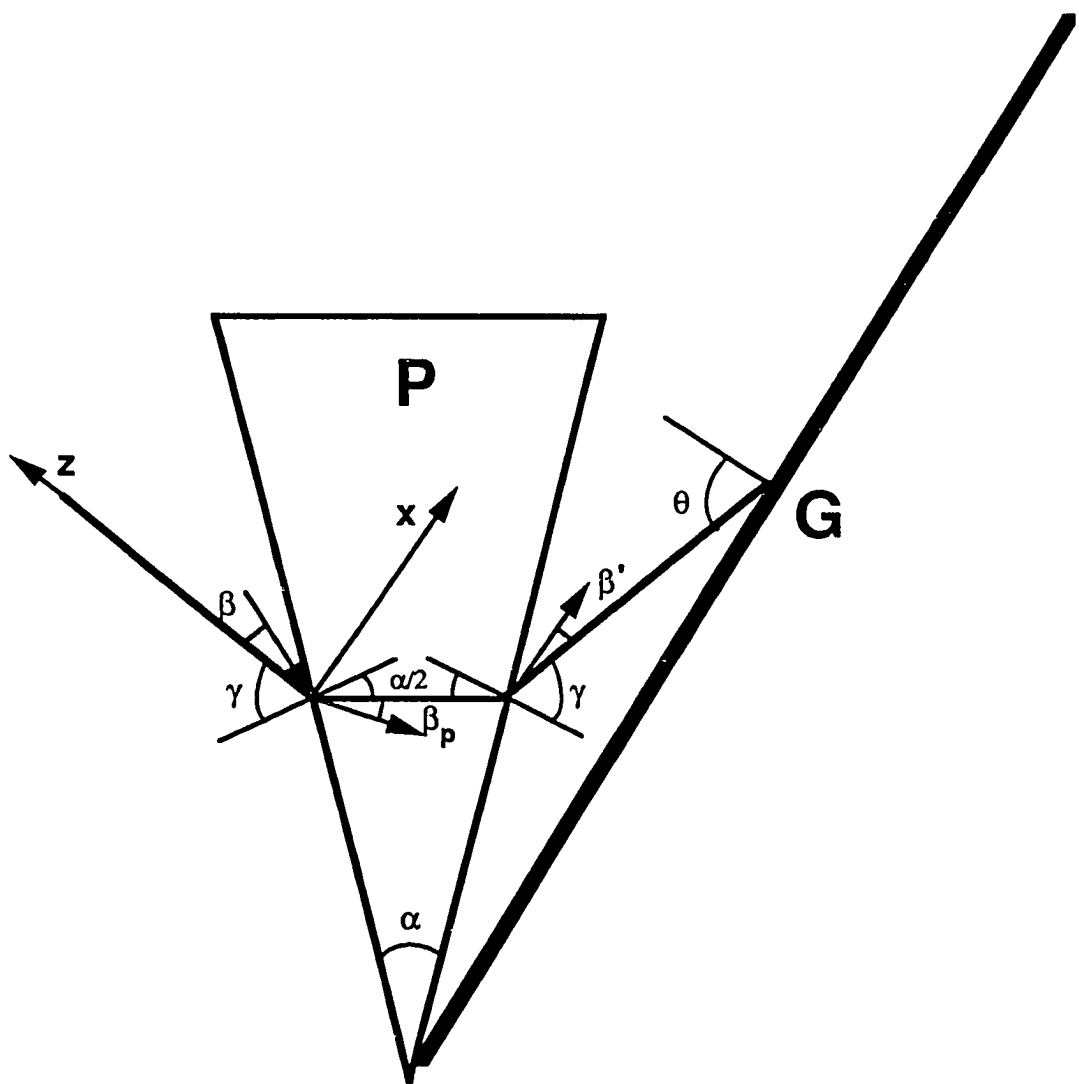


**Figure 5.4**

where  $n$  is the index of refraction of the prism,  $\alpha$  the apex angle of the prism,  $\beta_p$  and  $\phi_p$  are the ray angles in the prism, and  $n \sin(\alpha/2) - \sin\gamma$ . Solving equations 5.1 for  $\beta'$  and  $\phi'$  and expanding to second order in  $\beta$  and  $\phi$  gives

$$\begin{aligned} \phi' - \phi \\ \beta' = -\beta + \beta^2 \frac{\tan\gamma}{\cos^2(\alpha/2)} \left( \frac{n^2 - 1}{n^2} \right) + \phi^2 \tan\gamma \left( \frac{n^2 - 1}{n^2} \right) + \dots . \end{aligned} \quad (5.2)$$

After exiting the prism the ray travels to the diffraction grating. The grating equation (eq. 2.4) and Figures 2.1 and 2.2 describe the diffraction at the grating in terms of the input variables  $\beta$  and  $\phi$ , and the exit variables  $\beta'$  and  $\phi'$ . Solving equation 2.4 for  $\beta'$  and  $\phi'$  and expanding to second order in angles and first order in  $\sigma/\sigma$  gives

$$\begin{aligned} \phi' = -\phi \\ \beta' = 2 \frac{\sigma'}{\sigma} \tan\theta - \beta + \tan\theta (\beta^2 + \phi^2) + \dots . \end{aligned} \quad (5.3)$$

After diffracting from the grating, the ray travels back through the prism and exits the interferometer. The angles between the final ray and the optical axis  $(\beta_{if}, \phi_{if})$  can be determined by first substituting  $(\beta', \phi')$  from

equation 5.2 for  $(\beta, \phi)$  in equation 5.3 and then substituting this result back into equation 5.2 for  $(\beta, \phi)$ . The exit angles  $(\beta_{2f}, \phi_{2f})$  associated with the coherent ray which traversed the opposite arm of the interferometer can be determined, using the above analysis, by making the substitutions  $\beta \rightarrow -\beta$  to determine  $\beta'_{1f}$  and then  $-\beta'_{1f} \rightarrow \beta_{2f}$ . To second order in angles, the phase of the cosine interferogram is  $\delta \sim 2\pi\sigma(\beta_{1f} - \beta_{2f})x$ . With the help of equation 5.2 and 5.3 the phase can be written

$$\begin{aligned}\delta = & 2\pi x [-4\sigma' \tan\theta \\ & + 2\sigma\beta^2 \left( \frac{2(n^2-1)}{n^2} \frac{\tan\gamma}{\cos^2(\alpha/2)} - \tan\theta \right) \\ & + 2\sigma\phi^2 \left( \frac{2(n^2-1)}{n^2} \tan\gamma - \tan\theta \right) + \dots].\end{aligned}\quad (5.4)$$

In order to field widen the system, the coefficient of the quadratic angular terms in equation 5.4 should be set to zero by appropriate choice of the prism angle. Since the coefficients of the angular terms in equation 5.4 are different, only one of the quadratic terms can be set to zero. Setting the coefficient of the  $\phi^2$  term is equal to zero gives

$$2(n^2 - 1)\tan\gamma - n^2\tan\theta. \quad (5.5)$$

Equation 5.5 and the relationship  $n\sin(\alpha/2) - \sin\gamma$  determine the prism angle  $\alpha$  appropriate for field widening in the  $\phi$  direction. Section 5.6 demonstrates that choosing a prism angle, determined by equation 5.5, increases the field of view of the system substantially in the  $\phi$  direction and somewhat in the  $\beta$  direction.

**5.6 Field of View Limits:** The field of view of an SHS instrument can be increased until the number of fringes produced by the extreme rays differs by one from the number of fringes produced by the axial rays, assuming a monochromatic source. In principle, this shift in fringe frequency for off-axis rays can be determined by including higher order terms in the expansions that led to equation 5.4. In practice, however, finding a general expression for the maximum field of view for the field widened system has proven to be difficult so an alternative approach has been pursued. A computer program was written to empirically find the maximal rays in both the  $\beta$  and  $\phi$  directions as a function of resolving power and diffraction angle  $\theta$ . Figures 5.5 through 5.7 show the results of the calculations.

Figure 5.5 plots the  $\phi$  field of view achieved by a field widened SHS instrument versus the grating angle  $\theta$ . The field of view is plotted in units of

**Figure 5.5** Results of a numerical calculation of the maximum field of view achieved in  $\phi$  by the field widened SHS system: The maximum field of view for the system  $\phi_{FWSHS}$  is given in units of the field of view in the conventional SHS system,  $\phi_{SHS} - \sqrt{8/R}$  as a function of grating angle  $\theta$  and resolving power  $R$ .

---

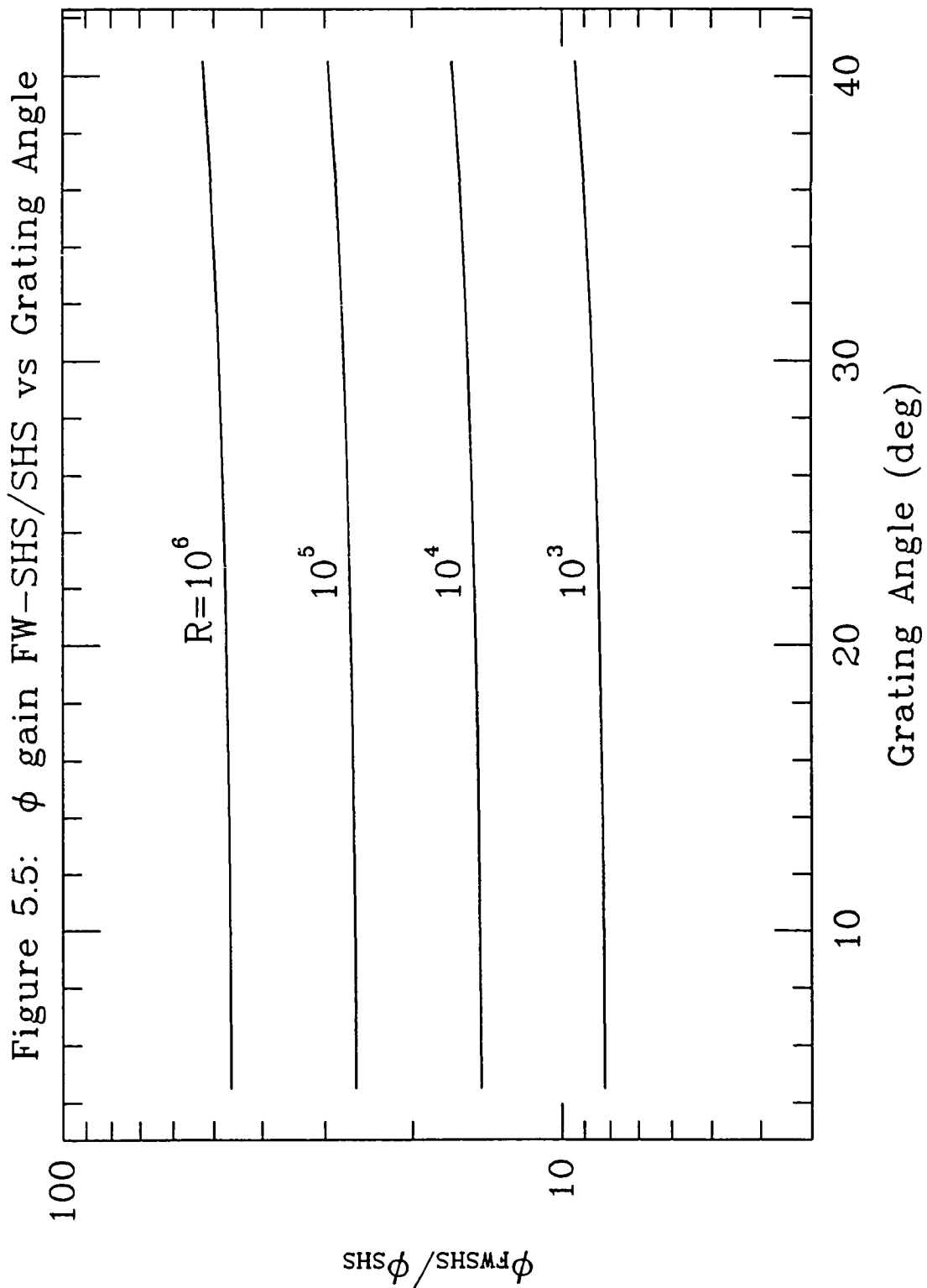


**Figure 5.6** Same as Figure 5.5 except for the angle  $\beta$ : The gains in this figure are modest when compared to Figure 5.5 because the system is field widened in  $\phi$  and not  $\beta$ . The dotted line (almost coincident with the  $R = 10^6$  curve) shows the upper limit determined by the non-zero  $\beta^2$  term in equation 5.4.

---

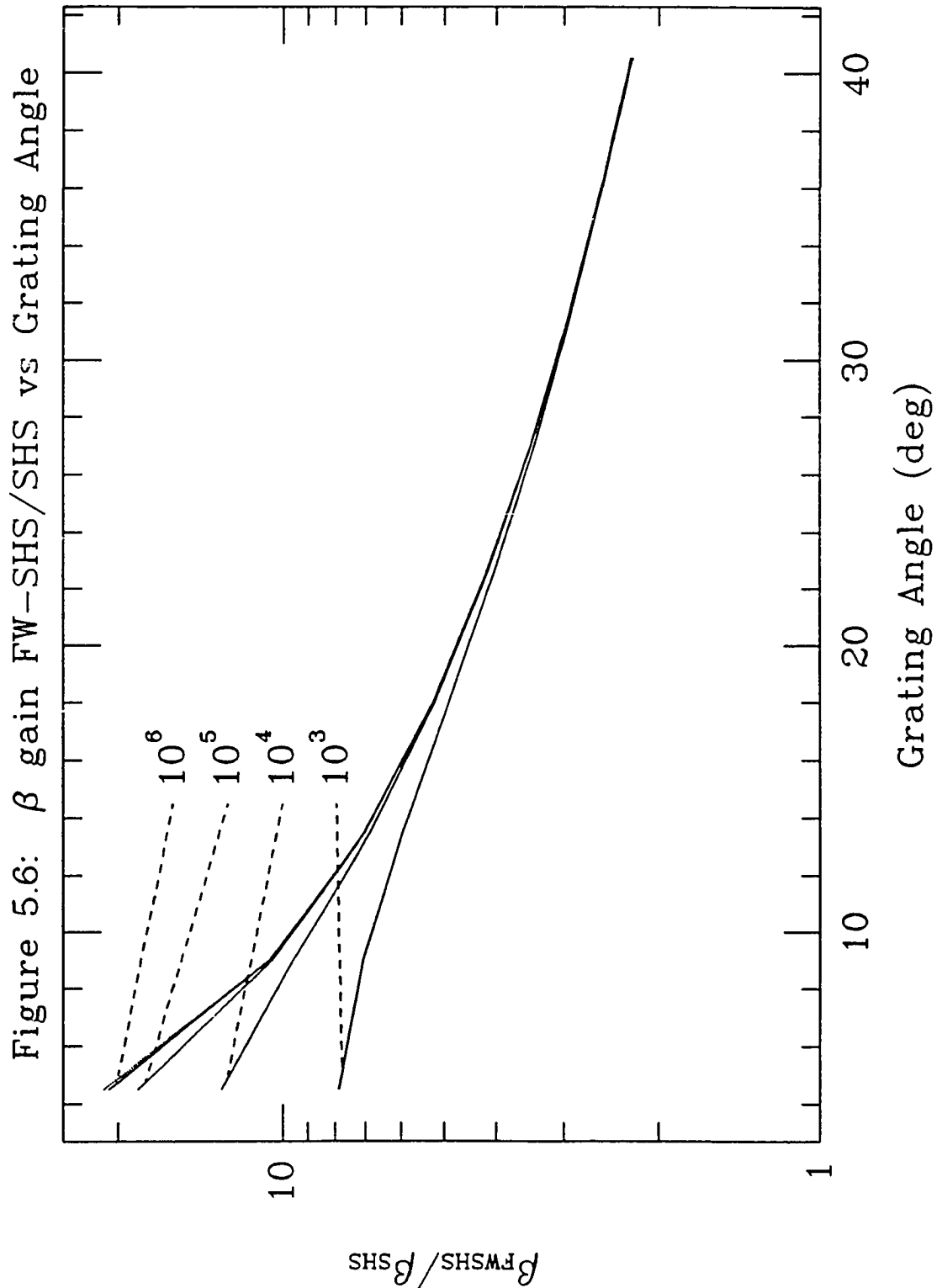
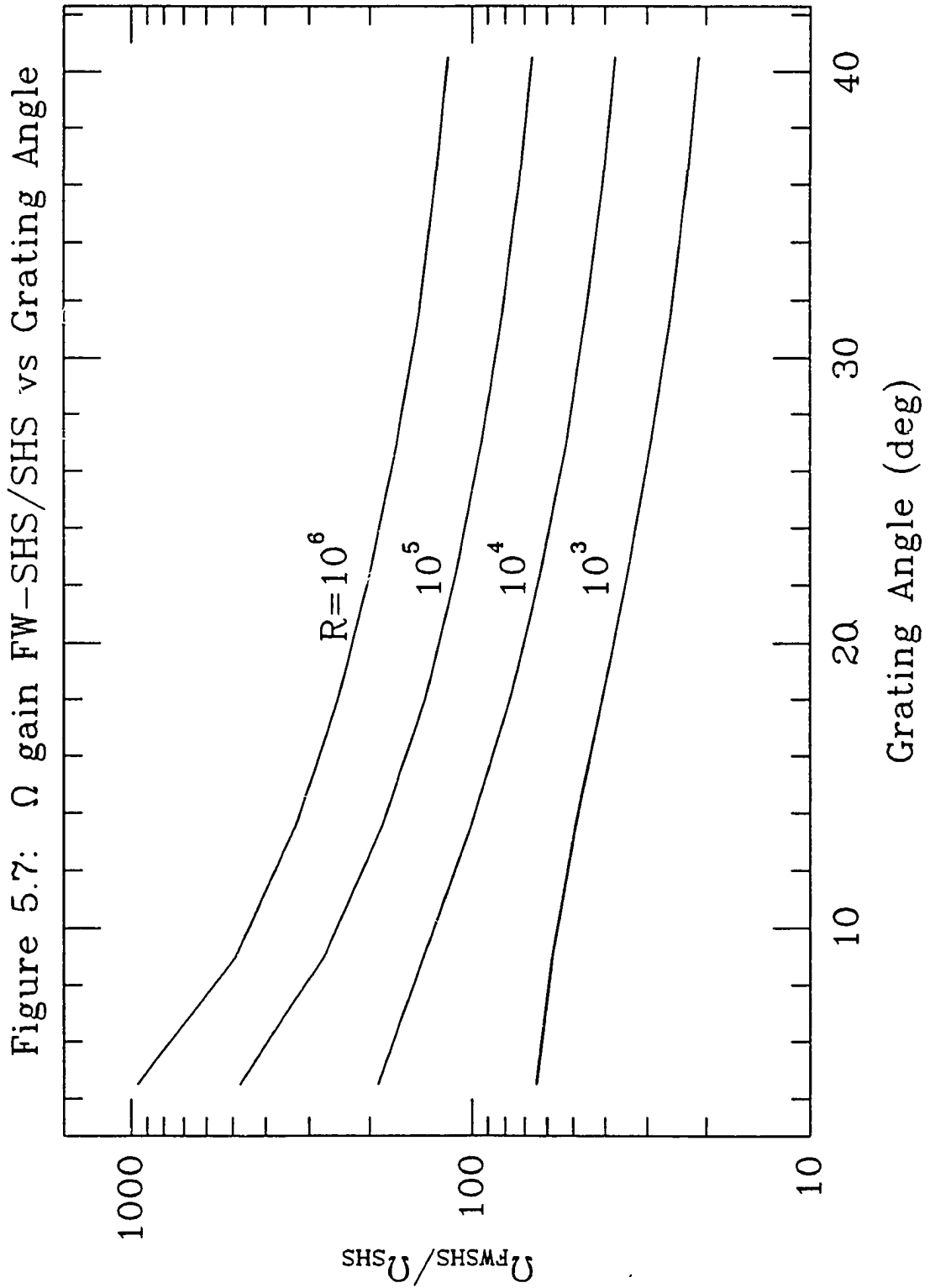


**Figure 5.7** Solid angle gain expected from field widening: This figure is the product of Figures 5.5 and 5.6 and represents the solid angle ( $\Omega$ ) gain expected from the field widened SHS system as a function of grating angle and resolving power.

---



the  $\phi$  field of view of a conventional interferometer operating at the same resolving power. A similar plot for the  $\beta$  direction, the angle in the dispersion plane of the gratings, is shown in Figure 5.6. The modest gains shown in Figure 5.6 reflect the fact that the prism angle was chosen to field widen the system in the  $\phi$  direction and not the  $\beta$  direction. By substituting equation 5.5 back into the coefficient of the (non-zero)  $\beta^2$  term in equation 5.4, an upper limit for the gain in the  $\beta$  direction is obtained. This limit is given by  $G - \cot(\alpha/2)$  and is shown in Figure 5.6 as the dotted line. Figure 5.7 shows the product of the gain achieved in the  $\beta$  and  $\phi$  directions. This figure represents the expected over-all gain afforded by field widening.

**5.7 Achromatic Field Widening:** To this point, the analysis of the field widened system has assumed that dispersion effects introduced by the prisms were negligible. This is the case for high resolution systems, particularly in the visible, where the index of refraction can be assumed to be constant over the small spectral range of the instrument. For systems designed to cover a broad spectral range, (i.e. low resolving power, echelle mode) or systems operating in the far ultraviolet spectral region where dispersion in optical materials is large, achromatic prisms may be required to achieve field widened performance.

Problems arise when the dispersion in the prisms cannot be ignored. The field of view is less than predicted by Figure 5.7 since the index of refraction is a function of wavelength. This being the case, equation 5.5 cannot be satisfied with a single prism for all wavelengths. The dispersion introduced by the prism also contributes to the resolving power of the system. The most serious problems arise when field widening the echelle SHS system discussed in Section 3.4. With the addition of the prisms, the light is dispersed before it arrives at the echelle grating. This means only one of the many Littrow wavenumbers in the echelle system survives in the field widened configuration. The other wavenumbers are incident in a non-Littrow geometry which shifts the spatial frequencies for the blaze peaks associated with these wavenumbers away from zero. If the shifts are large enough, the spatial frequencies may be high enough to exceed the limit set by sampling theory and produce aliased signals at the detector.

The effects of prism dispersion can be ameliorated to some extent by using achromatic prisms (Smith, 1966) to perform field widening. Figure 5.8 shows one arm of the field widened interferometer with an achromatic prism consisting of two oppositely oriented prisms made with different glasses and apex angles. The condition that must be satisfied for the prism to be achromatic at the wavenumbers  $\sigma_a$  and  $\sigma_b$  is given by

**Figure 5.8** One arm of the achromatic field widened SHS system: To achieve field widening when the dispersion effects of a single prism are problematic, an achromatic prism formed by two prisms  $P_1$  and  $P_2$  with apex angles  $\alpha_1$  and  $\alpha_2$  and indices of refraction  $n_1$  and  $n_2$  can be used.

---

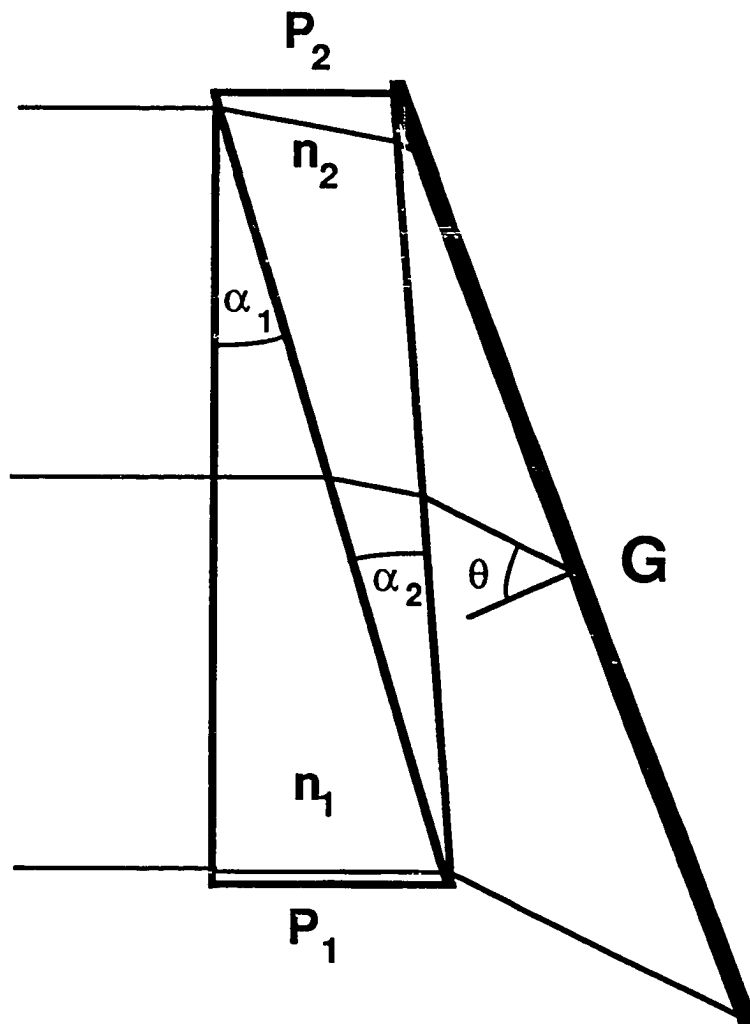


**Figure 5.8**

$$[n_1(\sigma_a) - n_1(\sigma_b)]\alpha_1 - [n_2(\sigma_a) - n_2(\sigma_b)]\alpha_2 \quad (5.6)$$

where  $n_i$  and  $\alpha_i$  are the index of refraction and apex angle of prism i. A simple geometric argument demonstrates that, to first order, field widening can be accomplished by choosing prisms which are related to the grating angle by

$$\theta = \frac{n_1^2 - 1}{n_1} \alpha_1 - \frac{n_2^2 - 1}{n_2} \alpha_2. \quad (5.7)$$

Since the  $n_i$ 's are a function of wavenumber, equation 5.7 can be satisfied only at one particular wavenumber,  $\sigma = \sigma_{FW}$ . For other wavenumbers, the field of view is decreased from the value at  $\sigma_{FW}$ . By choosing  $\sigma_a < \sigma_{FW} < \sigma_b$ , the benefits of the achromatic prism can be incorporated with minimal sacrifice in the field of view.

The resolving power of the achromatic field widened system varies as a function of wavenumber and is determined by the following analysis. The number of fringes detected at a particular wavenumber  $\sigma$  is given, to first order in grating and prism angles, by

$$m = 4W[(\sigma_0 - \sigma)\theta - \alpha_1 \sigma (n_1 - n_{10}) + \alpha_2 \sigma (n_2 - n_{20})] \quad (5.8)$$

where  $n_{i0}$  is the index of refraction at wavenumber  $\sigma_0$ ,  $\alpha_1$  and  $\alpha_2$  satisfy equations 5.6 and 5.7,  $W$  is the width of the grating, and  $\sigma_0$  is the wavenumber for which the system is aligned. Since adjacent resolution elements differ by one fringe at the detector, setting the differential of equation 5.8 equal to 1 and solving for  $\sigma/\delta\sigma$  gives the resolving power of the achromatic field widened SHS system as

$$R_0 = 4W\sigma|\theta + \alpha_1(\sigma \frac{\partial n_1}{\partial \sigma} + n_1 - n_{10}) - \alpha_2(\sigma \frac{\partial n_2}{\partial \sigma} + n_2 - n_{20})|. \quad (5.9)$$

**5.8 All-Reflection Field Widening:** A technique has been conceived that may bring the gains associated with field widening to the all-reflection SHS systems. This technique is currently considered speculative since its practicality has not been demonstrated.

Figure 5.9 is a schematic representation of the field widened all-reflection system. The collimator, exit optics, and imaging detector are not shown. An incident wavefront is diffracted into equal and opposite orders by the beam splitting grating G and combined at grating G' which has a groove spacing slightly different than G. Between the beam split and combine in

---

**Figure 5.9** Conceptual design for a field widened all-reflection SHS interferometer: From a geometrical optics point of view, gratings G and G' are imaged parallel to one another. As a result, there is no geometrical path difference in the system.

---

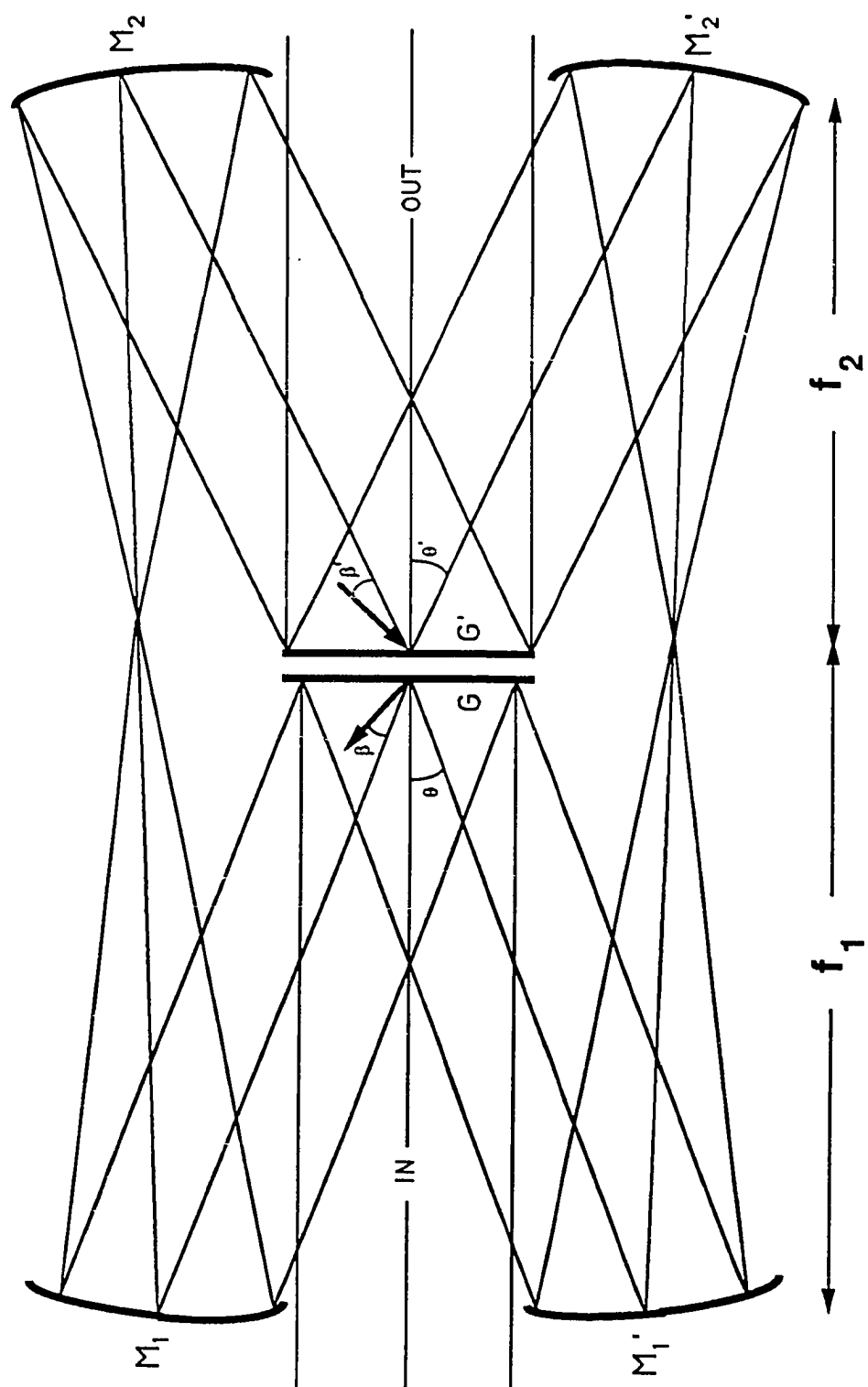


Figure 5.9

each arm is an afocal optical system consisting of two focusing elements,  $M_1$  and  $M_2$  (probably off-axis parabolas). In an aberration free optical system, the rays comprising a plane wavefront diffracting from grating G at an off-axis angle  $\beta$  are focused by mirror  $M_1$ , recollimated by mirror  $M_2$ , and incident on grating  $G'$  as a plane wave at angle  $\beta' - M\beta$  where  $M = f_1/f_2$ . To the extent that aberrations can be ignored, this configuration is field widened for a particular choice of  $\theta$ ,  $\theta'$ , and  $M$ . The Fizeau fringes can be determined for this system by expanding the grating equations for G and  $G'$  including the magnification  $M$ . The result is

$$\begin{aligned}\delta &= (k_{x1} - k_{x2})x \\ &\sim 2\pi x [2\sigma'(\sin\theta' - M\cos\theta'\tan\theta) \\ &\quad + \sigma \left( \frac{\beta^2}{\cos^2\theta} + \phi^2 \right) (M^2\sin\theta' - M\cos\theta'\tan\theta) + \dots].\end{aligned}\tag{5.10}$$

Setting the coefficient of the term quadratic in angles in equation 5.10 equal to zero gives

$$M = \frac{f_1}{f_2} - \frac{\tan\theta}{\tan\theta'}.\tag{5.11}$$

The resolution limit  $\delta_\sigma$  of this system is determined by finding the change in

wavenumber which changes the number of fringes detected by one.

Substituting equation 5.11 back into the first term of equation 5.10, setting

$\partial\delta/\partial\sigma' = \pi$ , and  $x_{\max} = W'/2$ , the resolving power  $R = \sigma/\delta\sigma'$  is then

$$R_0 = 2W'\sigma \sin\theta' (1 - \tan^2\theta \cot^2\theta') \quad (5.12)$$

where  $W'$  is the width of grating  $G'$ .

Figure 5.10 illustrates an alternative configuration for the field widened all-reflection device. Since the focusing optics in this system are used on axis, it is likely to suffer from fewer aberrations than the off axis system in Figure 5.9.

**Figure 5.10** Alternative configuration for the field widened all-reflection interferometer: The focusing elements are nearly on axis in an effort to minimize aberrations. The side view shows a detail of one of the arms. Conceptually, this system is identical to the system illustrated in Figure 5.9.

---

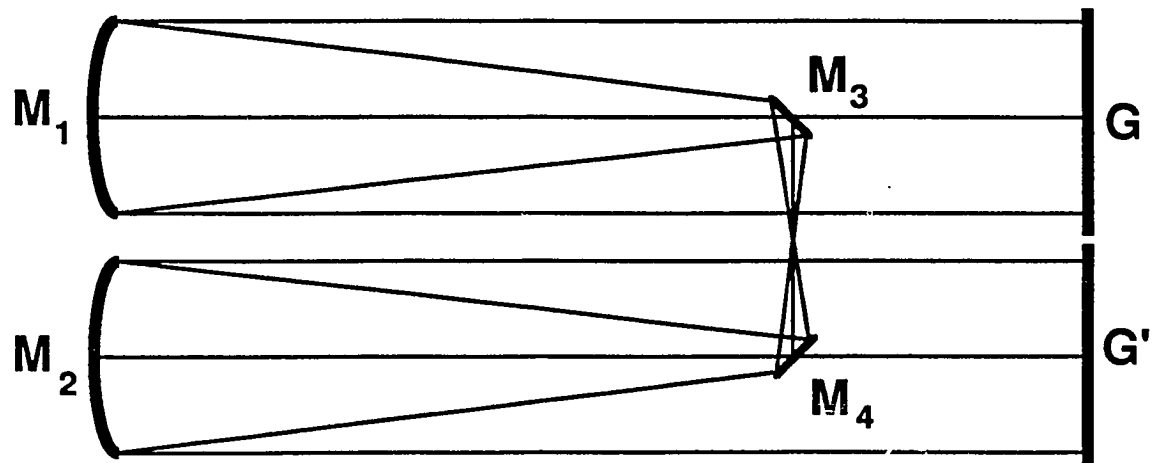
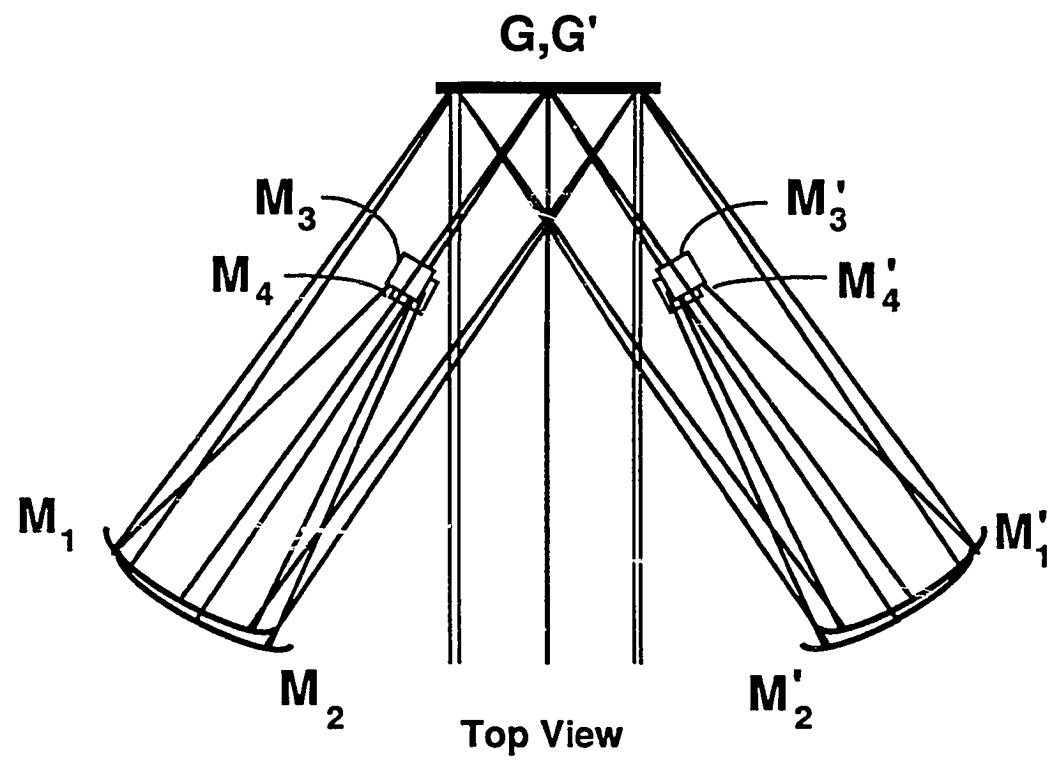


**Figure 5.10**

## 6. Noise Propagation

**6.1 Introduction:** In multiplex spectroscopy a single detector element records light from all spectral elements within the bandpass of the instrument. Each spectral element is coded so the spectrum may be recovered by a mathematical transformation. As a result of multiplex detection, the noise in these systems propagates differently than it does in non-multiplex systems. Noise propagation in Fourier Transform Spectroscopy, a classic example of a multiplex spectrometer, has been studied extensively (Sakai, 1977; Brault, 1985). Since SHS systems also detect photons in the Fourier domain, much of the FTS analysis is applicable to SHS systems.

Chapter 6 discusses issues pertinent to determining the expected signal-to-noise ratio for a particular measurement made with a SHS instrument. When the analysis follows from the FTS case, the discussion will be brief; where the analysis differs, the discussion will be more thorough. The results presented here have not been verified experimentally; however, computer simulations performed with realistic parameters validate the analysis. Most of the analysis in Chapter 6 is general in nature. More specific comments are made in Chapter 7 where SHS systems are compared to other types of instrumentation for specific problems.

**6.2 General Treatment:** A general analysis for predicting the signal-to-noise ratio expected from a dual-output Fourier Transform Spectrometer has been carried out by Brault (Brault, 1985). The analysis assumes the noise in the system has a distribution constant with frequency (white noise). The relationship derived between the signal-to-noise ratio in the spectral domain and the signal-to-noise ratio in the domain of the detector is

$$\left(\frac{s}{n}\right)_{\sigma'} = \sqrt{\frac{2}{N}} \frac{B_e(\sigma')}{\overline{B}_e} \left(\frac{s}{n}\right)_u \quad (6.1)$$

where:

$\left(\frac{s}{n}\right)_{\sigma'}$  = the signal-to-noise ratio in the spectral domain at wavenumber  $\sigma'$ ,

$N$  = the number of samples,

$B_e(\sigma')$  = the effective intensity at wavenumber  $\sigma'$  (section 2.3),

$\overline{B}_e$  = the effective intensity averaged over the number of samples

obtained, and

$\left(\frac{s}{n}\right)_u$  = the signal-to-noise ratio of the detected signal in the sample at zero

path difference ( $u=0$ ).

In a series of computer simulations, equation 6.1 has been shown to predict the signal-to-noise ratio in the spectral domain for SHS systems.

Brault's analysis leading to equation 6.1 assumes a dual-output FTS system. Dual-output FTS systems utilize two detectors to record the interferogram and its complement. The primary advantage of a dual-output system is that approximately twice the number of photons are detected which increases the signal-to-noise ratio of the recovered spectra. The SHS systems described have all been single output devices in which approximately half of the useful light escapes the system via the entrance aperture. To account for this loss in the application of equation 6.1, the optical efficiency of the system will be divided by a factor of 2 (see Section 6.7 for a more accurate assessment of this loss).

**6.3 Photon Limited Detection:** Section 6.3 discusses the predicted performance of SHS systems for situations distinguished by the origin of the noise in the system. In the first case considered, photon (shot) noise is the dominant noise source in the interferogram and in the second case detector noise is dominant.

For the first example, consider the case of a photon counting detector measuring an isolated spectral line with negligible background. The signal-to-noise ratio obtained for a fixed integration time will be compared with the

signal-to-noise ratio achieved using a scanning Fabry-Perot spectrometer of the same size operating at the same resolving power. For simplicity the optical efficiency  $\epsilon$ , including quantum efficiency, is assumed to be the same for both systems.

For the SHS system in the shot noise limit, the signal-to-noise ratio in the  $u=0$  sample is equal to the square root of the number of photons detected at  $u=0$ . This can be expressed as

$$\left(\frac{s}{n}\right)_u = \sqrt{\frac{\epsilon A \Omega}{2N} ST} \quad (6.2)$$

where S is intensity in photons per second per unit area per steradian, T is the total integration time, A is the effective area of the system,  $\Omega$  is the solid angle field of view, and N is the number of samples. The factor of two in the denominator accounts for the loss in efficiency since the system uses a single output.

Setting  $B_\epsilon(\sigma') = S/2$  and  $\bar{B}_\epsilon = S/N$  and substituting equation 6.2 into equation 6.1 gives the signal-to-noise ratio expected from the SHS system as

$$\left(\frac{s}{n}\right)_{SHS} = \sqrt{\frac{\epsilon A \Omega}{4} ST} - \sqrt{\frac{M_{SHS}}{2}} \quad (6.3)$$

where  $M_{SHS}$  is the number of photons detected over the entire detector.

A similar relationship can be derived for the scanning Fabry-Perot spectrometer. The signal-to-noise ratio in the recovered spectrum in this case is

$$\left(\frac{s}{n}\right)_{FP} = \sqrt{M_{FP}} \quad (6.4)$$

where  $M_{FP}$  is the total number of photons detected by the Fabry-Perot system.

If the Fabry-Perot and SHS systems have the same effective area, operate over the same field of view (the SHS system is not field widened), and integrate for the same total length of time, then  $M_{FP} = 2M_{SHS}/N$ . In this equation, the factor of two comes from the single output of the SHS and  $N$  is the number of samples taken with the scanning instrument. The  $N$  appears because the total integration time must be divided between  $N$  samples with a scanning instrument. The relationship between the signal-to-noise ratios achieved with the two systems is

$$\left(\frac{s}{n}\right)_{SHS} = \frac{\sqrt{N}}{2} \left(\frac{s}{n}\right)_{FP} . \quad (6.5)$$

Since the number of samples required to measure a narrow isolated line with

a scanning instrument can be small, the SHS and Fabry-Perot systems achieve a comparable signal-to-noise ratio for the case of a narrow isolated emission line.

As a second example, consider the same two instruments measuring a continuum source in the photon noise limited case. The signal to noise ratio at  $u=0$  for the SHS instrument is given by

$$\left(\frac{s}{n}\right)_u = \sqrt{\frac{\epsilon A \Omega}{2N} \frac{NI\delta\sigma}{2} T} \quad (6.6)$$

where  $I$  is the intensity of the continuum in photons per second per unit area per steradian per unit wavenumber,  $\delta\sigma$  is the spectral resolution, and the other quantities were previously defined. Substituting  $B(\sigma') - \bar{B}_e$  for the continuum case and equation 6.6 into equation 6.1 results in

$$\left(\frac{s}{n}\right)_{SHS} = \sqrt{\frac{\epsilon A \Omega}{2N} I \delta\sigma T} - \sqrt{\frac{M_{SHS}}{N}}. \quad (6.7)$$

For the Fabry-Perot, the signal-to-noise ratio at a particular point in the spectrum is the square root of the number of photons detected at that point. Using the relation  $M_{FP} - 2M_{SHS}/N$ , derived in the last example, for the number

of photons detected by the two systems, the signal-to-noise ratios achieved by the two systems are related by

$$\left(\frac{s}{n}\right)_{SHS} = \frac{1}{\sqrt{2}} \left(\frac{s}{n}\right)_{FP}. \quad (6.8)$$

This analysis assumes the SHS system is prefiltered to the desired bandwidth to avoid multiplex noise from photons outside the spectral region of interest.

When compared with FTS instrumentation in the shot noise limited case, an SHS system achieves the same performance when operating at the same resolving power, field of view, spectral range, and aperture. This result is not surprising since the analysis used to predict the signal-to-noise ratio for SHS systems was borrowed from FTS. Since it can be easily field widened, SHS has an advantage over FTS and Fabry-Perot spectroscopy. The increased field of view achieved by field widened SHS systems can lead to significant gains in sensitivity over conventional techniques.

**6.4 Multiplex Advantage:** The most extensive application of Fourier Transform Spectroscopy is in the infrared spectral region where the dominant noise is usually thermal noise generated by the detector. Since the detector in FTS collects light over the entire etendue from all spectral elements simultaneously, the rate of photon detection for a particular sample is increased in FTS over that of a non-multiplex instrument. Since thermal

detector noise is independent of photon flux, this increase in photon rate results in a higher  $(s/n)_u$  in equation 6.1 and a higher signal-to-noise ratio in the recovered spectrum (Thorne, 1988; Bell, 1972). This increase in signal-to-noise ratio is often called a multiplex gain.

In the case of SHS, the total photon flux is spread out over  $N$  detector elements so the photon rate at a particular detector element is comparable to the photon rate for a non-multiplex system. Therefore, SHS does not enjoy the classical multiplex advantage. However, a partial multiplex gain may be realized for SHS systems since the photon flux for a particular detector element may be higher for the SHS system than in a competing technique. In particular, this is the case for field widened SHS systems. Chapter 7 discusses examples of partial multiplex gains afforded by field widening techniques.

**6.5 Scintillation Noise:** Since FTS systems sample points in the interferogram sequentially, an undesirable modulation can be introduced into the interferogram if the source varies in intensity over the time it takes to record a scan. This unwanted modulation can lead to artifacts (scintillation noise) in the recovered spectrum. Experimental techniques such as rapid scanning and internal modulation have been developed in an attempt to minimize the effects of scintillation noise (Brault, 1985). Since SHS systems

detect the entire interferogram simultaneously, they are immune from scintillation noise. However, SHS systems distribute the interferogram over a number of detector channels which can lead to an analogous distortion if the detector channels are not carefully cross-calibrated.

**6.6 Digitizing Noise:** In multiplex systems, the finite dynamic range of the A/D converter in the detector can lead to noise in the recovered spectrum. Brault (Brault, 1985) has shown that when the digitizing thresholds of the A/D converter are adjusted so the interferogram is just saturated at the brightest sample, the signal to noise ratio in the domain of the detector is

$$\left(\frac{s}{n}\right)_u \sim 3D \quad (6.9)$$

where  $D$  is the dynamic range of the A/D converter. Equation 6.1 then predicts the limiting signal-to-noise ratio due to digitizing noise in the recovered spectrum.

**6.7 Distortions in the Recovered Intensity Distribution:** Two instrumental effects not usually important for FTS spectra, distort the recovered intensity distribution in SHS spectra. Technically, these effects are not a result of noise; however, erroneous results will be obtained if they are not taken into consideration.

The first effect pertains to systems utilizing a single output. This effect

was alluded to in Section 6.1 when a factor of two was introduced into the system efficiency because a single output system detects approximately half of the photons admitted into the system. Strictly speaking, the factor of two is only an approximation. If axial rays are considered, the factor of two is accurate only for the highest spatial frequencies in the interferogram. For the spectral element which produces zero spatial frequency,  $\sigma_0$ , *all* of the axial incident photons are detected. For  $\sigma \neq \sigma_0$ , the efficiency of the system is reduced. Qualitatively this reduction in efficiency results from the absence of photons in the dark portions of the fringes detected by the system. As the spatial frequency increases, the fraction of dark area on the detector oscillates about the value 1/2 and the efficiency of the system follows this oscillation. A simple calculation shows that the efficiency for axial rays is

$$E = \frac{1}{2} \left[ 1 + \text{sinc}\left(\frac{\sigma'}{\delta\sigma}\right) \right] = \frac{1}{2} [1 + \text{sinc}(m)] \quad (6.10)$$

where  $\delta\sigma$  represents one resolution element and  $m$  is the number of fringes measured by the detector. The decrease in efficiency is less noticeable for single output FTS instruments because the non-heterodyned frequencies in the interferogram are much higher. Thus, the sinc function in equation 6.10 is essentially zero.

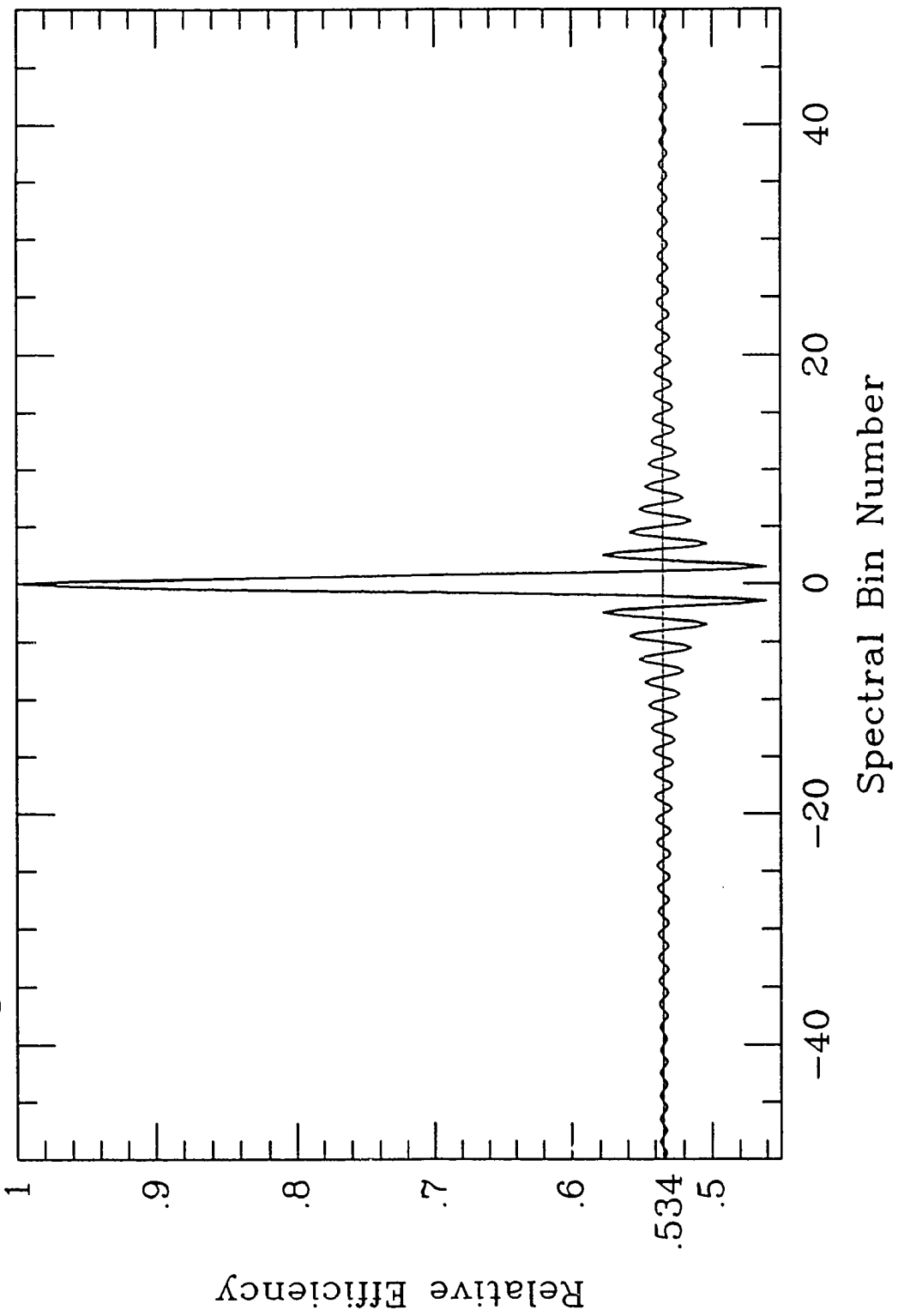
The addition of off-axis rays complicates the above analysis by reducing the efficiency of the system at finite path differences. In this case, the relative efficiency as a function of wavenumber can be calculated by integrating equation 2.19 over the entire range of path differences recorded ( $-U_{\max}$  to  $U_{\max}$ ) and normalizing the result with the value of the integral at  $\sigma' = 0$ . Figure 6.1 shows the result of this integration performed numerically as a function  $m$ , where  $m = \sigma'/\delta\sigma$ .

Another result of working with a single output system is difficulty in recovering the intensity at wavenumber  $\sigma_0$ . Since the interferogram is proportional to  $I_0(1 + \cos 2\pi u\sigma')$  and not  $I_0 \cos 2\pi u\sigma'$ , every spectral element has a zero spatial frequency component. The recovered intensity at  $\sigma' = 0$  represents the sum of all spectral elements in the spectrum. To remove the large feature at  $\sigma' = 0$  from the transforms shown in the system tests of Chapters 1 and 3, the average of the interferogram was subtracted prior to transforming. Therefore, spectral information at  $\sigma_0$  was lost. A dual output system is immune from this problem because it records  $I_0(1 - \cos 2\pi u\sigma')$  in addition to  $I_0(1 + \cos 2\pi u\sigma')$ . These two responses can be subtracted from one

**Figure 6.1** Efficiency of the single output system as a function of wavenumber: Results of a numerical integration of equation 2.19 over the full path difference recorded by the basic SHS instrument. In the absence of other effects, this curve represents the intensity recovered by a single output SHS system.

---

Figure 6.1: Efficiency of Single Output System



another without loss of the  $\sigma' - 0$  spectral information.

The second effect which distorts the recovered intensity distribution in SHS systems results from the manner in which the interferogram is sampled. FTS systems typically sample the interferogram by a step and hold system so that each sample records a particular value of path difference  $u$ . In SHS systems, each sample represents a range of path difference due to the finite pixel size on the imaging detector. At the highest frequencies in the bandpass of the instrument, the contrast of the sampled spectrum is reduced and therefore, the recovered intensity is reduced as well. Mathematically, the blurring can be represented by the convolution

$$I'(u) = I(u) \star \prod\left(\frac{u}{\delta u}\right) \quad (6.11)$$

where  $I(u)$  is the interferogram sampled at discrete path differences,  $\prod$  is the rectangle function, and  $\delta u$  is the range of path difference spanned by one sample. The Fourier transform of equation 6.11 is proportional to

$$B(\sigma') \text{sinc}(\sigma' \delta u). \quad (6.12)$$

The sinc function in equation 6.12 represents the distortion in the recovered intensity. Light at the highest spatial frequency  $\sigma'_{\max} - 1/2\delta u$  is reduced in

intensity by a factor of  $\text{sinc}(1/2) \sim 0.637$ . Equation 6.12 also predicts the recovered intensity for aliased wavenumbers ( $\sigma' > 1/2\delta u$ ). Although intensities at aliased wavenumbers are recovered at reduced intensity, the photons at these aliased frequencies still contribute shot noise.

## 7. Performance Prediction and Comparison

**7.1 Introduction:** The test of a spectroscopic technique takes place when comparing its performance against competing techniques for selected problems. Chapter 7 is a discussion of 'paper studies' that have been performed to compare SHS systems with other spectroscopic techniques. The discussion begins with systems that are designed for measuring geocoronal Balmer-alpha line profiles from the ground. The chapter continues with a comparison of techniques for measuring global maps of the diffuse interstellar medium in the far-ultraviolet spectral region from space. For each of these problems, SHS systems are shown to be superior to the other techniques.

**7.2 Geocoronal Balmer-alpha Emission Instrument:** This section investigates the potential of SHS for ground-based studies of geocoronal Balmer-alpha line profile measurements. Two prototype field-widened SHS systems are compared with two Fabry-Perot systems currently employed for such measurements. The conventional techniques that will be compared to the field-widened SHS systems are 1) a dual-etalon Fabry-Perot/photomultiplier scanning spectrometer (FP/PMT) and 2) a dual-etalon Fabry-Perot/CCD multichannel spectrometer (FP/CCD) (Reynolds et al., 1990). The FW-SHS systems require prefiltering to prevent photon noise

outside the spectral range of interest from contaminating the spectrum. For the first SHS system, prefiltering can be accomplished with existing techniques. The second SHS system requires a prefilter which is difficult to conceive. This "impractical" system is discussed to illustrate the potential of FW-SHS in situations which are not dominated by background light. In this case, the requirements on the prefilter are not as severe as for geocoronal Balmer-alpha measurements.

Geocoronal Balmer-alpha line emission is produced by the scattering of solar Lyman-beta radiation within the geocorona. The intensity of the emission is very faint, typically  $0.5 - 15 \text{ R}$  ( $1 \text{ R} = 10^6/4\pi \text{ ph cm}^{-2} \text{ s}^{-1} \text{ sr}^{-1}$ ). If dynamical information is to be derived from the line profiles, the resolving power required is  $\sim 100,000$  ( $\Delta v = 3 \text{ km s}^{-1}$ ). In the vicinity of the Balmer-alpha line the sky background is  $\sim 12 \text{ R}/\text{\AA}$ . This means the signal from the background in a  $3 \text{ km s}^{-1}$  spectral slice is approximately equal to the signal at the peak of a  $1 \text{ R}$  emission line. Before discussing the SHS systems, the current technology and performance of the conventional Fabry-Perot systems used for comparison will be reviewed.

Over the past decade, the dual-etalon Fabry-Perot/PMT scanning spectrometer has been used at the University of Wisconsin-Madison for the study of geocoronal Balmer-alpha radiation. The spectrometer consists of two

15 cm aperture pressure-scanned Fabry-Perot etalons operating in an axial scanning mode. At the exit of the system, light within approximately  $0.25^\circ$  of the optical axis is passed through an interference filter to a GaAs photomultiplier (PMT). The system is sequentially scanned through 20 resolution elements to obtain a spectrum of the night sky at Balmer-alpha.

The Fabry-Perot/CCD multichannel spectrometer, which represents the current state of the art in geocoronal Balmer-alpha measurements, has been field tested and is presently being integrated into observing campaigns. In the multichannel system all spectral channels are simultaneously sampled by imaging the ring pattern produced by the Fabry-Perot etalons onto the CCD detector. Each spectral element in the system views a solid angle on the sky equal to the solid angle seen by the scanner. Since all elements are viewed in parallel, the system views 20 times the solid angle of the scanning instrument. In addition to the gain associated with parallel detection, the CCD detector also has a higher quantum efficiency than the PMT. These gains are partially offset by read noise generated in the CCD detector. For studies of Balmer-alpha at a resolution of  $3 \text{ km s}^{-1}$ , each spectral element requires approximately 370 reads of the CCD to recover one ring of the Fabry-Perot pattern from the square format of the CCD. Relevant parameters for the scanning and multichannel Fabry-Perot systems are shown

in the first two columns of Table 7.1.

For the Fabry-Perot systems, Reynolds et al. (1990) derived a relationship which compares the signal  $s$  at the peak of an emission line after a time  $t$  to the noise  $n$  in an off-line spectral element. The relationship is

$$\frac{s}{n} = \frac{LQt}{(SQt + Dt + NR^2)^{1/2}} \quad (7.1)$$

where  $Q$  is the quantum efficiency of the detector,  $L$  and  $S$  the incident (on the detector) photon rates due to the emission line (peak) and sky continuum, respectively,  $D$  the dark rate per spectral element,  $R$  the read noise, and  $N$  the number of reads per spectral element. Appropriate values for substitution into equation 7.1 are obtained from field tests of the Fabry-Perot systems.

For the Fabry-Perot/PMT, system  $L \sim 9.5 \text{ s}^{-1}$  per rayleigh of geocoronal Balmer-alpha and  $S \sim 9.5 \text{ s}^{-1}$  in a  $3 \text{ km s}^{-1}$  resolution element. For the photomultiplier  $D = 2 \text{ s}^{-1}$ ,  $R = 0$ , and  $Q = 0.2$  at  $\text{H}\alpha$ . Therefore, to obtain a signal-to-noise ration of 20 for a typical 1 R line with this system requires an integration time of 500 s. An entire scan consisting of 20 such intervals requires  $10^4$  s. The large signal-to-noise ratio is chosen so the wings of the line profile can be extracted reliably.

Equation 7.1 also predicts the performance of the Fabry-Perot/CCD

**TABLE 7.1**  
Comparison of Geocoronal Balmer-alpha Systems

|   | FP/PMT             | FP/CCD  | FW-SHS   | FW-SHS FULL |
|---|--------------------|---|----------|-------------|
| Plate Aperture                            | 15 cm              | 15 cm   | 5 cm     | 15 cm       |
| <u>FOV</u>                                |                    |   |          |             |
| $\beta_{\max}/\beta_{\text{PMT}}$         | 1                  | 4.5   | 5        | 14          |
| $\phi_{\max}/\phi_{\text{PMT}}$           | 1                  | 4.5   | 20       | 28          |
| $\Omega_{\max}/\Omega_{\text{PMT}}$       | 1                  | 20  | 100      | 400         |
| $(A\Omega)_{\max}/(A\Omega)_{\text{PMT}}$ | 1                  | 20  | 14       | 500         |
| <u>Prefilter</u>                          | 15 cm FP + IF      | 15 cm FP + IF                                     | 15 cm IF | ?           |
| bandpass                                  | 0.5 Å              | 0.5 Å   | 1.3 Å    |             |
| <u>Detector</u>                           | PMT                | CCD   |          |             |
| QE  | 0.2                | 0.5   |          |             |
| Dark noise                                | $2 \text{ s}^{-1}$ | $0.15 \text{ e}^- \text{ nm}^{-2} \text{ s}^{-1}$ |          |             |
| Read noise                                | -                  | 8 e <sup>-</sup> RMS                              |          |             |
| Reads/spectral element                    | -                  | 370   | 2        | 2           |

system for geocoronal Balmer-alpha line profiles. Since the optics are unchanged from the PMT system, the only parameters which change in the application of equation 7.1 to the CCD system are those associated with the detector. Table 7.1 lists the parameters for the CCD detector as: Q = 0.5,

$D = 10 \text{ s}^{-1}$ ,  $N = 370$ , and  $R = 8$ . The dark noise  $D$  for the CCD is determined by considering the area one spectral resolution element occupies on the imaging detector assuming a  $f/1$  focusing system. For the FP/CCD system, equation 7.1 predicts a signal-to-noise ratio of 20 for a 1 R line in an integration time of 800 s. Since all spectral elements are measured in parallel, this is also the integration time required to recover the entire spectrum.

The parameters for a practical field-widened SHS system designed for geocoronal Balmer-alpha line profiles are shown in the third column of Table 7.1. The detector used in this system is the same CCD used in the Fabry-Perot/CCD system. A 5 cm aperture was chosen for the system in a effort to reduce the cost of the optical components, especially when compared to the 15 cm aperture Fabry-Perot systems. To achieve a resolving power of 100,000 at  $H\alpha$ , the grating angle is  $\theta = 18^\circ$  (cf. equation 2.14). The maximum extent this system can be field-widened is predicted by Figures 5.5 and 5.6.

Table 7.1 shows the field of view for the FW-SHS system is 20 times larger in the  $\phi$  direction and 5 times larger in the  $\beta$  direction than the field of view of the Fabry-Perot/PMT system. In the  $\phi$  direction, the gain is less than that predicted by Figure 5.5 because the field of view is limited by the prefilter required for the system. The prefilter chosen was a 15 cm aperture

solid-gap Fabry-Perot with blocking filters to cancel repeated orders. A bandpass equal to the spectral range of interest ( $\delta\lambda - 1.3 \text{ \AA}$ ) eliminates excess background photons which contribute noise. This narrow bandpass is what ultimately limits the field of view of the SHS system. The field of view of a solid gap Fabry-Perot etalon is given by  $n(8\delta\lambda/\lambda)^{1/2}$  where  $n$  is the index of refraction in the gap and  $\delta\lambda$  is the bandpass. Assuming  $n = 1.5$  and taking into account the 3:1 magnification between the filter and the SHS system, the limiting gain in field of view is determined. The 15 cm filter is probably the most expensive optical element in this system, comparable in cost to one of the etalons in the dual-etalon Fabry-Perot systems. An alternative to this large prefilter might be a mosaic of smaller filters or a narrow-band, wide-field filter such as a wide-field Lyot or Solc filter (Evans, 1949). It has yet to be determined if wide-field filters with large apertures can be produced at a reasonable cost.

The last column of Table 7.1 shows the design parameters for an impractical field-widened SHS system. This system is not practical because it is difficult to conceive of a prefilter with a narrow bandpass and enough throughput to fill the SHS system with light. Irrespective of this limitation, the system illustrates the potential of a 15 cm aperture FW-SHS instrument operating over the full field of view predicted by Figures 5.5 and 5.6. In

situations where background light is negligible, the restriction imposed by the prefilter is not severe and a system operating with full field-widening might be practical.

The signal to noise ratio expected from these field-widened SHS systems can be calculated using equation 6.1:

$$\left(\frac{s}{n}\right)_{\sigma'} = \sqrt{\frac{2}{N} \frac{B_e(\sigma')}{B_e}} \left(\frac{s}{n}\right)_u. \quad (6.1)$$

Assuming the efficiency of the optics in the SHS systems is equal to the efficiency for the Fabry-Perot systems, the photon rates S and L associated with signal and background, respectively, will increase by a factor of  $(A\Omega)_{SHS}/(A\Omega)_{PMT}$  over the rates seen with the Fabry-Perot PMT system. This ratio is tabulated for the various systems in Table 7.1. After substituting the appropriate parameters into equation 6.1, it can be written as

$$\left(\frac{s}{n}\right)_{\sigma} = \frac{G Q I_r L t}{\sqrt{2(GQ(I_r L + NS/2)t + NDt + NR^2)^{1/2}}} \quad (7.2)$$

where  $G = (A\Omega)_{SHS}/(A\Omega)_{PMT}$ ,  $I_r$  is the intensity of the emission line in raylieghs,  $N = 40$ , and the other parameters are defined in discussion of the Fabry-Perot instruments. Note the SHS system requires only 40 samples

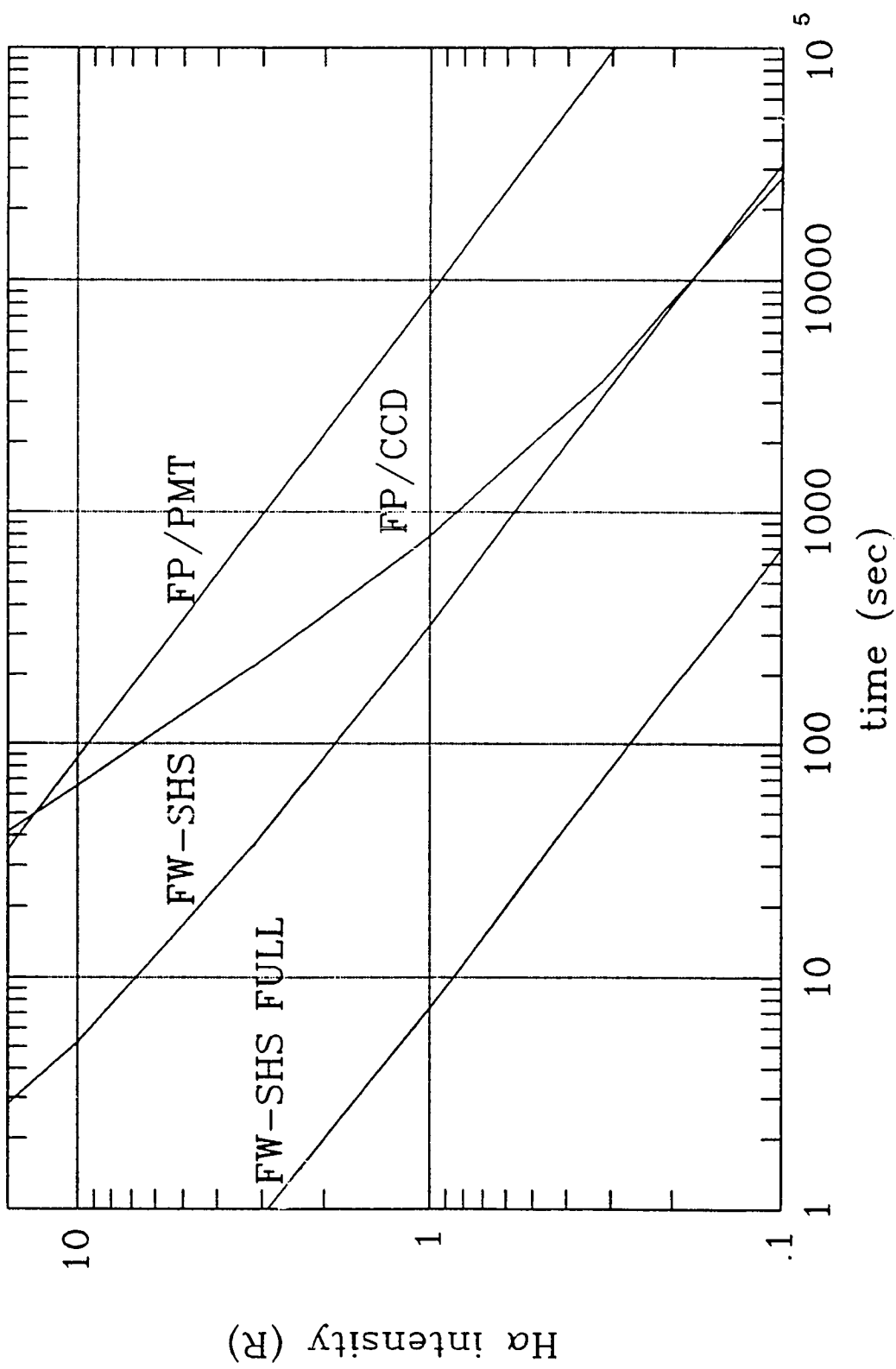
(reads) to recover 20 resolution elements whereas the Fabry-Perot/CCD system requires 370 reads of the CCD per spectral element.

Figure 7.1 illustrates the performance of the four systems discussed above by plotting for each the time  $t$  required to achieve a signal-to-noise ratio of 20 on the geocoronal emission line as a function of geocoronal intensity  $I$ . The Fabry-Perot/PMT system requires the longest integration times of the four, needing almost 2.7 hr to measure a 1 R line. The Fabry-Perot/CCD system shows significant gains over the Fabry-Perot/PMT system requiring an integration time 10 times shorter at  $I = 1$  R. For short integration times,  $I \propto t^{-1}$  for the FP/CCD system because read noise in the CCD is the dominant noise source in the system. As the integration time is increased, the detection becomes photon noise limited ( $I \propto t^{-1/2}$ ) and the reduction in integration time over the PMT system approaches 50 fold. This is the expected gain for a zero read noise FP/CCD system since it is equal to the throughput gain of the system multiplied by the ratio of the quantum efficiencies of the CCD and PMT.

The FW-SHS curve in Figure 7.1 shows a gain over the Fabry-Perot/CCD system through most of the intensity range considered. Only at the lowest intensities where the Fabry-Perot/CCD system becomes photon noise limited does the FP/CCD system, by virtue of its higher throughput,

**Figure 7.1** Intensity of geocoronal Balmer-alpha versus time required to achieve a signal-to-noise ratio of 20 for the four interferometers discussed in the text.

---

Figure 7.1: Intensity of H $\alpha$  vs time for S/N = 20H $\alpha$  intensity (R)

achieve a shorter integration time than the FW-SHS system. The curve labeled FW-SHS is basically a straight line consistent with  $I \propto t^{-1/2}$ . This system uses the same detector as the Fabry-Perot/CCD system; however, it performs as if the detection is photon limited over the entire range of intensities. The photon limited performance results from the FW-SHS system detecting more photons per readout of the CCD than the Fabry-Perot system. The SHS system accumulates more photons per read for two reasons. First, the image format of the one-dimensional Fizeau fringe pattern is more compatible with the square pixel format on the CCD. The entire spectrum can be recovered with 40 readouts of the CCD as opposed to 7400 with the Fabry-Perot system. Second, each spectral element in the SHS systems sees the entire throughput of the device. In contrast, the field of view of the Fabry-Perot system is divided into distinct spectral elements. In the Fabry-Perot system all spectral elements are detected simultaneously, but each element sees only a fraction of the total field of view.

The curve labeled FW-SHS FULL in Figure 7.1 shows enormous gains over the other three systems. However, it is not practical for geocoronal Balmer-alpha because of difficulty conceiving of an appropriate prefilter.

**7.3 Far Ultraviolet Interstellar Medium System:** The objective of the FUV interstellar medium mapping instrument is to obtain a velocity resolved

map of interstellar medium emission lines in the spectral region from 1350Å to 1950Å. These measurements would help resolve the current debate as to the extent to which hot gas ( $T \sim 10^5$ ) influences the overall structure and dynamics of the interstellar medium and galactic halo (Jakobsen and Kahn, 1986; Martin and Bowyer, 1990). Martin and Bowyer (1990) were the first to measure this gas in emission; their measurements will be used to determine the characteristics of the instrumentation discussed in this section.

The resolving power ( $\sigma/\delta\sigma$ ) required to dynamically resolve the emission features is  $\sim 20,000$ , and for compatibility with Small Explorer-class satellite missions, a maximum time of about 1 year was chosen to complete a survey of one hemisphere. A spatial scale of  $\sim 2^\circ \times 2^\circ$  was chosen to be compatible with the HI 21cm radio surveys of the interstellar medium. The source is assumed to be comprised of lines of intensity  $2500 \text{ ph cm}^{-2} \text{ s}^{-1} \text{ sr}^{-1}$  with a background of  $4000 \text{ ph cm}^{-2} \text{ s}^{-1} \text{ sr}^{-1} \text{ nm}^{-1}$ , consistent with the Martin and Bowyer result. A  $1000 \times 1000$  pixel photon counting array with  $20\mu\text{m}$  pixels and a CsI photocathode is assumed as the detector. A  $\text{BaF}_2$  window on the detector eliminates the strong Ly- $\alpha$  and OI 1304Å airglow. In this system, prefiltering is achieved by the cutoff of the photocathode and the transmitting materials at long and short wavelengths, respectively. Efficiencies

of the optical components are as follows: mirrors 0.8; gratings 0.4; transmitting optics 0.8; and detector quantum efficiency 0.2.

The field widened echelle SHS system under consideration is comprised of gratings 5 cm x 5 cm of groove density 5 g/mm operating at a blaze angle of  $0.86^\circ$  in orders 30 through 44. A  $\text{MgF}_2$  beam-splitter and achromatic field widening prisms using  $\text{MgF}_2$  and  $\text{CaF}_2$  were chosen to achieve field widened performance at  $\lambda - 1650\text{\AA}$ . Achromatic field widening prisms are required because of the large bandwidth of the instrument and inherent dispersion of optical materials in the VUV. The system is designed to be achromatic at  $\lambda - 1350\text{\AA}$  and  $\lambda - 1750\text{\AA}$  (cf. equation 5.6). The combination of equations 5.6 and 5.7 give the prism angles appropriate to achieve field widened performance as  $2.41^\circ$  for  $\text{MgF}_2$  and  $3.14^\circ$  for  $\text{CaF}_2$ . Computer modeling of the system indicates it achieves a  $15^\circ \times 15^\circ$  field of view over the entire spectral range of the instrument. As a result, a 38 cm 'light bucket' telescope is required to match the spatial scale to  $\sim 2^\circ \times 2^\circ$ . For this system to achieve a signal-to-noise ratio of 10 on the emission features, an integration time of  $\sim 36$  min for one spatial resolution element, as predicted by equation 6.1, is necessary. Hence, a hemisphere of sky consisting of 6500 spatial elements could be mapped in  $\sim 0.45$  yr, well within

the lifetime of a Small Explorer satellite.

The conventional spectrometer chosen for comparison utilizes a 30 cm x 60 cm 63° echelle grating, a cross disperser, and an f/2.5 camera. The field of view is limited by the size of the detector to 0.7 arcmin in the dispersion direction and 1 arcmin along the slit. A simple sensitivity calculation, including estimates of the optical efficiency of the components, predicts 9 hr of integration is required to obtain a signal-to-noise ratio of 10 for one spatial element. A hemisphere survey would then require 6.8 yr. If a detector of four times the area is used, the total observation time is reduced to 1.7 yr, a time frame too long to consider for a Small Explorer mission. The size of the echelle instrument is another limiting factor if the mission is to be performed from the Small Explorer platform.

As another figure of merit of the field-widened SHS system, consider the effective area x field of view product ( $\epsilon A\Omega$ ) of the SHS system compared to the  $\epsilon A\Omega$  product of the ISM instrument flown by Martin and Bowyer (1990). For the Martin and Bowyer instrument,  $\epsilon A\Omega_{mb} = 1.2 \times 10^{-4} \text{ cm}^2 \text{ sr}$  at 1550 Å while the field-widened SHS instrument discussed here has  $\epsilon A\Omega_{SHS} = 3.6 \times 10^{-3} \text{ cm}^2 \text{ sr}$ , a factor of 30 increase *with 200 times the spectral resolution*. The reduction in integration time, however, is somewhat less than

30 since photon noise propagates differently in the two systems.

Recent advances in Vacuum Ultraviolet (VUV) interference filters (Zukic et al., 1990) may make a sounding rocket demonstration of a field-widened SHS system designed for a single interstellar emission line a practicality. These filters have transmissions of greater than 25% and bandpasses less than 5 nm in the VUV spectral region. If one of the many interstellar emission lines in this region is selected with a filter, the spectral range of the instrument can be reduced significantly. The reduction in spectral range reduces the photon noise in the system and results in a shorter integration time to achieve a particular signal-to-noise ratio on a single emission line. The system is also simplified because the spectral range is decreased from the broadband instrument and achromatic prisms are no longer necessary to achieve field widening. For a sounding rocket demonstration of the SHS technique using one of these filters, one spatial resolution element could be obtained at the  $10\sigma$  confidence level in  $\sim 6$  min. This integration time is comparable to the integration time available in a sounding rocket flight. Table 7.2 summarizes the system parameters and integration times for the FUV interstellar medium instrumentation.

**Table 7.2**  
**Performance Prediction-Comparison**  
**FUV-ISM  $\lambda$  1350 -  $\lambda$  1950**

|  | Echelle Grating                 | FW-SHS                     | FW-SHS<br>single line      |
|--|---------------------------------|----------------------------|----------------------------|
| Disperser Size                             | 30cm X 60cm                     | 5cm X 5cm                  | 5cm X 5cm                  |
| Resolution Limit                           | $15 \text{ km s}^{-1}$          | $15 \text{ km s}^{-1}$     | $15 \text{ km s}^{-1}$     |
| Instrumental FOV                           | $0.7 \times 1.4 \text{ arcmin}$ | $15^\circ \times 15^\circ$ | $15^\circ \times 15^\circ$ |
| $\epsilon A \Omega \text{ cm}^2 \text{ s}$ | $1.4 \times 10^{-6}$            | $3.6 \times 10^{-3}$       | $4.5 \times 10^{-3}$       |
| Light bucket size                          | 1.5 cm                          | 38 cm                      | 38 cm                      |
| FOV w/telescope                            | $2^\circ \times 2^\circ$        | $2^\circ \times 2^\circ$   | $2^\circ \times 2^\circ$   |
| Time/resel ( $\sigma - 10$ )               | 9 hr                            | 36 min                     | 6 min                      |
| Time/6500 resels                           | 6.7 yr                          | 0.45 yr                    | 0.9 mo                     |

### **8. Summary and Suggestions for Future Research**

Spatial Heterodyne Spectroscopy, developed at The University of Wisconsin-Madison, possesses a number of properties that promise advantages in many areas of spectroscopy. No moving parts are required, the high etendue characteristic of interference spectroscopy is achieved, and field widening techniques can be applied to further increase the etendue without complex scan and control mechanisms. Since SHS, in principle, can be built in all-reflection configurations, the technique can be extended to any wavelength region.

This work concentrated on the initial development of SHS. Basic properties of the device were derived, often times adapting similar analysis preformed for Fourier Transform Spectroscopy. Also, first order system tests were described; however, these tests were performed with equipment that was either on short-term loan or of insufficient precision to investigate more than the first order properties of the various systems. When experimental evidence could not be obtained, computer modeling was substituted. To demonstrate the competitiveness of the SHS technique, its expected performance was compared to conventional spectroscopic techniques for studies of geocoronal Balmer-alpha emission and for studies of the diffuse galactic emission line

background in the far-ultraviolet.

The investigation of SHS properties is far from complete. The system tests presented in Chapters 1 and 3 need to be extended to address the more subtle issues raised. Major items discussed in the text needing verification in the laboratory include: a measurement of the signal-to-noise ratio achieved with a SHS system at low light level, a demonstration of the field widened systems (both visible and all-reflection), laboratory demonstration of the echelle concept, and verification and implementation of the fringe correction scheme discussed in Section 1.5. For the interstellar medium SHS instrument, outlined in Section 7.3, the suitability and precision of transmitting materials in the far-ultraviolet must be demonstrated in the laboratory. Recently, funding was secured for the next stage of laboratory testing so many of these tests are forthcoming.

In addition to laboratory tests, additional issues related to the performance of SHS systems should be investigated. Dielectric multilayer coatings designed to enhance the reflectivity of surfaces need to be investigated in an effort to extend SHS into the extreme ultraviolet. Of particular importance are the recent developments in dielectric multilayer coatings for diffraction gratings (Ritva, 1990). Various types of prefilters should also be investigated, especially filters which provide a large field of

view since they are of particular importance to the field widened systems. Finally, studies of the performance and competitiveness of SHS systems must continue in an effort to discover additional areas where SHS is superior to conventional techniques.

### References

- Baker, D. (1977). Field widened interferometers for Fourier spectroscopy. In G.A. Vanasse (Ed.), *Spectrometric Techniques: Vol. 1* (pp. 71-106). New York: Academic Press.
- Bell, R.J. (1972). *Introductory Fourier transform spectroscopy*. New York: Academic Press.
- Bouchareine, P. & P. Connes (1963). Interferometre a champ compense pour spectroscopie par transformation de Fourier. *Le Journal de Physique et le Radium*, **24**, 134-138.
- Braultz, J.W. (1985). Fourier transform spectroscopy. In A. Benz, M. Huber, & M. Mayor (Eds.), *High Resolution in Astronomy: Fifteenth Advanced Course of the Swiss Society of Astronomy and Astrophysics* (pp. 1-61). Sauverny, Switzerland: Geneva Observatory.
- Butcher, H., N. Douglas, S. Frandsen, & F. Maaswinkel (1989). A practical non-scanning FTS for astronomy, *High Resolution Fourier Transform Spectroscopy, 1989 Technical Digest Series* (Vol. 6, pp. 9-12). Optical Society of America.
- Connes, P. (1958). Spectrometre interferentiel a selection par l'amplitude de modulation. *Le Journal De Physique et le Radium*, **19**, 215-222.

- Dohi, T. & T. Suzuki (1971). Attainment of high resolution holographic Fourier transform spectroscopy. *Applied Optics*, **10**, 1137-1140.
- Douglas N.G, H.R. Butcher, & M.A. Melis (1990). Heterodyned, holographic spectroscopy - first results with the FRINGHE spectrometer. *Astrophysics and Space Science*, **171**, 307-318.
- Evans, J.W. (1949). The birefringent filter. *Journal of the Optical Society of America*, **39**, 229-242.
- Fonck, R.J., D.A. Huppler, F.L. Roesler, D.H. Tracy, & M. Daehler (1978). All-reflection Michelson interferometer: analysis and test for far ir Fourier spectroscopy. *Applied Optics*, **17**, 1739-1747.
- Fonck, R.J., & F.L. Roesler (1980). *Analysis of a three grating all-reflection interferometer*. Unpublished report, University of Wisconsin-Madison.
- Harlander, J. & F.L. Roesler. (1990). Spatial heterodyne spectroscopy: a novel interferometric technique for ground based and space astronomy. In D. Crawford (Ed.), *Instrumentation in Astronomy VII, SPIE vol. 1235* (pp. 622-633). Bellingham, Washington: The Society of Photo-Optical Instrumentation Engineers.

- Harlander, J., F.L. Roesler, & S. Chakrabarti (in press). Spatial heterodyne spectroscopy: a novel interferometric technique for the FUV. In O. Siegmund (Ed.), *X-ray/EUV Optics for Astronomy, Microscopy, Polarimetry, and Projection Lithography, SPIE vol. 1343*. Bellingham, Washington: The Society of Photo-Optical Instrumentation Engineers.
- Jakobsen, P., & Kahn, S.M. (1986). On the interpretation of the soft X-ray background: the effects of an embedded cloud geometry. *Astrophysical Journal*, **309**, 682-693.
- Kruger, R.A., L.W. Anderson, & F.L. Roesler (1972). All-reflection interferometer for use as a Fourier transform spectrometer. *Journal of the Optical Society of America*, **62**, 938-945.
- Kruger, R.A., L.W. Anderson, & F.L. Roesler (1973). New Fourier transform all-reflection interferometer. *Applied Optics*, **12**, 533-540.
- Martin, C., and S. Bowyer (1990). Discovery of high-ionization far-ultraviolet line emission from the interstellar medium. *Astrophysical Journal*, **350**, 242-261.
- Mertz, L. (1965). *Transformations in optics*. New York: Wiley.
- Miller, E.E. & F.L. Roesler (in press). *Optical concepts and applications: a textbook for users*. New York: Wiley.

- Reynolds, R.J., F.L. Roesler, F. Scherb, & J. Harlander (1990). Fabry-Perot/CCD multichannel spectrometer for the study of warm, ionized interstellar gas and galactic clouds. In D. Crawford (Ed.), *Instrumentation in Astronomy VII, SPIE vol. 1235* (pp. 610-621). Bellingham, Washington: The Society of Photo-Optical Instrumentation Engineers.
- Ritva, A.M. Keski-Kuuha, R.J. Thomas, J.S. Gum, & C.E. Condor (1990). Performance of multilayer coated diffraction gratings in the EUV. *Applied Optics*, **29**, 4529-4531.
- Roesler, F.L. (1974). Fabry-Perot instruments for astronomy. In *Methods of Experimental Physics, vol. 12, Part A: Optical and Infared*. (pp. 531-567). New York: Academic Press.
- Roesler, F.L. & J. Harlander (in press). Spatial heterodyne spectroscopy: interferometric performance at any wavelength without scanning. In *Optical Instrumentation for the 1990's: Applications in Astronomy, Chemistry, and Physics, SPIE vol. 1318*. Bellingham, Washington: The Society of Photo-Optical Instrumentation Engineers.
- Sakai, H. (1977). High resolution Fourier transform spectroscopy. In G.A. Vanasse (Ed.), *Spectrometric Techniques: Vol. 1* (pp. 1-70). New York: Academic Press.

- Smith, W.J. (1966). *Modern optical engineering: the design of optical systems.* New York: McGraw Hill.
- Thorne, A.P. (1988). *Spectrophysics.* London: Chapman and Hall.
- Vanasse G., & H. Sakai (1966). Fourier Spectroscopy. In E. Wolf (Ed.), *Progress in Optics Vol. 6* (pp. 261-330). Amsterdam: North-Holland.
- Zukic, M., D.G. Torr, J.F. Spann, & M.R. Torr (1990). Vacuum ultraviolet thin films. 2: Vacuum ultraviolet all-dielectric narrowband filters. *Applied Optics, 29*, 4293-4302.

# VITA SHEET

Title of thesis Spatial Heterodyne Spectroscopy: Interferometric Performance at Any Wavelength Without Scanning

Major professor Fred L. Roesler

Major Physics

Minor Distributed

Name John M. Harlander

Place and date  
of birth Frederic, Wisconsin April 20, 1959

Colleges and  
universities:  
years attended  
and degrees

|           |                               |          |
|-----------|-------------------------------|----------|
| 1977-1983 | Univ. of Wisconsin-Eau Claire | BA 1982  |
| 1983-1986 | Univ. of Wisconsin-Madison    | MS 1986  |
| 1986-1991 | Univ. of Wisconsin-Madison    | PhD 1991 |

Memberships in  
learned or  
honorary  
societies Optical Society of America, American Geophysical  
Union, American Association of Physics Teachers, Sigma Pi Sigma

Publications Harlander, J., Roesler, F. L., & Chakrabarti, S.  
(1990) Spatial heterodyne spectroscopy: A novel interferometric  
technique for the FUV. SPIE Symposium Proceedings, No. 1343:  
"X-Ray/EUV Optics for Astronomy, Microscopy, Polarimetry, and  
Projection Lithography", San Diego, California.

continued on next page

Current date Jan. 16, 1991

- Roesler, F.L., & Harlander, J. (1990) Spatial heterodyne spectroscopy: Interferometric performance at any wavelength without scanning. *SPIE Symposium Proceedings*, No. 1318: "Optical Instrumentation for the 1990's: Applications in Astronomy, Chemistry, and Physics", Las Cruces, New Mexico.
- Roesler, F.L., Harlander, J., & Reynolds, R.J. (in press) An observatory for mapping the far UV diffuse galactic emission line background. *IAU Colloquium Proceedings*, No. 123: "Observatories in Earth Orbit and Beyond", Annapolis, Maryland.
- Harlander, J., & Roesler, F.L. (1990) Spatial heterodyne spectroscopy: A novel interferometric technique for ground-based and space astronomy. *SPIE Symposium Proceedings*, No. 1235: "Astronomical Telescopes and Instrumentation for the 21st Century", Tucson, Arizona.
- Reynolds, R.J., Roesler, F.L., Scherb, F., & Harlander, J. (1990) A Fabry-Perot/CCD Multichannel Spectrometer for study of the warm, ionized interstellar gas and extragalactic clouds. *SPIE Symposium Proceedings*, No. 1235: "Astronomical Telescopes and Instrumentation for the 21st Century", Tucson, Arizona.
- Scherb, F., Magee-Sauer, K., Roesler, F.L., & Harlander, J. (1990) Fabry-Perot observations of Comet Halley H<sub>2</sub>O<sup>+</sup>. *Icarus*, 86, 172.
- Magee-Sauer, K., Scherb, F., Roesler, F.L., & Harlander, J. (1990) Comet Halley O(<sup>1</sup>D) and H<sub>2</sub>O production rates. *Icarus*, 84, 154.
- Franke, S.J., Beatty, T., Thorsen, D., Liu, C.H., Gardener, C.S., Roesler, F.L., & Harlander, J. (1990) Simultaneous Na lidar and HF radar observations of vertical velocities in the mesosphere above Urbana, Illinois. *Geophysical Research Letters*, 17, 69.
- Magee-Sauer, K., Scherb, F., Roesler, F.L., Harlander, J., & Lutz, B. (1989) Fabry-Perot observations of NH<sub>2</sub> emission from Comet Halley. *Icarus*, 82, 50.
- Magee-Sauer, K., Roesler, F.L., Scherb, F., Harlander, J., & Oliverson, R.J. (1988) Spatial distribution of O(<sup>1</sup>D) from Comet Halley. *Icarus*, 76, 89.
- Kwon, K.H., Gardner, C.S., Senft, D.C., Roesler, F.L., & Harlander, J. (1987) Daytime lidar measurements of tidal winds in the mesospheric sodium layer at Urbana, Illinois. *Journal of Geophysical Research*, 92, 8781.
- Roesler, F.L., Scherb, F., Magee-Sauer, K., Harlander, J., Reynolds, R.J., & Oliverson, R.J. (1987) Spatial distribution of O(<sup>1</sup>D) from Comet Halley. *Proceedings of the Symposium on the Diversity and Similarity of Comets, Brussels, European Space Agency SP-278*, 217.
- Roesler, F.L., Magee-Sauer, K., Harlander, J., Reynolds, R.J., Oliverson, R.J., Yelle, R.V., & Broadfoot, A.L. (1986) Spatial distribution of [OI] 6300Å emission determined from narrow-band images of Halley's Comet. *Proceedings of the 20th ESLAB Symposium on the Exploration of Halley's Comet, Heidelberg, European Space Agency SP-250*, 413.
- Scherb, F., Roesler, F.L., Magee, K., Harlander, J., & Reynolds, R.J. (1986) Fabry-Perot ground-based observations of Comet Halley. *Advances in Space Research*, 5, 275.
- Roesler, F.L., Scherb, F., Magee, K., Harlander, J., Reynolds, R.J., Yelle, R.V., Broadfoot, A.L., & Oliverson, R.J. (1986) High spectral resolution line profiles and images of Comet Halley. *Advances in Space Research*, 5, 279.
- Reynolds, R.J., Magee, K., Roesler, F.L., Scherb, F., & Harlander J. (1986) H $\alpha$  scans of the intergalactic HI cloud in Leo. *Astrophysical Journal*, 309, L9.